Investigation of Molecular and Electronic Structures to Understand the Expression of TADF Properties in Multiple Resonance Organic Molecules

裵, 宰玄

2024

Doctoral Dissertation

Investigation of Molecular and Electronic Structures to Understand the Expression of TADF Properties in Multiple Resonance Organic Molecules

Jaehyun Bae

Department of Chemistry and Biochemistry

Graduate School of Engineering

Kyushu University

Table of Contents

Chapter III. Experimental Investigation and Visualization of the Electronic Structure of a Single MR-TADF Molecule Using Scanning Tunneling Microscopy

Chapter IV. Summary and Perspective

Chapter I

General Introduction

1. 1. Introduction

Electronics is a scientific discipline that entails the interdisciplinary research of the physical and chemical properties of diverse types of materials. Utilizing electrons or electrically charged particles, it can operate various devices and systems by controlling their flow or interaction with light.[1-3] These devices and systems are the foundation for the vast array of technologies that fuel modern society. Conventional electronics have relied primarily on inorganic materials such as silicon, which has a mature technology ecosystem that includes excellent semiconductor properties, durability, processing, and manufacturing.[4,5]

With the rapid growth of the electronics industry, dependence on electronic devices in our lives is dramatically increasing and the demands on them are expanding beyond their functional benefits. The advent of organic electronics was motivated by the fulfillment of this desire. Organic electronics research has been garnering significant attention due to the advanced properties of organic materials based on carbon-based molecules: mechanical flexibility, the ability to fabricate transparent circuits and displays, low-cost mass production, and the potential for large-area device applications.[6-10] Moreover, the versatility of organic chemistry allows for the molecular engineering of organic semiconductors to tailor their electronic, optical, and mechanical properties, enabling optimization for specific applications.[10] Due to these promising characteristics and potentials, organic electronics is becoming a pivotal technology for future electronic devices and systems.

In particular, the commercial success of organic light-emitting diodes (OLEDs) has triggered a period of rapid development in the field of organic optoelectronic materials and devices.[12-14] The tremendous surge in interest and research efforts has enabled the development of numerous organic materials with enhanced optoelectronic performance, leading to improvements in technology for photon generation. This development of organic electronic devices has been based on studying the electronic structure of organic semiconductors as their materials.[15] In this dissertation, I focus on an analysis of the electronic structure for the optimization of thermally activated delayed fluorescence (TADF) molecules, the state-of-the-art organic semiconductor material for organic optoelectronic devices.

1. 2. Organic light-emitting diodes (OLEDs)

OLEDs have solidified their status as the predominant display technology within our modern living environments, marking a milestone in visual display development.[16,17] OLED displays eliminate the need for backlighting due to their self-luminous nature, providing excellent contrast ratio, fast response time, and vivid color expression. This technology enables organic luminescent materials to emit light

by using organic thin-film layers composed of organic semiconductor materials designed to transfer carriers through hopping when current or electric fields are applied. These features enable OLEDs to realize thinner, lighter, more efficient, and flexible displays.

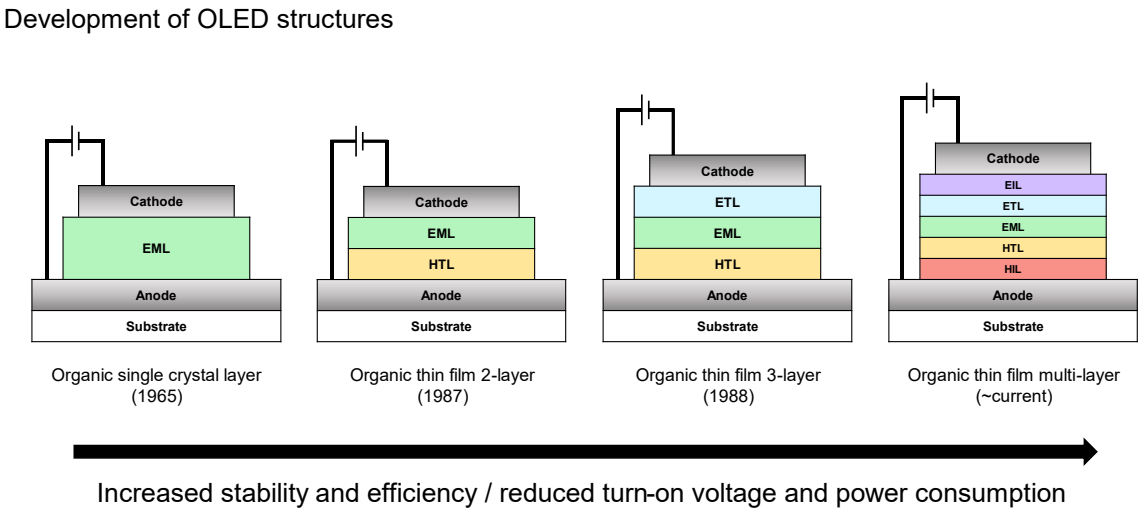

Figure 1-1. Development of OLED structures from single-organic thick crystal layer to multi-organic thin film layers.

The developments in such OLED structures are introduced in **Figure 1-1**. Initial studies on the development of OLEDs were reported by W. Helfrich and W. G. Schneider in 1965.[18] They connected an anthracene single-crystal layer to an electrode with suitable materials for carrier injection and successfully observed blue light emission by applying a high voltage. This basic configuration allowed for the generation of light through the recombination of electrons and holes within the organic material. However, the structure employed in the initial design was similar to that of modern OLEDs, but the organic layer, which is inherently insulating, was 1~5 mm thick and presented a significant barrier to efficient carrier injection and transport. This structural limitation required hundreds of volts of electric voltage to initiate light emission, in marked contrast to the lower voltages required by today's efficient OLED structures. The research fundamental to the OLED structure used today was reported in 1987 by C. W. Tang and S. A. VanSlyke.[19] In their research, OLEDs were fabricated using a bilayer structure, incorporating an emissive layer and a conductive layer sandwiched between two electrodes. The structure of OLEDs in this research was composed of tris(8-hydroxyquinoline)aluminum (Alq_3) and 1,1-bis[(di-4-tolylamino)phenyl]cyclohexane (TAPC) as the emissive layer (EML) and hole transport layer (HTL), respectively, with indium tin oxide (ITO) as the anode and Mg:Ag as the cathode. It is noteworthy that the thickness of each organic layer was significantly reduced to about 60-75 nm by vacuum deposition. Due to this thin film structure, this OLED structure showed a luminance of 1000 cd/m² under 10 V and an external quantum efficiency (EQE) of about 1%.

As research and development progressed, more sophisticated try-layer structures were introduced to enhance performance. In 1988, Adachi Chihaya et al. designed an OLED that incorporated an electron transport layer (ETL) to effectively facilitate the transfer of charge carriers to the emissive layer.[20] In this research, the emissive layer is sandwiched between N,N′-bis(3-methylphenyl)-N,N′-diphenylbenzidine (TPD) as the hole transport layer (HTL) and perylene tetracarboxylic derivative (PV) as the electron transport layer (ETL), with each transport layer designed to efficiently inject and transfer carriers from the electrodes. As a result, emission was observed at 420 nm, 500 nm, and 600 nm, corresponding to the materials anthracene, coronene, and perylene used in the emissive layer, respectively. The introduction of these additional transport layers resulted in a threshold voltage of about 4 V, and the device demonstrated high stability at a driving voltage of 60 V. It is remarkable that this research results showed not only improvement of the efficiency through a multilayer structure in OLEDs but also realize multicolor light emission toward full-color displays by altering the emitters. Following these studies, research into multilayered OLED structures has been actively investigated.

The structure of current OLEDs has been refined through the integration of electron injection layers (EILs) and hole injection layers (HILs) directly from the electrodes, facilitating more efficient injection of electrons and holes. In addition, the EML is designed as a host-guest system with doped film, which prevents aggregation quenching of the organic small molecules as emitters and thereby improves the emission efficiency.[21-25] In addition, the introduction of blocking layers allows the injected carriers to be precisely positioned to participate in the emission process. The progressive development of these multi-layer structures has contributed significantly to the enhancement of device performance. Advances in the multilayer structure of OLEDs are designed to optimize the efficient injection of electrons and holes and their subsequent recombination at precise locations. These optimizations were guided by the light-emitting mechanism of OLEDs, which is based on electroluminescence (EL).

1. 2. 1. Electroluminescence

EL is a phenomenon in which a material emits light in response to the application of an electric field, representing a fundamental mechanism in the operation of various optoelectronic devices, including OLEDs.[26] This process is implemented by the recombination of electrons and holes within the material, leading to the release of energy in the form of photons. In the OLEDs, electrons from the cathode and holes from the anode are injected and transferred into the EML layer.[18] When a recombination of these charge carriers occurs, they transition from an excited state to a lower energy level, resulting in the emission of light whose energy is determined by the energy level of the organic material used in the EML layer. This process results in light with an energy corresponding to the energy level of the excited

states of the organic molecules in the EML layer. **Figure 1-2a** shows a schematic illustration of this process within OLEDs.

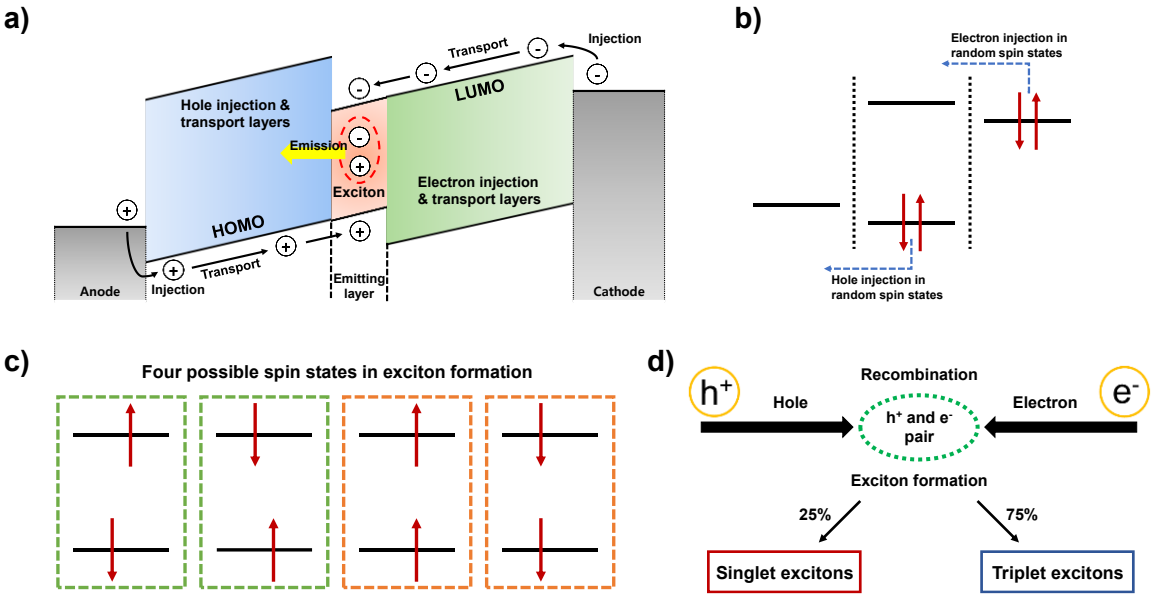

Figure 1-2. a) Schematic illustration of the electron and hole injection process and exciton formation in an OLED. **b)** Spin states of electrons transferred in the process of electron and hole injection. **c)** Possible spin states of excitons formed by the EL process in OLEDs. **d)** Recombination by hole and electron pairs and exciton formation by spin-statistics.

A distinctive characteristic of EL devices that utilize excitons formed by the recombination of injected electrons and holes is that the spin state of the injected electrons in the device is a ransom (**Figure 1-2b**). In the case of electron injection, electrons are transferred from the Fermi energy level of the cathode to the lowest unoccupied molecular orbital (LUMO) energy level of the organic molecules that compose the organic layer of the OLEDs, and likewise, in the case of hole injection, electrons are transferred from the highest occupied molecular orbital (HOMO) of the organic molecules to the anode. The spin state of all electrons migrating in this process is a random orientation.

Figure 1-2c shows the possible combinations of each direction of electron spins. Considering the spin angular momentum of an electron, each spin state can be distinguished by the absolute value of the sum of its spin quantum numbers (s), which can be either 0 or 1. In cases where the sum of the spin quantum numbers is 0, singlet excitons are formed, while in cases where the sum is 1, triplet excitons are formed. For the two quantum states represented by the green dashed lines in **Figure 1-2c**, there are cases where two single excitons or two triplet excitons are formed. In contrast, for the two quantum states shown with dashed orange lines in **Figure 1-2c**, there are only cases where four triplets of excitons are formed. Therefore, the ratio of total cases where the spin quantum number $s = 0$ to cases where the $s = 1$ is 1:3. This indicates that the excitons formed in electroluminescent devices are composed of 25% singlets and

75% triplet by spin statistics (**Figure 1-2d**). Since OLEDs utilize light generated by the energy emitted when an electron transitions from an excited state to a ground state by an exciton formed, the type of exciton formed has a significant impact on device efficiency.

1. 2. 2. Device efficiency

In OLEDs, EL quantum efficiency is a pivotal factor in device evaluation because it directly correlates to device performance and energy efficiency. This efficiency metric is crucial for determining how effectively OLEDs can convert electrical energy into light. Quantum efficiency in the context of OLEDs refers to the ability of the device to convert electrical energy into light. The EQE represents the ratio of emitted photons to the number of charge carriers injected into the OLEDs. The EQE (η_{ext}) is determined by the internal quantum efficiency (η_{int}) and the outcoupling efficiency (η_{out}) as follows.

$$\eta_{ext} = \eta_{int} \cdot \eta_{out} \tag{1.1}$$

In addition, the η_{int} is yielded by the factors of charge carrier balance (γ), radiative exciton fraction (η_r), and effective radiative quantum efficiency (q_{eff}). [29]

$$\eta_{int} = \gamma \cdot \eta_r \cdot q_{eff} \tag{1.2}$$

Figure 1-3 describes the four individual factors of the EQE in relation to the structure of OLEDs. The coefficient γ refers to efficient charge carrier recombination, achieving values close to 1 by precisely adjusting the multi-layered stack structure of the OLEDs and the thickness and charge mobility of each organic layer. The q_{eff} reflects the competition between radiative and non-radiative decay processes. By employing materials with high internal photoluminescence quantum yields (PLQY), values near 100% can be achieved. Furthermore, q_{eff} can be influenced by device elements such as the Purcell effect induced by microcavities and exciton quenching at high current densities. η_{out} typically stands at around 20% for emitters with random orientations and is measured as the proportion of photons that actually leave the OLEDs.

Therefore, as an organic light emitter that follows the EL mechanism, the most significant contribution to the quantum efficiency of OLEDs is to maximize η_r. The η_r is governed by quantum-mechanical selection rules: Only singlet excitons (total spin zero) can decay radiatively, while triplet excitons (total spin one) decay nonradiatively.[27,28] This rule can be bypassed with strong spin-orbit coupling (SOC) between singlet state and triplet state, but for typical fluorescent molecules, the SOC is too weak to deviate from this rule significantly at room temperature. Therefore, for most fluorescent luminescent materials, this value is limited to 25%. To overcome this efficiency limitation, it's essential to enable triplet excitons to undergo radiative decay and participate in the emission process. Numerous

research efforts have been dedicated to establishing various photophysical strategies to harvest triplet excitons in dark exciton states that are annihilated by non-radiative processes.

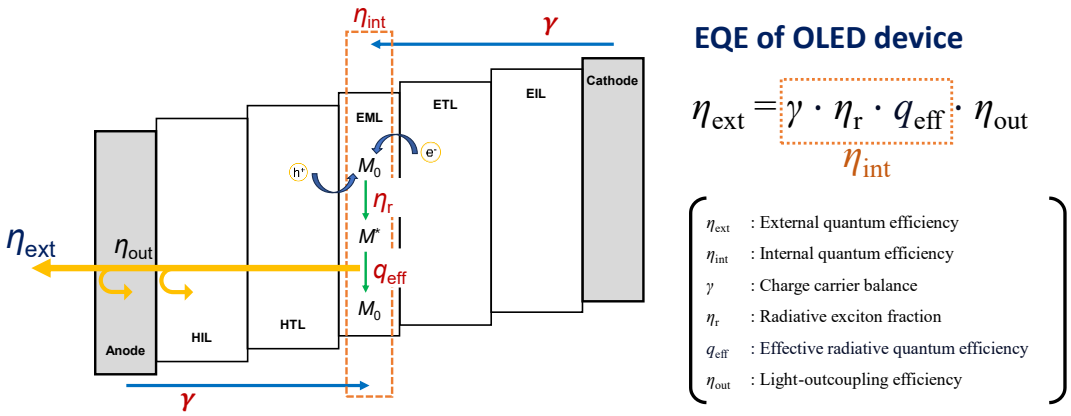

Figure 1-3. Schematic illustration for explanation of quantum efficiency of OLEDs.

1. 3. Thermally activated delayed fluorescence (TADF)

The intense research interest in TADF materials is closely linked to efforts to improve OLED efficiency.[30-33] TADF materials can harness both single and triplet excitons for luminescence by utilizing a reverse intersystem crossing (RISC) process activated by thermal energy. This process efficiently converts non-radiative triplet excitons into radiative single excitons, significantly improving the EQE of OLEDs without relying on heavy metal ions such as phosphorescent materials. The performance of TADF materials, including absorption, emission characteristics, and quantum efficiency, is primarily determined by the electronic structure, which includes the HOMO and the LUMO. Therefore, designing efficient TADF emitters requires a deep understanding of the precise electronic structure and energy levels related to the molecular structure.

1. 3. 1. Light emission from organic material

Organic materials based on carbon are generally known as insulators, but some organic compounds with a π-conjugation structure can exhibit properties of semiconductors or conductors. These organic semiconductor materials can transport electrons via specific energy levels under external electric fields in organic thin film, making them primary materials for OLEDs. The π-conjugation structure is not only utilized for electron transport but also causes primary absorption through π bonds. The electron

transition, in this case, occurs from the π orbital to the π* orbital, hence it is called a π-π* transition. The unit that shows primary absorption transition through π bonds is referred to as a chromophore. In organic compounds, the presence of lone pairs of electrons can lead to additional absorption, and the unit that supports the chromophore's absorption by lone pairs of electrons is called an auxochrome. Nitrogen and oxygen are representative elements that have lone pairs of electrons, and when an organic molecule includes a functional group of these atoms, it possesses an n orbital. Since this n orbital does not form a bond, it is not stabilized. Thus, the position of its energy exists between the HOMO and LUMO, allowing for a transition to the π* orbital (n-π* transition). Fundamentally, the luminescence of organic compounds is primarily the result of electron transitions between molecular orbitals (MOs), specifically between occupied and unoccupied orbitals. Therefore, by controlling the appropriate energy difference between the HOMO and the LUMO, it is possible to control the luminescence process of organic molecules to absorb specific energies. This energy difference between HOMO and LUMO is called the bandgap.

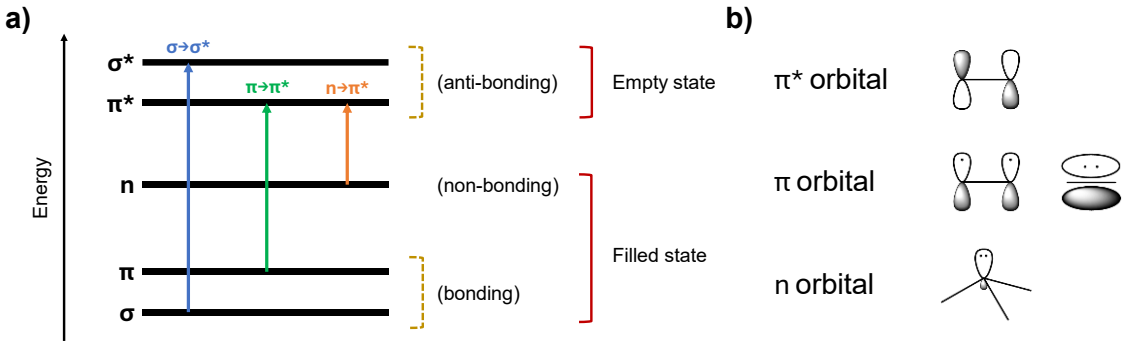

Figure 1-4. A schematic illustration of **a)** the possible electronic transitions in the energy absorption and **b)** orbitals that mainly participate in energy absorption.

In OLEDs, this absorption process occurs as the injected carriers, i.e., electrons and holes, move to the EML and are attracted by the Coulomb force to form electron-hole pairs known as excitons. The excitons formed by the holes and electron recombination electrically excite organic molecules, and this exciton then decays to generate a photon, which produces light. By adjusting the bandgap, the energy of the emitted light can be controlled, which in turn determines the frequency of the light, thus allowing for the realization of light in various colors.[34] Therefore, organic compounds are indispensable to OLED technology due to their adaptability, which allows for the emission of a wide range of colors through chemical synthesis, and their ability to easily form thin films through vacuum thermal deposition. Based on the fundamental luminescence principles of organic compounds in OLED technology, efforts to improve the performance and efficiency of fluorescence have led to the exploration of phosphorescence and TADF mechanisms.

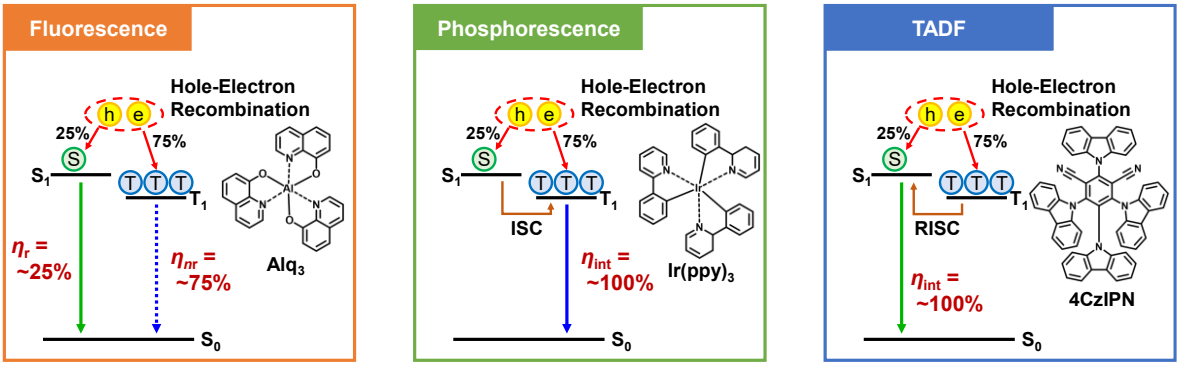

Figure 1-5. EL mechanisms and representative materials of fluorescence, phosphorescence, and TADF. The materials are Alq_3 for fluorescence, $Ir(ppy)_3$ for phosphorescence, and 4CzIPN for TADF, respectively.

Figure 1-5 illustrates the EL mechanisms of fluorescence, phosphorescence, and TADF and their representative molecules used as organic luminescent materials for OLEDs. First, Fluorescence in OLEDs is a process where an organic molecule is electronically excited by exciton and emits light. Excitons in singlet states have a relatively short emission lifetime, and when the electron returns to its ground state, it emits a photon. The efficiency of fluorescent materials is inherently limited by spin statistics to approximately 25%. This limitation arises because only singlet excitons can undergo fluorescence, and according to spin statistics, singlet excitons are formed only 25% of the time during electron-hole recombination. An example of a fluorescent material used in early OLEDs is Alq_3.[19] Despite its importance in demonstrating the potential of OLED technology, the quantum efficiency limitation of fluorescent materials prompted the search for more efficient light-emitting mechanisms.

Phosphorescence, unlike fluorescence, involves the emission of light from a triplet excited state. These excitons in the triplet excited state have longer emission lifetime than the singlet state due to the "forbidden" transition by spin selection rules, resulting in emission lifetimes of microseconds to milliseconds.[35,36] The incorporation of heavy metal atoms into the organic compound, such as iridium (Ir) or platinum (Pt), facilitates intersystem crossing from the singlet to the triplet state, thereby overcoming the spin-statistics limitation and enabling nearly 100% internal quantum efficiency (IQE).[37] An example of a phosphorescent material is $Ir(ppy)_3$, tris(2-phenylpyridinato)iridium(III).[38] The use of such phosphorescent emitters marked a significant advancement in OLED technology, allowing for the development of highly efficient displays and lighting systems. However, the reliance on heavy metals raised concerns about cost, environmental impact, and the broader emission spectra that could affect color purity. In addition, using triplet state energy for blue color luminescent materials requires high energy, leading to rapid molecular degradation and making the development of stable blue light sources challenging.

In 2012, the remarkable potential of TADF emitters as the next-generation luminescent materials was reported.[39] These TADF emitters are composed entirely of pure organic compounds and can achieve 100% internal quantum efficiency (IQE) by utilizing the triplet excitons at room temperature.[40,41] This high efficiency is achieved through a RISC process, which allows for the conversion of excitons from the lowest excited triplet state back to the lowest excited singlet state. This conversion enables the harnessing of both prompt and delayed fluorescence, significantly improving the IQE and, consequently, the EQE of OLEDs.

One of the most prominent examples of a TADF molecule is 4CzIPN (1,2,3,5-tetrakis(carbazol-9-yl)-4,6-dicyanobenzene).[39] Its organic molecular structure facilitates efficient RISC, leading to the effective utilization of both singlet and triplet excitons for light emission. In particular, TADF emitters do not require heavy metal complexes, thereby addressing the cost and environmental concerns associated with phosphorescent materials. Additionally, TADF emitters have attracted significant interest due to their high potential for the development of highly efficient blue luminescent materials, as they utilize the energy of a single state for emission.[42]

In a paper reporting on 4CzIPN, Prof. Adachi's group also reported TADF materials with a wide range of emission wavelengths from 473 nm to 577 nm using similar carbazole and dicyanobenzene-based compounds. This indicates that the bandgap of organic TADF materials can be easily adjusted through modification of the molecular structure and shows promise for the development of full-color OLEDs (**Figure 1-6**). The report of successful high-performance device fabrication utilizing this series of TADF materials marks a new milestone for OLED technology as the next generation of organic light-emitting materials.[43]

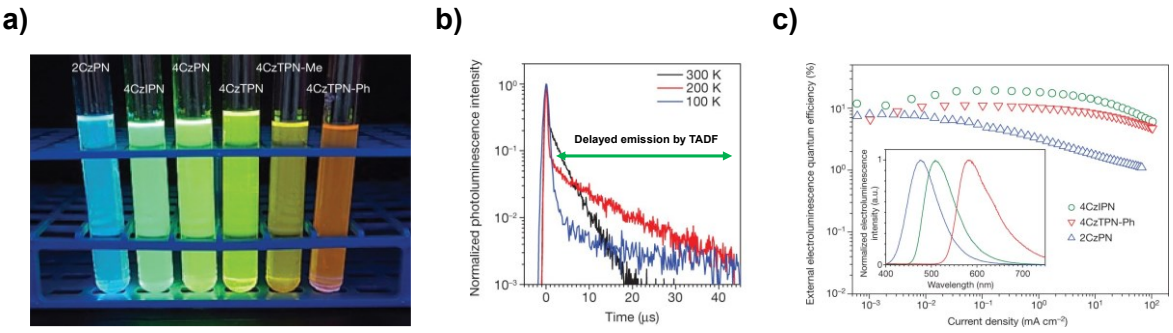

Figure 1-6. a) Photograph of carbazoles and dicyanobenzene-based TADF materials under irradiation at 365 nm. **b)** Temperature dependence of the photoluminescence decay curve of 6wt% 4CzIPN: CBP film. Since TADF activity is thermally active, its delayed fluorescence has a temperature dependency. **c)** Measured device performance using TADF materials. It demonstrates that the TADF emitter can overcome the limitations of fluorescence efficiency, showing a maximum EQE of up to 19.3%. **All figures** edited with permission from Uoyama et al., *Nature* **492**, 234-238 (2012), *Copyright © 2012 Springer Nature*.[39]

1. 3. 2. Mechanism of organic TADF molecules

The main design strategy of the TADF molecule still follows the design of the 4CzIPN molecule. A notable design strategy was to link the carbazole unit, which acts as an electron donor, and the dicyanobenzene unit, which acts as an electron acceptor, in a single bond, effectively separating the HOMO and LUMO. The spatial separation of HOMO-LUMO is correlated with the energy difference between singlet and triplet state (ΔE_{ST}) to activate RISC by the following equation,[44-46]

$$\Delta E_{ST} = \Delta E_S - \Delta E_T = 2J \tag{1.3}$$

$$J = \iint \Phi_H(r_1)\Phi_L(r_2)\frac{e^2}{|r_2 - r_1|}\Phi_H(r_2)\Phi_L(r_1)dr_1dr_2 \tag{1.4}$$

wherein J is exchange energy, Φ_H and Φ_L are HOMO and LUMO wave-function, e is the electron charge. r_1 and r_2 are the electron coordinates. Increasing the spatial separation of HOMO and LUMO generally minimizes the quantum effects of exchange correlations, reducing the ΔE_{ST}. In particular, for the 4CzIPN molecule, the carbazole and dicyanobenzene units are twisted to each other, further reducing orbital overlap, which resulted in a significantly low ΔE_{ST} value. This strategic design is crucial to facilitate effective RISC processes in the TADF molecules. Therefore, the TADF molecule is designed as a D-A type organic molecular structure with a donor (D) unit as HOMO and an acceptor (A) unit as LUMO. This structural configuration results in the TADF molecule exhibiting intramolecular charge transfer (ICT) characteristics. However, this HOMO-LUMO separation also caused the transition dipole moment to decrease. The transition dipole moment (μ) is related to the oscillator strength (f), which represents the transition probability, through the following simple relationship.

$$f \propto \mu^2 \tag{1.5}$$

As a result, the separation of HOMO and LUMO dramatically increases the η_r in device efficiency but also reduces q_{eff}. To mitigate this conflict, it is notable that dicyanobenzene is used as the electron acceptor. The cyano groups in the dicyanobenzene unit suppress non-radiative deactivation by minimizing geometric changes in the excited state. Thus, 4CzIPN exhibited excellent TADF performance and high PLQY ($\Phi \approx 0.94$).

After a design strategy was presented for synthesizing highly efficient TADF molecules, a lot of research has been conducted to improve the RISC ratio through more accurate numerical analysis and predictions. In the context of theoretical calculations for designing TADF molecules, Fermi's golden rule, which assumes that the transition rate is determined by the interaction of electrons between the initial and final states of the system, has been applied. In 2017, Pralok K. Samanta et al. applied the Marcus−Levich−Jortner theory to Fermi's golden rule to compute the rate constant for RISC,

numerically analyzing the correlation between k_{RISC}, ΔE_{ST}, and the SOC matrix element (SOCME).[47] Based on Marcus−Levich−Jortner theory, the rate constant for RISC, associated with spin upconversion between the singlet and triplet states, can be described as follows,

$$k_{\mathrm{RISC}} = \frac{2\pi}{\hbar}\left|\langle\psi_{\mathrm{S}}|\hat{H}_{\mathrm{SOC}}|\psi_{\mathrm{T}}\rangle\right|^2 \frac{1}{\sqrt{4\pi\lambda k_B T}} \exp\left[-\frac{(\Delta E_{ST}+\lambda)^2}{4\lambda k_B T}\right] \quad (1.6)$$

where k_{RISC} is the rate constant of RISC, $\langle\psi_{\mathrm{S}}|\hat{H}_{\mathrm{SOC}}|\psi_{\mathrm{T}}\rangle$ is SOCME between triplet and singlet states, and ΔE_{ST} is the energy splitting between singlet and triplet states. The other variables and constants are as follows; $\hbar$ is Dirac's constant, λ is the reorganization energy, k_B is the Boltzmann constant, T is the temperature. Therefore, in order to design an optimized TADF molecule with a high RISC ratio, the molecular structure must be delicately designed using two strategies (**Figure 1-7**): i) To minimize ΔE_{ST}, the two frontier molecular orbitals (FMOs), HOMO and LUMO, of the organic molecule should be spatially well-separated with minimal overlap. ii) To maximize SOCME, heavy atoms can be inserted into the molecule, or the transition nature between the singlet and triplet excitonic states should involve a radiationless transition that changes the MO type (El-Sayed rule).[48,49]

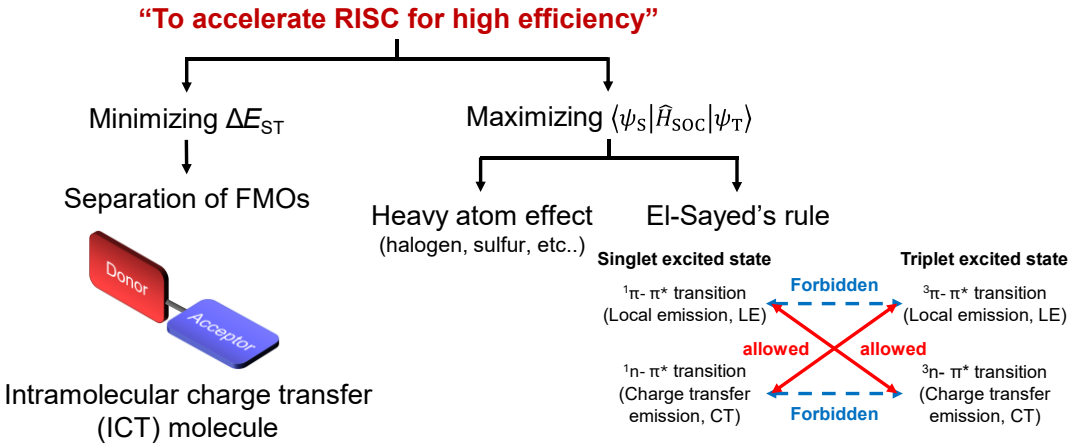

Figure 1-7. Strategies for TADF molecular design to accelerate RISC.

In particular, this analysis emphasizes that high RISC is not achieved solely by the separation of the HOMO and LUMO wavefunctions of D-A type TADF molecules, but also requires differences in the transition characteristics of the S_1 excited state and triplet state to achieve strong SOC. The establishment of the TADF design strategies has provided the foundation for the development of various TADF materials that exhibit enhanced efficiency by accelerating the RISC rate. Despite these advancements, the ICT characteristics originating from the D-A configuration have posed challenges for the development of high-performance OLEDs, imposing broad emission spectra and low *f* values on TADF

emitters. To overcome these issues, additional strategies are needed to achieve the narrowband emission and high *f* values required for display applications with high performance and wide color gamut.

1. 3. 3. Multiple-resonance (MR-) TADF molecules

Although there have been many efforts to improve the color purity of TADF emitters, reconciling the low full width at half maximum (FWHM) characteristics of the emission spectrum with high RISC rates has proven challenging. To address these issues, Hatakeyama et al. introduced a new type of TADF emitter in 2016 that can achieve narrowband emission and high *f* with multiple resonance (MR) effects.[50] The strategic embedding of electron-rich and electron-deficient atoms within the polycyclic aromatic hydrocarbon (PAH) core facilitated resonance effects to separate FMOs with structural rigidity, resulting in sharper emission spectra that enable the expression of high color purity. The resonance effect induced by heteroatoms, composed of pairs of electron-rich and electron-deficient atoms embedded adjacent to the aromatic rings within the PAH core, creates the HOMO and LUMO on carbon atoms at the *ortho* and *para* positions of the heteroatoms (**Figure 1-8a**).[51,52]

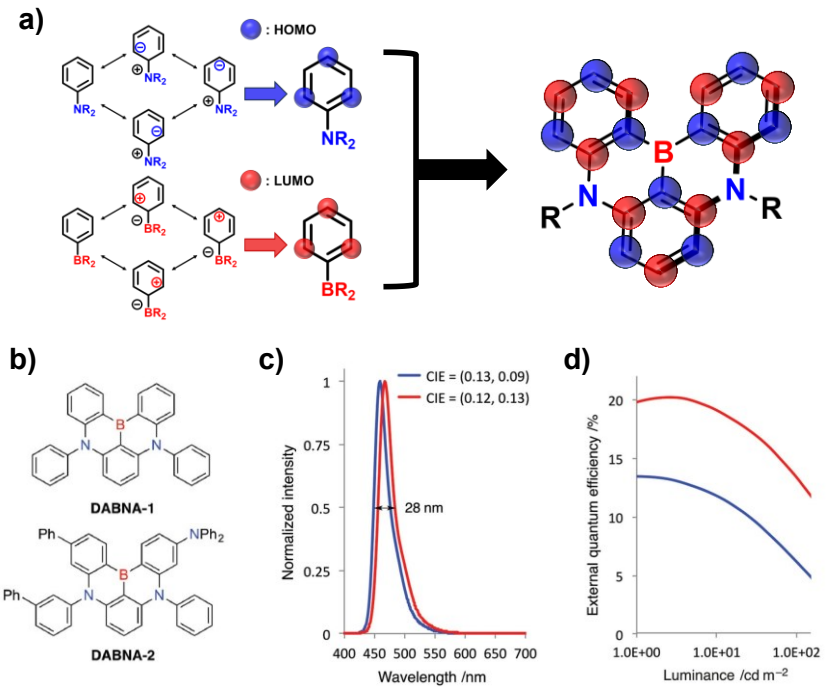

Figure 1-8. a) A schematic illustration of the resonance effect caused by electron-rich nitrogen atoms and electron-deficient boron atoms and HOMO-LUMO separation in MR-TADF molecules induced by resonance effect. **b)** Molecular structure of DABNA-1 and DABNA-2. **c)** EL spectra with CIE coordinates and **d)** EQE-luminescence characteristics of DABNA-1 and DABNA-2. The blue line is DABNA-1, and the red line is DABNA-2, respectively. **Figures 1-8b**, **1-8c**, and **1-8d** are adapted with permission from Takuji Hatakeyama et al., *Adv.Mater.* **28**, 2777 (2016), Weinheim, © 2016 WILEY-VCH Verlag GmbH & Co. KGaA.[50]

These donor and acceptor regions formed inside the PAH core generate multiple sites of short-range charge transfer (CT) within the molecule. Consequently, this delocalized short-range CT allows MR-TADF molecules to achieve high *f* and narrowband emission. Therefore, the MR-TADF emitter maintains TADF performance while simultaneously achieving high *f* and narrowband emission, significantly enhancing the commercial viability of organic EL devices using TADF emitters. **Figure 1-8b** shows the molecular structure of DABNA-1 and DABNA-2, representative MR-TADF molecules. DABNA-1 exhibits an emission at 459 nm with an FWHM of 28 nm, achieving CIE coordinates of (0.13, 0.09) and an EQE of 13.5%. This indicates a very narrow and pure blue emission, which is desirable for high-quality OLEDs. DABNA-2, on the other hand, is a derivative of DABNA-1 with improved *f*, emitting at 467 nm with an identical FWHM of 28 nm, CIE coordinates of (0.12, 0.13), and a notably higher EQE of 20.2%. The enhancements in DABNA-2 are attributed to the introduction of substituents that improve *f* without affecting the localization of MOs, leading to better device performance (**Figures 1-8c** and **1-8d**).

However, MR-TADF materials pose challenges to analysis using computational chemistry, especially when predicting the properties of excited states accurately. This challenge is based on the intricate distribution of MOs within a molecule, featuring the presence of MR structures within the molecule that contribute to the TADF behavior.[53,54] While density functional theory (DFT) and time-dependent (TD)-DFT approaches have been the foundation of TADF materials research, their limitations in accurately estimating ΔE_{ST} and other excited-state properties of MR-TADF materials have led researchers to explore more advanced methods. The SCS-CC2 (Spin-Component Scaling Second-order approximate Coupled Cluster) method which is based on the post-Hartree-Fock (post-HF) method represents a significant advancement over DFT and TD-DFT for MR-TADF materials, offering more accurate predictions for ΔE_{ST} values and *f*.[55] This accuracy is crucial for designing efficient MR-TADF molecules, as it allows for a more precise understanding of how molecular design influences TADF performance. The SCS-CC2 method provides better agreement with experimental results by incorporating electron correlation effects effectively, resulting in more accurate predictions than simple DFT and TD-DFT approaches for MR-TADF materials. However, despite the success of SCS-CC2 in predicting ΔE_{ST} and *f* values for MR-TADF materials, challenges remain. In particular, the discrepancies between predicted and experimental values for individual S_1 and T_1 states are still large, indicating that this method still has limitations for precise analysis of single and triple states.

Given the complexities of the electronic structure of MR-TADF materials, originating from their MR effects, there is a clear need for the development of new computational strategies or the enhancement of existing ones. Such Advances in these new analytical methods would enable a deeper understanding of the electronic structures of MR-TADF molecules, facilitating the design of more effective TADF

emitters and contributing to the development of OLEDs with improved color purity and quantum efficiencies.

1. 4. Methodology for analyzing electronic structures

While MR-TADF molecules have exhibited significant advancements as previously mentioned, the analysis of their electronic properties has significantly depended on computational approaches like DFT and post-HF methods.[53-55] Experimental approaches, including electrochemical techniques such as cyclic voltammetry (CV) and spectroscopic methods like photoelectron and UV-Vis spectroscopy, have also been employed to explore their electronic characteristics, particularly in the condensed solid-state phase (or bulk state).[56-58] However, these systems have presented challenges in experimentally analyzing the electronic structure at the single-molecule level, which plays a crucial role in the luminescence mechanism of MR-TADF molecules. While device fabrication leverages the solid-state properties of TADF molecules, the design process often starts with an understanding of individual molecule properties. Thus, a precise experimental analysis of a single TADF molecule could serve as a crucial benchmark for its design and further development. The experimental investigation of the electronic structure at the atomic level is expected to significantly advance our comprehension of the distinctive electronic properties inherent to MR-TADF molecules.

In this context, I have introduced the scanning tunneling microscopy (STM) technique for the precise experimental analysis of single MR-TADF molecules, alongside the advanced computational chemistry methods, including the similarity transformed equation-of-motion domain-based local pair natural orbital coupled-cluster singles and doubles (STEOM-DLNPO-CCSD) method.[59-63] The atomic-level experiment using STM will enable a comprehensive understanding of the intricate electronic structure and CT behavior of individual MR-TADF molecules, paving the way for the optimized design of next-generation OLED materials.

1. 4. 1. Scanning tunneling microscopy (STM)

STM is a powerful and versatile technique that allows for the imaging and probing of surfaces or target molecules on the surface at the atomic level. STM operates by scanning a sharp tip close to the surface of a conductive or semiconductive sample. An applied bias voltage between the STM tip and the sample allows electrons to tunnel through the vacuum gap, with the tunneling current being highly sensitive to the tip-to-sample distance. This sensitivity enables the STM to achieve atomic-scale

resolution, making it a powerful tool for observing the topography of surfaces. These topographical scans cross a two-dimensional plane utilizing quantum tunneling effects to detect the tunneling current attributed to the spatial distribution of the local density of states (LDOS) of the sample when a bias voltage is applied. This can be expressed by the following equation,[59,61]

$$I_{t\to s} \approx -\frac{4\pi e}{\hbar} e^{-d\sqrt{\frac{8m\varphi}{\hbar^2}}} \rho_t(0) \int_0^{eV} \rho_s(\varepsilon) d\varepsilon \tag{1.6}$$

where $I_{t\to s}$ is tunneling current between tip to sample and d is the width of the barrier corresponding to tip-sample separation, $\rho_s(\varepsilon)$ is DOS for the sample at energy ε, with respect to the Fermi level of the sample. For the STM tip material, it is assumed that DOS is constant within the energy range of the Fermi surface. Therefore, $\rho_t(0)$, DOS for the tip, can be treated as a constant. For the other constants, e is the electron charge and φ is the height of the barrier. It is noteworthy that the value of the tunneling current is proportional to the integral of the DOS up to the bias voltage of the sample and exponential to the distance between the tip and the samples. These differences provide high sensitivity to the distance between the STM tip and the sample due to changes in the DOS affecting the tunneling current. **Figure 1-9** presents a schematic illustration that depicts the basic operating principle and measurement system of STM.

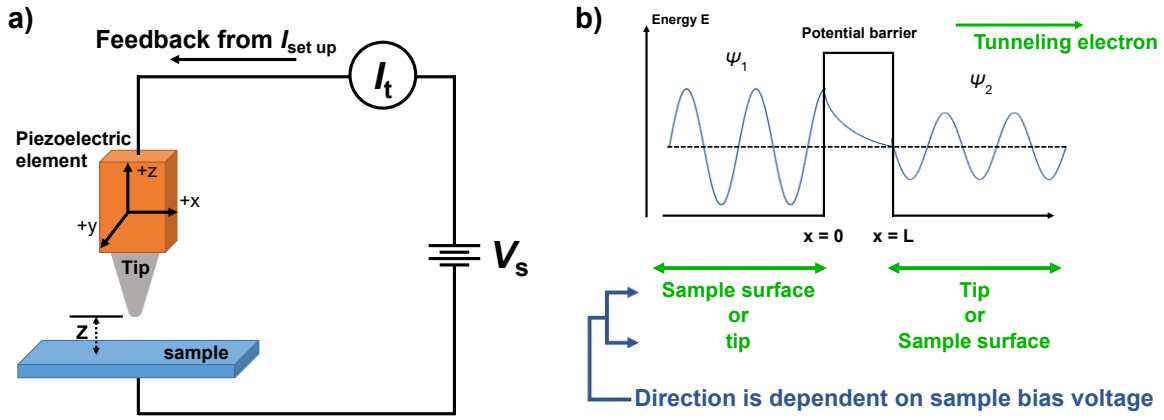

Figure 1-9. Schematic illustration of **a)** STM operations with STM tip and feedback loop and **b)** tunneling effect for tunneling current detection.

The feedback loop is an important part of STM operation. The main role of the feedback loop is to maintain a constant tunneling current between the tip and the sample as the tip scans the surface. This is crucial because the tunneling current is exponentially dependent on the distance between the tip and the sample surface, so even a small change in distance can result in a large change in current. A feedback loop adjusts the height of the tip to keep the tunneling current constant, allowing the topography of the sample to be accurately mapped with atomic resolution. By monitoring the current, which is adjusted to

maintain this constant current by a feedback loop, the STM can generate detailed images of the surface structure.

The movement of the STM tip is precisely controlled by a connected part consisting of the piezoelectric element. Piezoelectric materials change shape when an electric voltage is applied to them, a property that STM leverages to achieve fine movement. By applying a voltage to the piezoelectric actuator, the STM can move the tip in three dimensions: laterally across the sample surface (x and y axis) and vertically approach or retract from the surface (z axis). This precise control allows the STM tip to scan the sample surface with atomic-scale resolution.

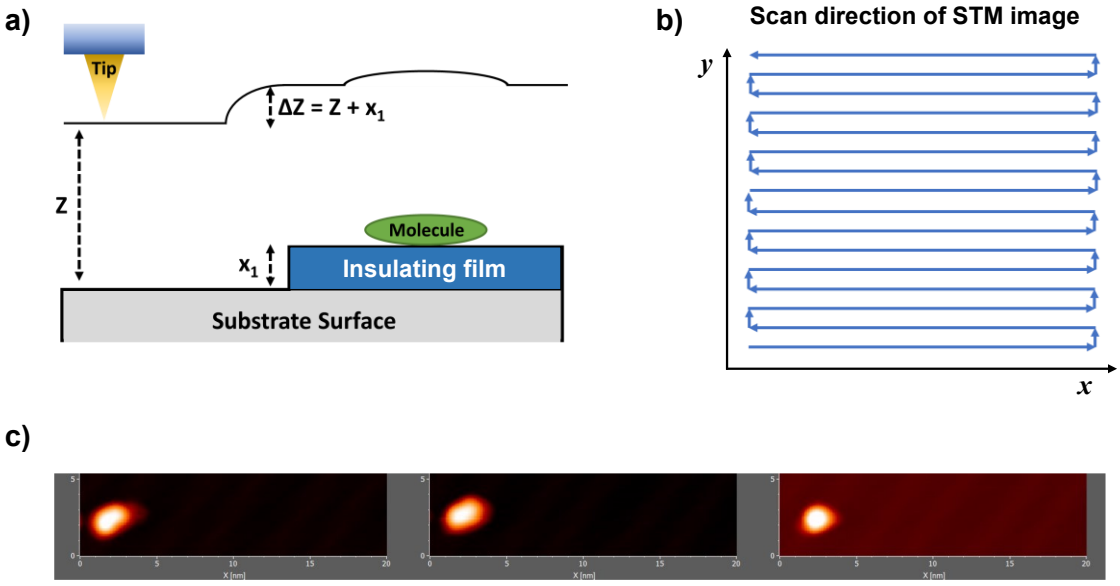

Figure 1-10. Schematic illustration of **a)** STM operations with STM tip and feedback loop and **b)** tunneling effect for tunneling current detection. **c)** Apex of tip cleaning using z-ramp function. By crashing the tip into the surface of the metal sample, the apex is sharpened into a single, symmetrical shape.

First, in STM measurements, the STM tip is positioned at a tip-to-sample distance (Z) corresponding to the initial setup of tunneling current (I_t) and sample bias voltage (V_s) using a feedback loop (in **Figure 1-10a**). The z-distance is typically around 1 nm or less. The sample is then scanned based on the geometric information of the surface as compensated by the feedback loop. The scan direction is shown in **Figure 1-10b**. During a single scan procedure, the STM tip moves alternately along the +x and -x axes. This approach allows to acquisition of two separate scan images, a forward image and a backward image, depending on the scanning direction. Each of these images represents the topography and electronic properties of the surface captured while traveling in one direction. By comparing the forward and backward images, researchers can identify inconsistencies in the data, leading to a more accurate and reliable interpretation of the surface's properties. High-resolution imaging requires a sharp tip, and the shape or apex of the STM tip has a significant impact on the scanned image produced. However,

contamination of the tip during scanning can cause blurred or double images. Therefore, it is important to clean the tip consistently throughout the experiment to maintain image quality and accuracy to gain reliable insight into the material surface at the atomic level (**Figure 1-10c**).

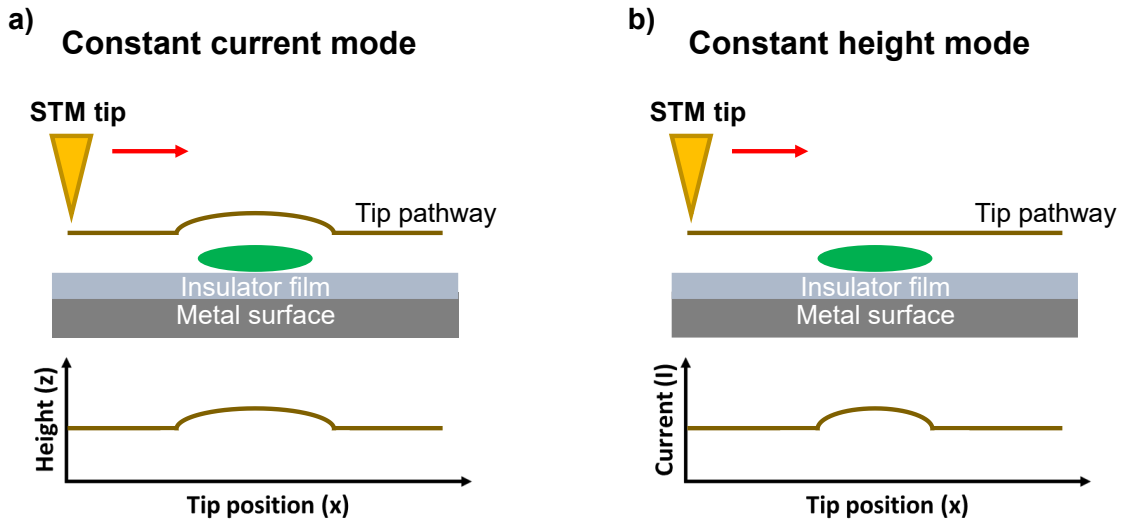

Figure 1-11. Schematic illustration of two different STM scan modes: **a)** Constant current (C.C.) mode and **b)** constant height (C.H.) mode.

Two basic STM modes are used for sample scanning: Constant current (C.C.) mode and constant height (C.H.) mode. In C.C. mode, the scanning using the STM tip operates by maintaining a constant tunneling current between the tip and the sample surface (**Figure 1-11a**). This is achieved through a feedback loop that detects fluctuations in the tunneling current and compensates for them by adjusting the vertical position of the tip. This adjustment ensures that the tip remains in the exact spatial position where the preset tunneling current is consistently detected, allowing the topography of the sample surface to be effectively mapped with high accuracy. In particular, this C.C. mode can prevent the STM tip from being damaged by geometric protrusions on the surface of the sample.

Alternatively, in C.H. mode, the STM maintains the tip at a predetermined height above the sample surface and detects changes in the tunneling current at this fixed height (**Figure 1-11b**). C.H. mode is particularly suited for scanning surfaces that are relatively flat, as significant variations in surface height can lead to a loss of tunneling current and, consequently, a loss of image resolution. However, C.H. mode offers several advantages, including producing STM images that better represent the actual size of the molecules on the surface. In addition, because the tip's height does not need to be continuously adjusted, C.H. mode enables faster scanning speeds compared to C.C. mode.

Each mode has its specific applications and limitations. C.C. mode is widely used for its ability to accurately follow the surface contours, making it ideal for samples with varied topography. It is

particularly utilized to scan large areas safely. In contrast, the C.H. mode is efficient for scanning flat surfaces at a higher scan rate, and for single molecules, it can offer STM images that are in better agreement with the actual molecule size to the distribution of electronic states.

1. 4. 2. Scanning tunneling spectroscopy (STS)

Scanning Tunneling Spectroscopy (STS) is an advanced technique that employs the foundational principles of STM to not just visualize, but also analyze the electronic structure of materials with remarkable precision. STS operates by precisely varying the voltage applied between the tip of the STM and the sample. This variation allows STS to investigate and map the localized density of electronic states on the surface being examined. These spectroscopic capabilities make STS an effective tool for investigating deeply into the electronic properties of materials.[61]

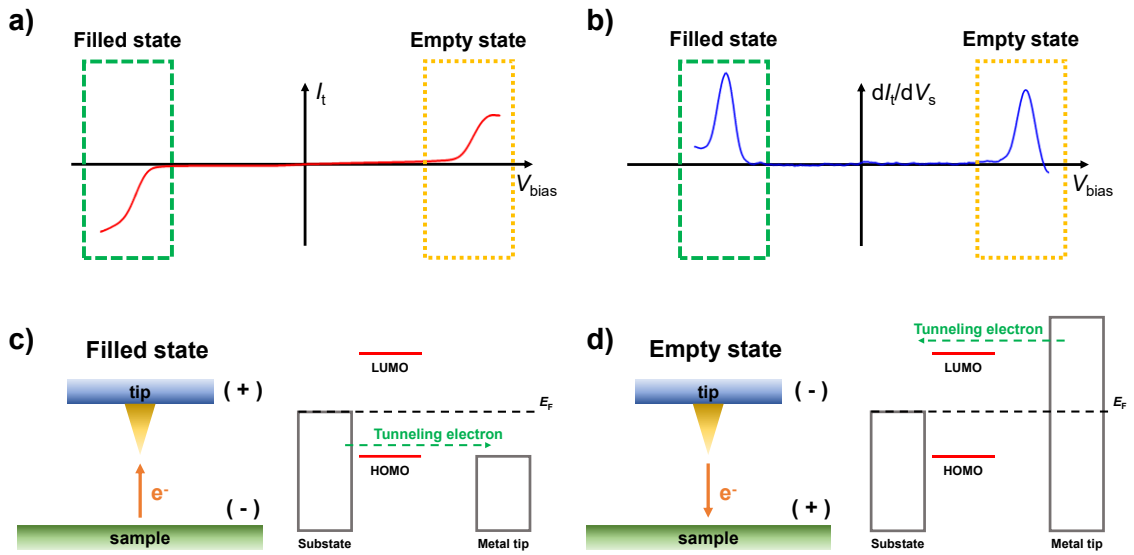

Figure 1-12. Typical features of **a)** I-V curve and **b)** d*I*/d*V* curves of organic semiconductor samples. Explanations of the mechanism for detecting **c)** filled state at negative bias voltage and **d)** empty state at positive bias voltage of a target organic molecule.

Using STS to measure conductance (d*I*/d*V*) offers distinct advantages over simple STM scans by providing insights into the electronic properties of materials at the specific energy level (**Figures 1-12a** and **1-12b**). While STM can visualize surface topography by keeping the tunneling current constant as the tip scans across a sample, STS evaluates the local electronic density of states (DOS) through d*I*/d*V* measurements, which directly correlate to the local DOS at specific energies (**Figures 1-12c** and **1-12d**). The d*I*/d*V* measurement process involves applying a small oscillating voltage (modulation amplitude) to the sample, in addition to the constant bias voltage. This oscillation allows for the differentiation of

the tunneling current with respect to the voltage, effectively measuring the conductance. Therefore, a lock-in amplifier is crucial in this setup. It processes the tunneling current by isolating the specific oscillation frequency of the input signal, thereby significantly enhancing the signal-to-noise ratio. This method efficiently filters out noise not matching the reference signal's phase and period, resulting in a cleaner, more accurate representation of the sample's electronic states. STS technology provides a conductance spectrum versus sample bias voltage by gradually varying the bias voltage across the range while recording the dI/dV signal at each step. This STS spectrum reveals the DOS of the sample and can also offer a map of how electronic states distribute spatially.

1. 5. Objective and outline of this doctoral thesis

In this thesis, I focused on the precise analysis of the electronic properties of MR-TADF molecules for a deeper understanding of the TADF mechanism. In particular, the investigation of the spatial distribution of the delicate MO configuration and the analysis of resulting multiple short-range CT characteristics in the organic molecular structure of MR-TADF molecules is expected to provide novel perspectives for the optimized design of highly efficient MR-TADF molecules. The outline of this thesis is as follows.

In Chapter 2, I analyzed the impact of partial planarization on the photophysical properties of MR-TADF molecules using dibenzo[1,4]azaborine derivatives. Specifically, to analyze the electrical properties of the molecules, I utilized the STEOM-DLPNO-CCSD method, which is used to calculate the properties of excited states based on wave functions. This advanced computational approach allowed us to accurately predict and understand the excited state and difference spin density plots essential for understanding the photophysical properties and RISC process of these MR-TADF molecules.

In Chapter 3, I experimentally investigated the electronic structure and characteristics of single MR-TADF molecules using scanning tunneling microscopy/spectroscopy (STM/STS). I investigated the local DOS based on the position of the heteroatoms that function as donors and accepter of MR-TADF by positioning the tip on each location. Also, the ionization energy and electron affinity of the DABNA-1 molecule in 1-ML NaCl/Au(111) were obtained based on the STS spectrum. In particular, I was successful in visualizing FMOs, which is important in determining TADF properties. With this visualization of FMOs, I confirmed that DABNA-1 Molecule also has well-separated HOMO and LUMO with multi-site overlap.

These research efforts have provided direct insight into the electronic structure underlying the TADF mechanism and improved our understanding of the factors affecting the efficiency and performance of

MR-TADF molecules. I also demonstrate the potential of the STM technique for the investigation of electrical characteristics in single MR-TADF molecules and briefly discuss the following experiments about MR-TADF material analysis using STM in conclusion.

1.6. References

[1] Portilla, L.; Loganathan, K.; Faber, H.; Eid, A.; Hester, J.; Tentzeris, M.; Fattori, M.; Cantatore, E.; Jiang, C.; Nathan, A.; Fiori, G.; Ibn-Mohammed, T.; Anthopoulos, T.; Pecunia, V. Wirelessly powered large-area electronics for the Internet of Things. *Nat. Electron.* **2023**, *6*, 10−17.

[2] Wen, D.; Sun, D.; Huang, P.; Huang, W.; Su, M.; Wang, Y.; Han, M.; Kim, B.; Brugger, J.; Zhang, H.; Zhang, X. Recent progress in silk fibroin-based flexible electronics. *Microsyst. Nanoeng.* **2021**, *7*, 35.

[3] Song, S.; Kim, J.; Kwon, S.; Jo, J.; Park, S.; Kim, Y. Recent Progress of Optoelectronic and All-Optical Neuromorphic Devices: A Comprehensive Review of Device Structures Materials, and Applications. *Adv. Intell. Syst.* **2021**, *3*, 2000119.

[4] Shekhar, S.; Bogaerts, W; Chrostowski, L.; Bowers, J.; Hochberg, M.; Soref, R.; Shastri, B. Roadmapping the next generation of silicon photonics. *Nat. Commun.* **2024**, *15*, 751.

[5] Hwang, S.; Tao, H.; Kim, D.; Cheng, H.; Song, J.; Rill, E.; Brenckle, M.; Panilaitis, B.; Won S, Kim.; Y Song, Y.; Yu, K.; Ameen A.; Li, R.; Su, Y.; Yang, M.; Kaplan, D.; Zakin, M.; Slepian, M.; Huang, Y.; Omenetto, F.; Rogers, J. A. Physically Transient Form of Silicon Electronics. *Science* **2012**, *337*,1640−1644.

[6] Dimitrakopoulos, C.; Malenfant, P. Organic Thin Film Transistors for Large Area Electronics. *Adv. Mater.* **2002**, *14*, 99−117.

[7] Sekitani, T.; Someya, T. Stretchable, Large-area Organic Electronics. *Adv. Mater.* **2010**, *22*, 2228−2246.

[8] Pang, S.; Hernandez, Y.; Feng, X.; Müllen, K. Graphene as Transparent Electrode Material for Organic Electronics. *Adv. Mater.* **2011**, *23*, 2779−2795.

[9] Fahlman, M.; Fabianom, S.; Gueskine, V.; Simon, D.; Berggren, M.; Crispin, X. Interfaces in organic electronics. *Nat. Rev. Mater.* **2019**, *4*, 627−650.

[10] McCulloch, I.; Chabinyc, M.; Brabec, C.; Nielsen, C.; Watkins, S. Sustainability considerations for organic electronic products. *Nat. Mater.* **2023**, *22*, 1304–1310.

[11] Friederich, P.; Fediai, A.; Kaiser, S.; Konrad, M.; Jung, N.; Wenzel, W. Toward Design of Novel Materials for Organic Electronics. *Adv. Mater.* **2019**, *31*, 1808256.

[12] Geffroy, B.; le, Roy, P.; Prat, C. Organic light-emitting diode (OLED) technology: materials, devices and display technologies. *Polym. Int.* **2006**, *55*, 572−582.

[13] Salehi, A.; Fu, X.; Shin, D.; So, F. Recent Advances in OLED Optical Design, *Adv. Funct. Mater.* **2019**, *29*, 1808803.

[14] Hong, G.; Gan, X.; Leonhardt, C.; Zhang, Z.; Seibert, J.; Busch, J.; Bräse, S. A Brief History of OLEDs—Emitter Development and Industry Milestones. *Adv. Mater.* **2021**, *33*, 2005630.

[15] Holmes-Siedle, A. Electronic structure of organic semiconductors. *Nature* **1975**, *255*, 13.

[16] Chen, H.; Leem J.; Lin, B.; Chen, S.; Wu, S. Liquid crystal display and organic light-emitting diode display: present status and future perspectives. *Light: Sci. Appl.* **2018**, *7*, 17168.

[17] Huang, Y.; Hsiang, E.; Deng, M.; Wu, S. Mini-LED, Micro-LED and OLED displays: present status and future perspectives. *Light: Sci. Appl.* **2020**, *9*, 105.

[18] Helfrich, W.; Schneider, W. G. Recombination Radiation in Anthracene Crystals. *Phys. Rev. Lett.* **1965**, *14*, 7.

[19] Tang, C. W.; VanSlyke, S. A. Organic electroluminescent diodes. *Appl. Phys. Lett.* **1987**, *51*, 913.

[20] Adachi, C.; Tokito, S.; Tsutsui, T.; Satio S. Electroluminescence in Organic Films with Three-Layer Structure. *Jpn. J. Appl. Phys*. **1988**, *27*, 269−271.

[21] Nakanotani, H.; Masui, K.; Nishide, J.; Shibata, T.; Adachi, C. Promising operational stability of high-efficiency organic light-emitting diodes based on thermally activated delayed fluorescence. *Sci. Rep.* **2013**, *3*, 2127.

[22] Jou, J.; Kumar, S.; Agrawal, A.; Li, T.; Sahoo, S. Approaches for fabricating high efficiency organic light emitting diodes. *J. Mater. Chem. C*, **2015**, *3*, 2974.

[23] Wei, Q.; Fei, N.; Islam, A.; Lei, T.; Hong, L.; Peng, R.; Fan, X.; Chen, L.; Gao, P.; Ge, Z. Small-Molecule Emitters with High Quantum Efficiency: Mechanisms, Structures, and Applications in OLED Devices. *Adv. Opt. Mater.* **2018**, *6*, 1800512.

[24] Zou, S.; Shen, Y.; Xie, F.; Chen, J.; Li, Y.; Tang, J. Recent advances in organic light-emitting diodes: toward smart lighting and displays. *Mater. Chem. Front.* **2020**, *4*, 788−820.

[25] Nayak, D.; Choudhary, R. A survey of the structure, fabrication, and characterization of advanced organic light emitting diodes. *Microelectron. Reliab.* **2023**, *144*, 114959.

[26] Pope, M.; Kallmann, H. P.; Magnante, P. Electroluminescence in Organic Crystals. *J. Chem. Phys.* **1963**, *38*, 2042−2043.

[27] Rothberg L. J.; Andrew J. L. Status of and prospects for organic electroluminescence. *J. Mater. Res.*, **1996**, *11*, 12.

[28] Köhler, A.; Bässler, H. Triplet states in organic semiconductors. *Mater. Sci. Eng.* **2009**, *66*, 71−109.

[29] Tsutsui, T.; Aminaka, E.; Lin, C. P.; Kim D. -U. Extended molecular design concept of molecular materials for electroluminescence: sublimed–dye films, molecularly doped polymers and polymers with chromophores. *Philos. Trans. R. Soc., A* **1725**, *355*, 801−814.

[30] Wong, M. Y.; Zysman-Colman, E. Purely Organic Thermally Activated Delayed Fluorescence Materials for Organic Light-Emitting Diodes. *Adv. Mater.* **2017**, *29*, 1605444.

[31] Teng, J. M.; Wang, Y. F.; Chen, C. F. Recent progress of narrowband TADF emitters and their applications in OLEDs. *J. Mater. Chem. C* **2020**, *8*, 11340−11353.

[32] Monkman, A. Why Do We Still Need a Stable Long Lifetime Deep Blue OLED Emitter? *ACS Appl. Mater. Interfaces* **2022**, *14*, 18, 20463−20467.

[33] Ha, J. M.; Hur, S. H.; Pathak, A.; Jeong, J. E.; Woo, H. Y. Recent advances in organic luminescent materials with narrowband emission. *NPG Asia Mater.* **2021**, *13*, 53.

[34] Jiao, Y.; Li, M.; Wang, N.; Lu, T.; Zhou, L.; Huang, Y.; Lu, Z.; Luo, D.; Pu, X. A facile color-tuning strategy for constructing a library of Ir(III) complexes with fine-tuned phosphorescence from bluish green to red using a synergetic substituent effect of -OCH_3 and -CN at only the C-ring of C^N ligand. *J. Mater. Chem. C*, **2016**, *4*, 4269.

[35] Minaev, B.; Baryshnikov, G.; Agren, H. Principles of phosphorescent organic light emitting devices. *Phys. Chem. Chem. Phys.*, **2014**, *16*, 1719.

[36] Baryshnikov, G.; Minaev, B.; Agren, H. Theory and Calculation of the Phosphorescence Phenomenon. *Chem. Rev.* **2017**, *117*, 6500−6537.

[37] Baldo, M. A.; O'Brien, D. F.; You. Y.; Shoustikov, A.; Sibley, S.; Thompson, M. E.; Forrest, S. R. Highly efficient phosphorescent emission from organic electroluminescent devices. *Nature* **1998**, *395*, 151.

[38] Adachi, C.; Baldo, M. A.; Thompson, M. E.; Forrest, S. R. Nearly 100% internal phosphorescence efficiency in an organic light emitting device. *J. Appl. Phys.* **2001**, *90*, 5048−5051.

[39] Uoyama, H.; Goushi, K.; Shizu, K.; Nomura, H.; Adachi, C. Highly Efficient Organic Light-Emitting Diodes from Delayed Fluorescence. *Nature* **2012**, *492*, 234−238.

[40] Dias, F. B.; Bourdakos, K. N.; Jankus, V.; Moss, K. C.; Kamtekar, K. T.; Bhalla, V.; Santos, J.; Bryce, M. R.; Monkman, A. P. Triplet Harvesting with 100% Efficiency by Way of Thermally Activated Delayed Fluorescence in Charge Transfer OLED Emitters. *Adv. Mater.* **2013**, 25, 3707−3714.

[41] Hirata, S.; Sakai, Y.; Masui, K.; Tanaka, H.; Lee, S. Y.; Nomura, H.; Nakamura, N.; Yasumatsu, M.; Nakanotani, H.; Zhang, Q.; Shizu, K.; Miyazaki, H.; Adachi, C. Highly Efficient Blue Electroluminescence Based on Thermally Activated Delayed Fluorescence. *Nat. Mater.* **2015**, *14*, 330−336.

[42] Zhang, Q.; Li, B.; Huang, S.; Nomura, H.; Tanaka, H.; Adachi, C. Efficient Blue Organic Light-Emitting Diodes Employing Thermally Activated Delayed Fluorescence. *Nat. Photon.* **2014**, *8*, 326−332.

[43] Nakanotani, H; Tsuchiya, Y; Adachi C. Thermally-activated Delayed Fluorescence for Light-emitting Devices. *Chem. Lett.* **2021**, *50*, 938−948.

[44] Hirata, S.; Head-Gordon M. Time-dependent density functional theory within the Tamm-Dancoff approximation. *Chem. Phys. Lett.* **1999**, 314, 291.

[45] Casida, M. E.; Huix-Rotllant, M. Progress in time-dependent density-functional theory. *Annu. Rev. Phys. Chem.* **2012**, 63, 287.

[46] Chen, X. -K.; Tsuchiya, Y.; Ishikawa, Y.; Zhong, C.; Adachi, C.; Brédas J. -L. A New Design Strategy for Efficient Thermally Activated Delayed Fluorescence Organic Emitters: From Twisted to Planar Structures. *Adv. Mater.* **2017**, 29, 1702767.

[47] Samanta, P. K.; Kim, D.; Coropceanu, V.; Brédas, J. L. Up-Conversion Intersystem Crossing Rates in Organic Emitters for Thermally Activated Delayed Fluorescence: Impact of the Nature of Singlet vs Triplet Excited States. *J. Am. Chem. Soc.* **2017**, 139, 4042−4051.

[48] El-Sayed, M. A. Spin-orbit coupling and the radiationless processes in nitrogen heterocyclics. *J. Chem. Phys.* **1963**, *38*, 2834−2838.

[49] Baba, M. Intersystem Crossing in the $^1n\pi^*$ and $^1\pi\pi^*$ States. *J. Phys. Chem. A* **2011**, *115*, 34, 9514−9519

[50] Hatakeyama, T.; Shiren, K.; Nakajima, K.; Nomura, S.; Nakatsuka, S.; Kinoshita, K.; Ni, J.; Ono, Y.; Ikuta, T. Ultrapure Blue Thermally Activated Delayed Fluorescence Molecules: Efficient HOMO-LUMO Separation by the Multiple Resonance Effect. *Adv. Mater.* **2016**, *28*, 2777−2781.

[51] Kim, H. J.; Yasuda, T. Narrowband Emissive Thermally Activated Delayed Fluorescence Materials. *Adv. Opt. Mater.* **2022**, *10*, 2201714.

[52] Mamada, M.; Hayakawa, M.; Ochi, J.; Hatakeyama, T. Organoboron-Based Multiple-Resonance Emitters: Synthesis, Structure-Property Correlations, and Prospects. *Chem. Soc. Rev.*, **2024**, *53*, 1624.

[53] Northey, T.; Penfold, T. J. The Intersystem Crossing Mechanism of an Ultrapure Blue Organoboron Emitter. *Org. Electron.* **2018**, *59*, 45−48.

[54] Lin, L.; Fan, J.; Cai L.; Wang C. -K. Excited state dynamics of new-type thermally activated delayed fluorescence emitters: theoretical view of light-emitting mechanism *Mol. Phys.*, **2018**, *116*, 19−28.

[55] Pershin, A.; Hall, D.; Lemaur, V.; Sancho-Garcia, J. C.; Muccioli, L.; Zysman-Colman, E.; Beljonne, D.; Olivier, Y. Highly Emissive Excitons with Reduced Exchange Energy in Thermally Activated Delayed Fluorescent Molecules. *Nat. Commun.* **2019**, *10*, 597.

[56] Wu, X.; Su, B. K.; Chen, D. G.; Liu, D.; Wu, C. C.; Huang, Z. X.; Lin, T. C.; Wu, C. H.; Zhu, M.; Li, E. Y.; Hung, W. Y.; Zhu, W.; Chou, P. T. The Role of Host-Guest Interactions in Organic Emitters Employing MR-TADF. *Nat. Photon.* **2021**, *15*, 780−786.

[57] Meng, G.; Liu, L.; He, Z.; Hall, D.; Wang, X.; Peng, T.; Yin, X.; Chen, P.; Beljonne, D.; Olivier, Y.; Zysman-Colman, E.; Wang, N.; Wang, S. Multi-Resonant Thermally Activated Delayed Fluorescence Emitters Based on Tetracoordinate Boron-Containing PAHs: Colour Tuning Based on the Nature of Chelates. *Chem. Sci.* **2022**, *13*, 1665−1674.

[58] dos Santos, J. M.; Chan, C. Y.; Tang, S.; Hall, D.; Matulaitis, T.; Cordes, D. B.; Slawin, A. M. Z.; Tsuchiya, Y.; Edman, L.; Adachi, C.; Olivier, Y.; Zysman-Colman, E. Color Tuning of Multi-Resonant Thermally Activated Delayed Fluorescence Emitters Based on Fully Fused Polycyclic Amine/Carbonyl Frameworks. *J. Mater. Chem. C* **2023**, *11*, 8263−8273.

[59] Stipe, B. C.; Rezaei, M. A.; Ho, W. Single-Molecule Vibrational Spectroscopy and Microscopy. *Science* **1998**, *280*, 5370.

[60] Swart, I.; Gross, L.; Liljeroth, P. Single-Molecule Chemistry and Physics Explored by Low-Temperature Scanning Probe Microscopy. *Chem. Commun.* **2011**, *47*, 9011−9023.

[61] Hoffman, J. E. Spectroscopic Scanning Tunneling Microscopy Insights into Fe-Based Superconductors. *Rep. Prog. Phys.* **2011**, *74*, 124513.

[62] Zoh, I.; Imai-Imada, M.; Bae, J.; Imada, H.; Tsuchiya, Y.; Adachi, C.; Kim, Y. Visualization of Frontier Molecular Orbital Separation of a Single Thermally Activated Delayed Fluorescence Emitter by STM. *J. Phys. Chem. Lett.* **2021**, *12*, 31, 7512−7518

[63] Bhattacharyya, K. Can TDDFT Render the Electronic Excited States Ordering of Azine Derivative? A Closer Investigation with DLPNO-STEOM-CCSD. *Chem. Phys. Lett.* **2021**, *779*, 138827.

Chapter II

Analysis of the Impact of Partial Planarization at Boron and Nitrogen Sites within MR-TADF Molecules on the Electronic and Photophysical Properties with Dibenzo[1,4]azaborine Derivatives

2. 1. Introduction

Since the DABNA-1 molecule demonstrated the potential for high color purity and efficiency of MR-TADF materials,[1] research into MR-TADF molecules has intensified. The structure of DABNA-1 is a PAH core containing one boron atom and two nitrogen atoms, with two phenyl groups substituted on the nitrogen. To achieve deeper blue emission, research has suggested that a weak electron donor ability should be introduced. Therefore, previous research reported materials substituting one nitrogen atom with an oxygen atom to maintain TADF performance and exhibit more blue-shifted emission.[2,3] These B-O-N molecules emitted deep blue around 430 nm but either did not show TADF properties[2] or had very low RISC rate constants (0.83×10^4 s^{-1}).[3] In this context, I focused on studying the mechanisms that achieve deep blue emission while exhibiting TADF activity. Since the reported MR-TADF materials with weak donors exhibited inconsistent TADF properties, understanding the conditions for the expression of TADF activity was also a primary research objective. Prof. Yamaguchi's group at Nagoya University synthesized a basic heterocyclic structure containing a dibenzo[1,4]azaborine core (BN1) containing a single boron and nitrogen pair and characterized its photophysical and electronic properties, including narrowband emission and MOs from this molecule (see **Figure 2-1**).[4] This minimal B-N arrangement serves as the fundamental unit for achieving effective HOMO-LUMO separation in heterocycles and is the simplest structure in terms of minimal building blocks, compared to earlier MR-TADF materials structured around the core structure of DABNA.[1, 5-6] Building on the BN1 framework, I anticipated that introducing a planar, ring-fused configuration using triarylborane and/or triarylamine would enhance π-conjugation, thereby improving the photophysical properties of subsequent derivatives (BN2, BN3, and BN4). I specifically expected these enhanced photophysical properties to include TADF activity and focused on investigating the expression of TADF property.

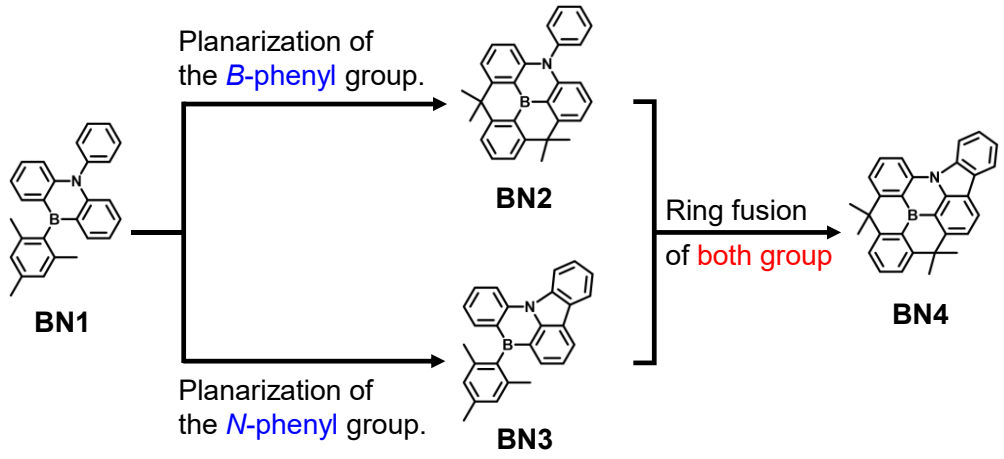

Figure 2-1. Schematic illustration of chemical structures of dibenzo[1,4]azaborine derivatives with planarization (BN1, BN2, BN3, and BN4).

In this study, I explore the photophysical properties of the aforementioned organic light emitters and their OLED performance in depth through computation and experiment. The investigations reveal that the original azaborine backbone (BN1) inherently lacks TADF properties. However, introducing planarity through the ring fusion of *B*- and *N*-phenyl groups instigates TADF activity. Notably, incorporating a carbazole unit significantly boosts SOC, with BN4 exhibiting the highest degree of planarity, demonstrating superior TADF properties among the series. Furthermore, the analysis indicated that the primary non-radiative decay of BN4 occurs mainly in the triplet state, which is a consideration for improving the efficiency and roll-off characteristics of EL. This is demonstrated by a comparison between theoretical EQE, which is strongly influenced by the dynamics of the non-radiative decay processes occurring in both S_1 and T_1 states, and experimental EQE.

2. 2. Result and discussion

2. 2. 1. Computational analysis using wave function-based methodologies

In an initial approach, I conducted theoretical studies using quantum chemical calculations for the BNs (BN1, BN2, BN3, and BN4). This included evaluating the ΔE_{ST} using a wave function-based methodology, specifically the SCS-CC2, as an alternative to DFT.[7] Our early investigations revealed that DFT calculations using the B3LYP/6-31G(d) functional showed significant discrepancies in the predicted energy levels (S_1, T_1) and ΔE_{ST} values, with *f* also diverging from the experimentally measured result.[8] The SCS-CC2 method matched the experimental results closely in certain cases, but the general agreement for all parameters of the BN was inconsistent. To address these inconsistencies, I introduced the STEOM-DLPNO-CCSD method.[9,10] The STEOM component of this method utilizes a similarity transformation approach that modifies the Hamiltonian to more accurately account for electron correlation effects in excited states. The DLPNO technique is applied to reduce the computational cost by focusing on relevant pairs of electrons in localized orbitals, making the calculations feasible even for larger systems. CCSD refers to a high-level quantum chemical method that includes both single and double electron excitations in the wave function, offering a robust description of electronic states. This advanced wave function-based approach provided more reliable results, closely matching experimental data for the energy levels and ΔE_{ST} of BNs. The values and comparison of the overall calculation results are shown in **Figure 2-2** and **Table 2-1**.

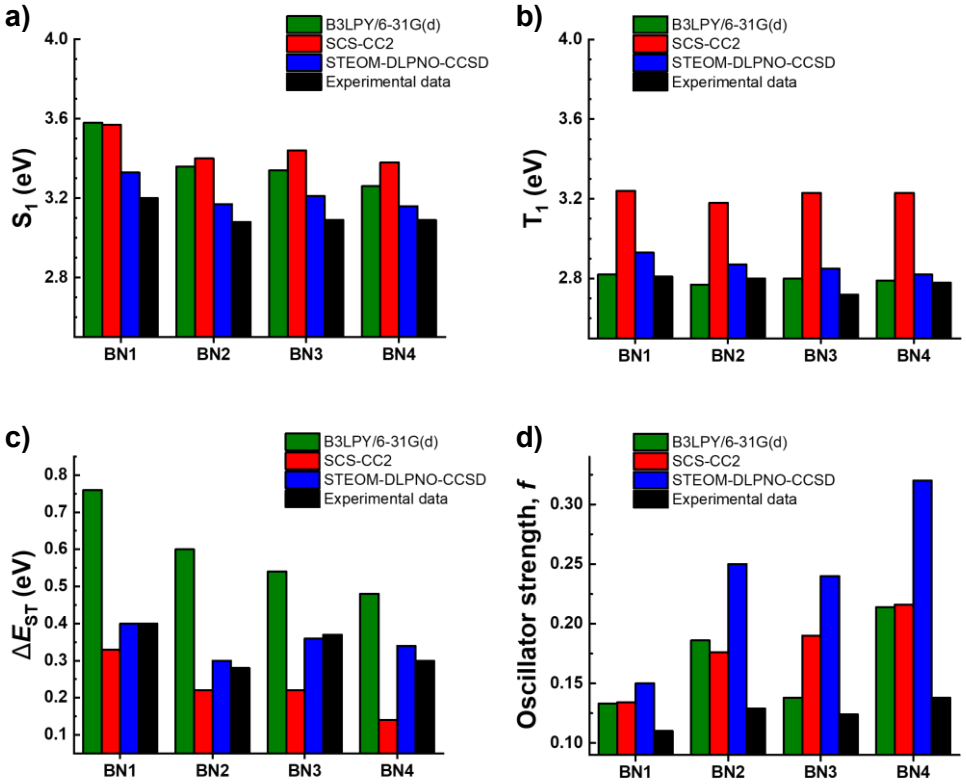

Figure 2-2. Comparison of various calculation results and experimental data (in toluene) of **BN1-4** for **a)** S_1 energies, **b)** T_1 energies, **c)** ΔE_{ST}, and **d)** *f*.

Table 2-1. Calculated excitation energies and *f* with various levels of theories and experimental results. The spin orbit-coupling value was also calculated with the STEOM-DLPNO-CCSD method.

	B3LPY/6-31G(d)				SCS-CC2				STEOM-DLPNO-CCSD					Experimental (in toluene) [a,c]				Experimental (in DPEPO) [b,c]		
	S_1 (eV)	T_1 (eV)	ΔE_{ST} (eV)	*f*	S_1 (eV)	T_1 (eV)	ΔE_{ST} (eV)	*f*	S_1 (eV)	T_1 (eV)	ΔE_{ST} (eV)	*f*	SOC (cm^{-1})	S_1 (eV)	T_1 (eV)	ΔE_{ST} (eV)	*f* [d]	S_1 (eV)	T_1 (eV)	ΔE_{ST} (eV)
BN1	3.58	2.82	0.76	0.133	3.57	3.24	0.33	0.134	3.33	2.93	0.40	0.15	0.00	3.20	2.81	0.40	0.110	3.18	2.82	0.36
BN2	3.36	2.77	0.60	0.186	3.40	3.18	0.22	0.176	3.17	2.87	0.30	0.25	0.00	3.08	2.80	0.28	0.129	3.06	2.78	0.28
BN3	3.34	2.80	0.54	0.138	3.44	3.23	0.22	0.190	3.21	2.85	0.36	0.24	0.19	3.09	2.72	0.37	0.124	3.07	2.76	0.29
BN4	3.26	2.79	0.48	0.214	3.38	3.23	0.14	0.216	3.16	2.82	0.34	0.32	0.12	3.09	2.78	0.30	0.138	3.07	2.83	0.24

[a] 1.0×10^{-5} mol L^{-1}. [b] Doping concentration of 1 wt%. [c] Onset value. [d] Estimated from absorption and emission spectra by the reported method in the literature.

Therefore, I estimated the detailed excited state of BNs with the STEOM-DLPNO-CCSD method, and **Figure 2-3** shows the calculated energy levels of singlet and triplet states, their ΔE_{ST} and SOCME, and *f* of S_1 state. In this analysis, considering the relative energy levels within the BN, especially the high energy of the S_2 level compared to the S_1, T_1, and T_2 levels, it is reasonable to focus on the latter

three levels for the evaluation of the emission process. Although the *f* for the S_1 level of the BN appears to be overestimated, this result is relevant in that it correlates with the trends observed due to π-conjugation enhancement in ring-fused molecular structures. Calculated ΔE_{ST} values typically fall within the range of 0.30 to 0.40 eV, showing good agreement of less than 0.05 eV with experimental results. I investigated the photophysical properties of the BNs predicted by these computer calculations. Compared to BN1, BN2, which extended the π-conjugation through the planarization of the *B*-phenyl, was predicted to have a lower ΔE_{ST} and higher *f* value. Interestingly, BN3, which formed a carbazole through the planarization of *N*-phenyl, exhibited a lesser decrease in ΔE_{ST} than BN2 but showed a higher SOCME value. BN4 exhibited similar changes observed in both BN2 and BN3.

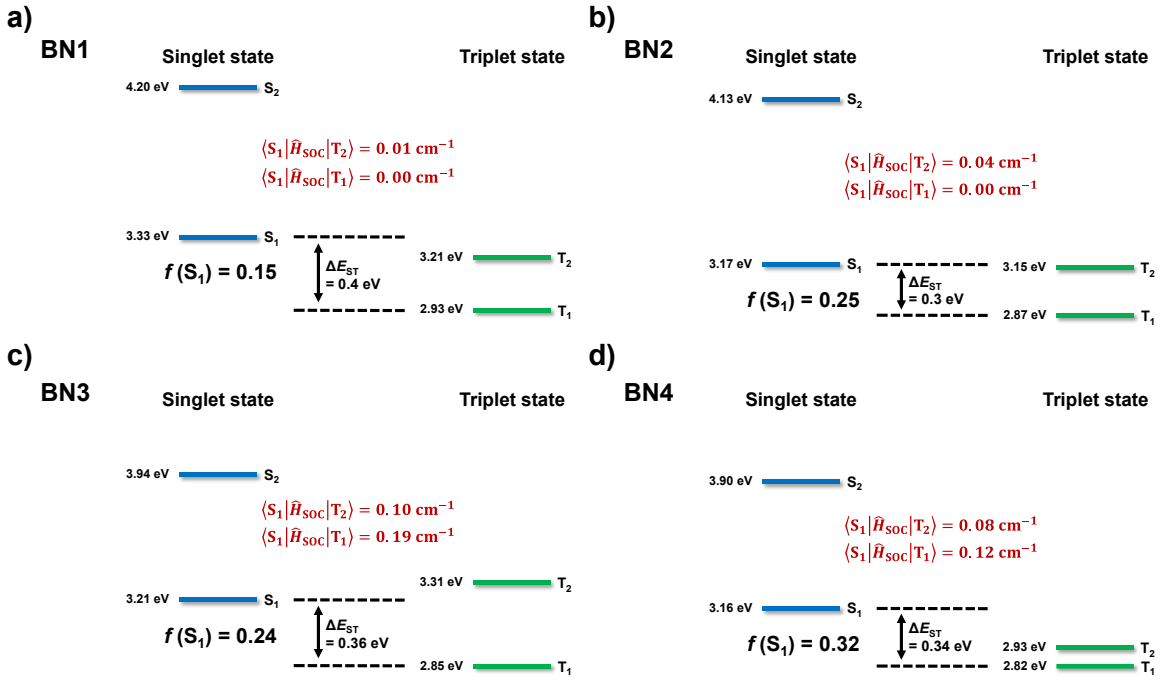

Figure 2-3. Calculated excited state energies for **a)** BN1, **b)** BN2, **c)** BN3, and **d)** BN4 at the STEOM-DLPNO-CCSD level of theory. Singlet (S_1, S_2) and triplet (T_1, T_2) levels were based on the geometry optimized for each level. *f* values were indicated for the S_1–S_0 transition at the S_1 state geometry. SOCME values were estimated by using initial and final state geometries.

To analyze the origin of SOCME improvement of BN3 and BN4, I simulated the hole and electron distributions of the difference spin density plots of S_1, T_1, and T_2 for each BN molecule with the same STEOM-DLPMO-CCSD method, which are shown in **Figure 2-4**. In the case of BN1 and BN2, the planarization from BN1 to BN2 led to a decrease in ΔE_{ST} due to the extension of delocalized CT, consistent with trends reported in previous research.[7] However, due to their similar distributions of holes and electrons in spin density plots, they showed negligible SOCME following El-Sayed's rules. These results are confirmed by the observation that the orbitals participating in both the singlet and

triplet excited states of the BN1 and BN2 molecules have similar conformations to the MOs formed by the resonance effect. In contrast, it was confirmed that the formation of carbazole significantly influences the distribution of holes and electrons in the excited state. In the case of BN3, where carbazole is formed, the influence of the resonance effect on the distribution in the S_1 state was significantly suppressed and exhibited a spatial separation characteristic of holes and electrons between the carbazole and other regions. Notably, in the T_1 state of BN3, the spatial separation characteristic is still observed, while the distribution influenced by the resonance effect is also discernible. The enhanced SOCME observed in BN3 materials appears to be due to the differences in electron transitions between the singlet and triplet excited states.

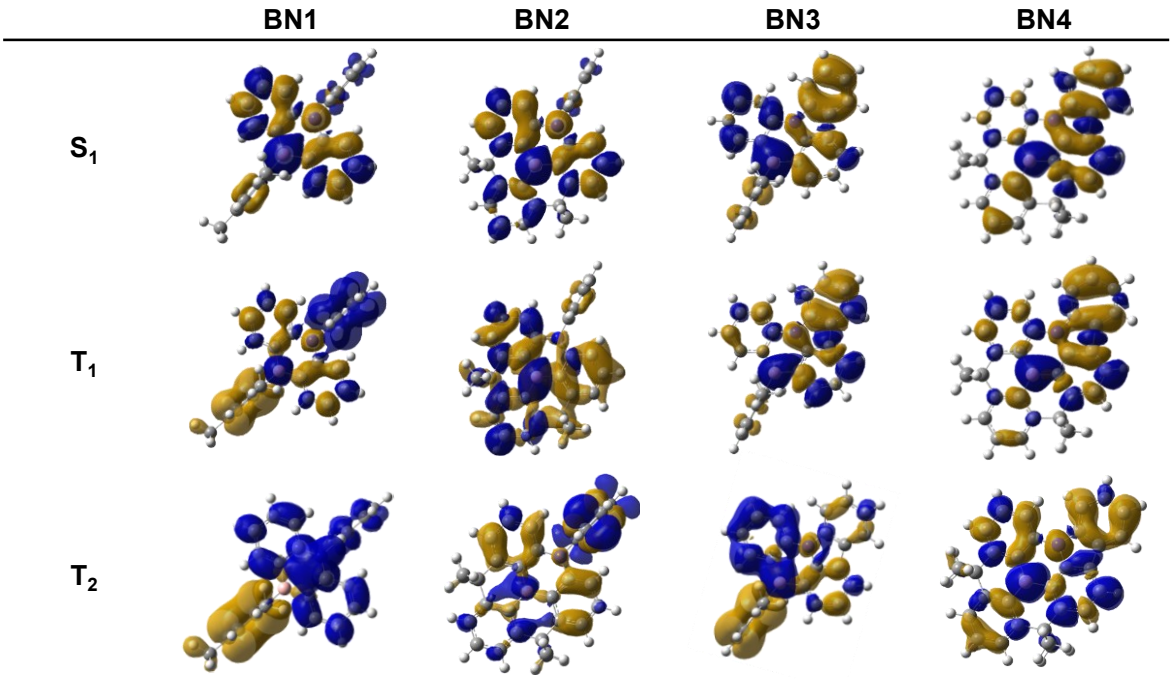

Figure 2-4. Difference density plots of BNs on each state, S_1, T_1, and T_2, at STEOM-DLPNO-CCSD level of theory. Distributions indicating blue and yellow denote electron-withdrawing and donating characteristics, respectively.

For BN4, it was predicted to exhibit both characteristics observed in both BN3 and BN2. However, a lower T_2 energy level can be observed when compared with BN2 and BN3. To confirm the impact of these T_2 energy levels, I conducted a comparative analysis of the theoretically calculated k_{RISC} values with BN3, which exhibits higher SOCME values. **Figure 2-5** shows the calculated k_{RISC} values for transitions from T_1 to S_1, from T_2 to S_1, and from $T_1 \leftrightarrow T_2$ to S_1. When considering only the transition from T_1 to S_1, BN3 ($k_{RISC}^{S_1 \leftarrow T_1}$: 1.39×10^1 s^{-1}) is expected to exhibit a higher k_{RISC} compared to BN4($k_{RISC}^{S_1 \leftarrow T_1}$: 1.23×10^1 s^{-1}). However, when considering the T_2 energy level, BN4 ($k_{RISC}^{S_1 \leftarrow T_2 \leftrightarrow T_1}$: 1.88×10^1 s^{-1}) is

predicted to exhibit a higher k_{RISC} value compared to BN3 ($k_{RISC}^{S_1 \leftarrow T_2 \leftrightarrow T_1}$: 1.40×10^1 s^{-1}). This is expected because the distribution of triplet excitons at the lowered T_2 energy level has increased, leading to a higher contribution to the RISC process.

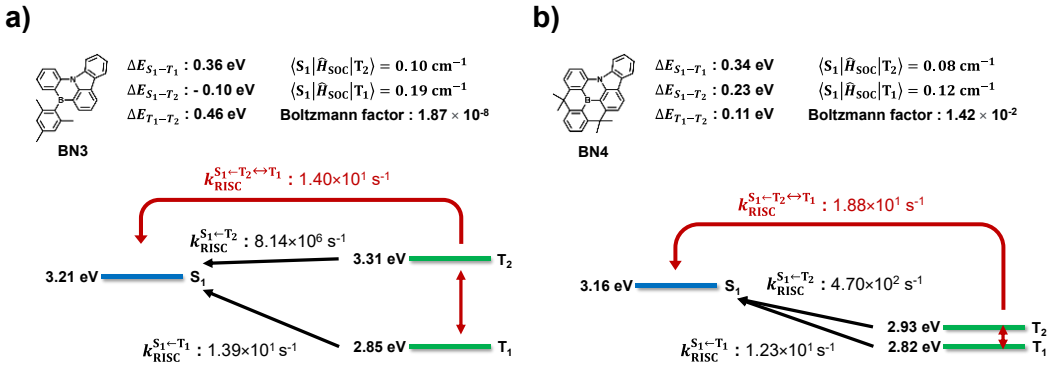

Figure 2-5. RISC process considering $T_1 \leftrightarrow T_2 \rightarrow S_1$ route in **a)** BN3 and **b)** BN4 molecule.

2. 2. 2. Detailed analysis of the photophysical properties of BNs molecules in solution

To experimentally confirm the electronic states of the BNs molecules predicted by the calculations, I first measured the photophysical properties of the molecules in a solution environment. This analysis primarily focused on the spectral characteristics and estimated values of photophysical properties exhibited by BNs in solution. **Figure 2-6** presents the ultraviolet-visible (UV-Vis) absorption and PL spectra of the BNs diluted in toluene solvent at a concentration of 1.0 × 10^{-5} mol L^{-1}. Based on previously reported methodologies, I used the integral of the molar absorption coefficient (ε), derived from the absorption component at the lowest energy, to estimate the experimental f for these fluorescence materials.[11-13] This method was also utilized to calculate the transition dipole moment (Q) and the radiative decay rate from the S_1 state (k_r^S) based on the absorption and emission spectra (**Table 2-2**). By measuring the photophysical properties of BNs molecules in solution and comparing them with the calculated results, I was able to verify the reliability of the computational outcomes and further discuss the impact of planarization.

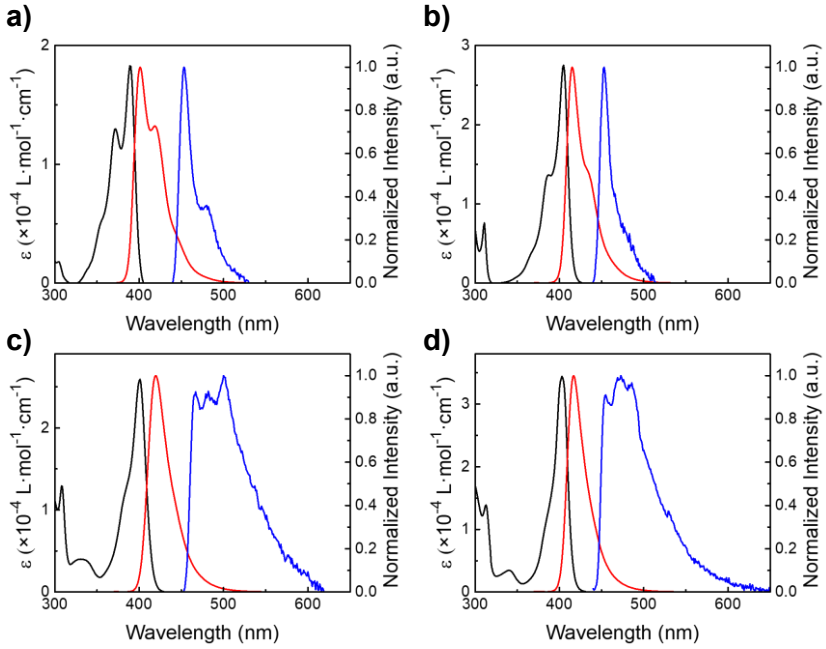

Figure 2-6. Absorption (black line), fluorescence (red line), and phosphorescence (blue line, at 77 K) spectra of **a)** BN1, **b)** BN2, **c)** BN3, and **d)** BN4 in toluene (1.0×10^{-5} mol L^{-1}).

Table 2-2. Photophysical values of BNs in toluene solution (1.0×10^{-5} mol L^{-1}).

Compounds	λ_{abs}[a] (nm)	ε[a] $\times 10^{-4}$ (L mol^{-1} cm^{-1})	λ_{flu}[b] (nm)	PLQY[c]	FWHM[a] (nm)	S_1[d] (eV)	T_1[d] (eV)	ΔE_{ST}[d] (eV)	f[e]	Q[e] (D)	k_r^S[e] (10^8 s^{-1})
BN1	389	1.83	401	0.98	36	3.20	2.81	0.40	0.110 (0.15)	1.564	1.35 (1.12)
BN2	405	2.75	415	0.98	28	3.08	2.80	0.28	0.129 (0.25)	1.925	1.51 (1.28)
BN3	401	2.59	420	0.86	29	3.09	2.72	0.37	0.124 (0.24)	2.085	1.42 (1.14)
BN4	403	3.44	417	0.86	25	3.09	2.78	0.30	0.138 (0.32)	2.428	1.67 (1.38)

[a] Absorption peak maxima of the lowest energy absorption band. [b] Emission peak maxima. [c] PLQY measured under inert gas conditions. [d] S_1 and T_1 are estimated from onset values of fluorescence and phosphorescence spectra. [e] f, transition dipole moment (Q), and radiative decay rate (k_r^S) are estimated from absorption and emission spectra by the reported method in the literature.[13] The values of f shown in parentheses are the computationally calculated values with the STEOM-DLPNO-CCSD level of theory.[9] The values of k_r^S shown in parentheses are obtained emission decay rate and PLQY.

All four compounds exhibited characteristic absorption bands at wavelengths longer than approximately 350 nm. Notably, these bands were deconvoluted using multi-component Gaussian curve fitting techniques (**Figure 2-7**), identifying an intense absorption peak around 400 nm, indicative of a short-range CT transition, a characteristic of the MR properties originating from the fused BN structure. The f, Q, and k_r^S rates were derived from the lowest absorption band. This result shows strong concordance with f from computational predictions and radiative decay rates based on k_r^S and PLQY. The experimentally derived f values were 0.110, 0.129, 0.124, and 0.138 for BN1, BN2, BN3, and BN4,

respectively, as shown in **Table 2-2**. These values closely align with the calculated values of 0.15, 0.25, 0.24, and 0.32, respectively. Notably, BN2, which features a *B*-phenyl fusion, exhibited slightly higher f values than BN3 with an *N*-phenyl fusion, both in experimental and computational results. The spectroscopic k_r^S values were approximately 20-25% higher than those estimated from transient emission decay measurements in toluene for all BN compounds.

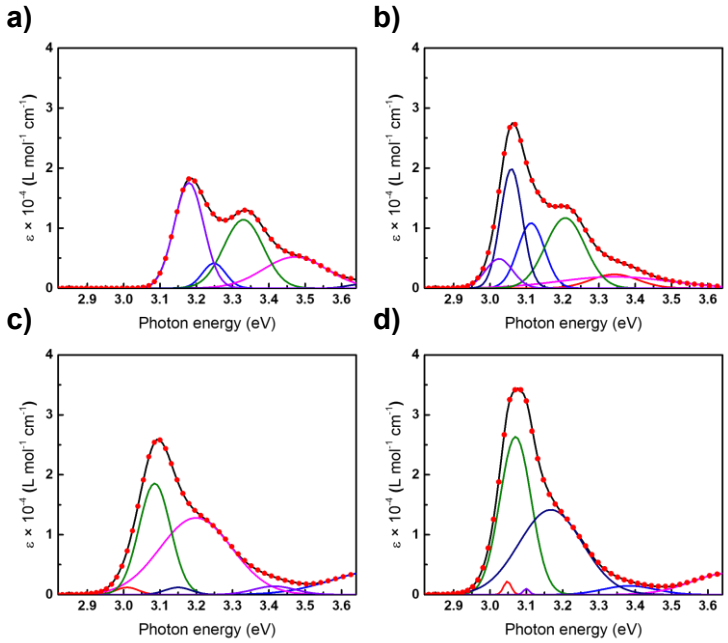

Figure 2-7. Absorbance characteristics of BN molecules in toluene solution; **a)** BN1, **b)** BN2, **c)** BN3, and **d)** BN4. Black lines are experimental data from UV-vis measurement. Colored lines represent fitting curves based on the Gaussian model: $\varepsilon_n(\nu) = A_n \exp(-(\nu-B_n)^2/2C_n^2)$ (n = 1, 2, 3…), where A_n is the amplitude, B_n is the average wavenumber and C_n is the distribution parameter. The dotted red lines are a summation of each fitting curve. Since the BNs showed strong absorption spectra by short-range CT between HOMO-LUMO, the summation of the Gaussian model fitting curves constituting the first absorption spectrum was used to obtain *f*, Q, and k_r^S values. The estimation method was followed within the literature.[12]

A detailed examination of the absorption bands reveals that the more planar molecular structure significantly suppresses the vibronic structure in both the absorption and fluorescence spectra. In particular, BN4, which incorporates a carbazole unit and most planar structure, exhibits the narrowest emission spectrum with a full width at half-maximum (FWHM) of 25 nm (49 meV). The fluorescence spectra of BN3 show no vibronic structure but are slightly broader at 29 nm when compared to BN4. This difference can be attributed to the CT-like spin distributions observed in theoretical analyses. Additionally, the planarization-induced expansion of π-conjugation has led to a slight bathochromic shift in the absorption and fluorescence spectra, with peak absorption maxima occurring at 389 nm for BN1, 405 nm for BN2, 401 nm for BN3, and 403 nm for BN4, respectively. As confirmed by computational analysis focusing on spin distributions, BN molecules with *N*-phenyl planarization (BN3

and BN4) showed phosphorescence spectra with mixed features of CT and vibrational structures. This contrasts with BN1 and BN2, showing narrow phosphorescence spectra. In addition, **Figures 2-8** and **2-9** show a comprehensive spectral analysis for a variety of solvents, showing that the fluorescence and phosphorescence spectra of all BN compounds are consistently similar, indicating low sensitivity to solvent polarity with respect to S_1 and T_1 energy states.

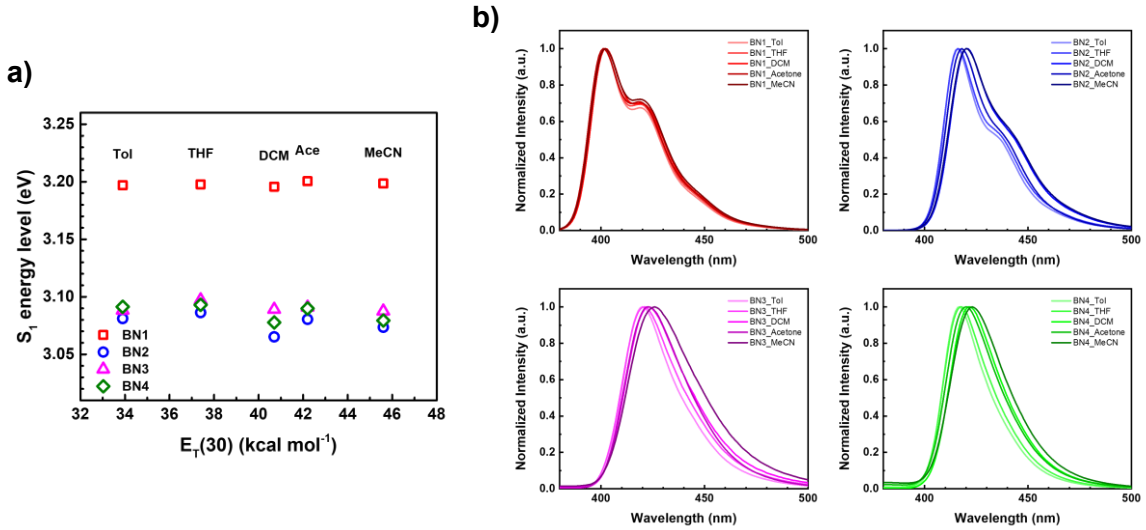

Figure 2-8. a) S_1 levels of BNs in various solvents in $E_T(30)$ scales as a solvent polarity parameter.[14] S_1 energy levels are estimated from the onset values of fluorescence spectra. **b)** Fluorescence spectra of BNs (red lines, blue lines, magenta lines, and green lines are BN1, BN2, BN3, and BN4, respectively).

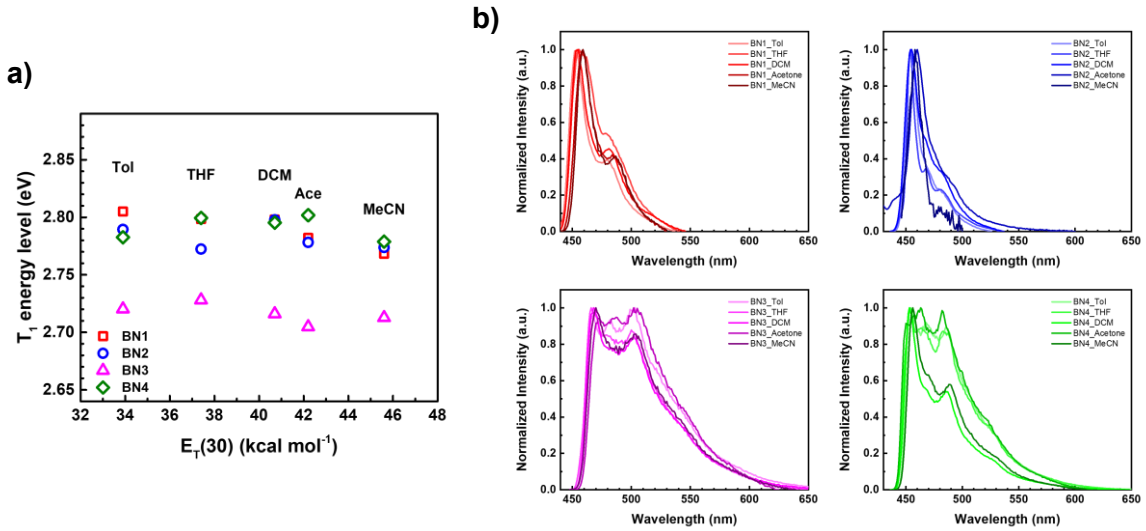

Figure 2-9. a) T_1 levels of BNs in various solvents in $E_T(30)$ scales as a solvent polarity parameter.[14] T_1 energy levels are estimated from the onset values of phosphorescence spectra. **b)** Phosphorescence spectra of BNs (red lines, blue lines, magenta lines, and green lines are BN1, BN2, BN3, and BN4, respectively).

Despite these findings, the delayed release detection of toluene presented a significant difficulty to all BNs. Notably, even BN4, which possesses the highest degree of molecular planarity and thus expected enhanced RISC efficiencies, exhibited only a very weak delayed emission, quantified as Φ_{PF}:Φ_{DF} = 85:1, as detailed in **Figure 2-10**. This subdued delayed emission behavior in toluene suggests intrinsic limitations within the BN series concerning non-radiative decay mechanisms, potentially due to the solvent's influence on RISC processes.

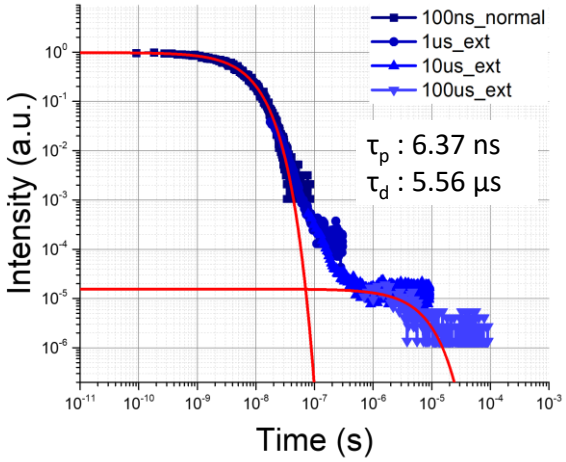

k_{ISC} : 1.28 × 10^7 s^{-1} < $k_r^S + k_{nr}^S$: 1.55 × 10^8 s^{-1}

k_{RISC} : 9.84 × 10^4 s^{-1} < k_{nr}^T : 1.67 × 10^5 s^{-1}

k_{RISC} and k_{ISC} are averaged value and k_r^S, k_{nr}^S and k_{nr}^T are maximum value corresponding to limited condition of k_{nr}^T = or k_{nr}^S = 0.

*Youichi Tsuchiya et al., *J. Phys. Chem. A* **2021**, *125*, 8074

Figure 2-10. Emission decay of BN4 in toluene solution was measured by a dynamic-range streak camera system; the difference from theoretical curves and observed plots are based on the IRF. Estimated value of k_{ISC}, k_{RISC} , k_r^S, k_{nr}^S, and k_{nr}^T from this spectrum also shown.[15]

2. 2. 3. Detailed analysis of TADF properties from the transient decay curve in DPEPO-doped films

Due to the weak TADF properties of all BN molecules in solution, I focused on their photophysical properties in solid films, where non-radiative decay is relatively less. I employed bis[2-(diphenylphosphino)phenyl] ether oxide (DPEPO), known for its high T_1 energy level (≈ 3.0 eV), as a host matrix to effectively confine the triplet energies of the BNs. I prepared BN-doped DPEPO films with a doping ratio of 1 wt%, which was optimized to suppress molecular aggregation. The spectroscopic analysis confirmed that the absorption and emission spectra of BNs in DPEPO, as shown in **Figures 2-11a, 11b, and Table 2-3**, closely correspond to the spectra observed in toluene, indicating that the BNs maintain their discrete molecular integrity without significant aggregation in the film environment.

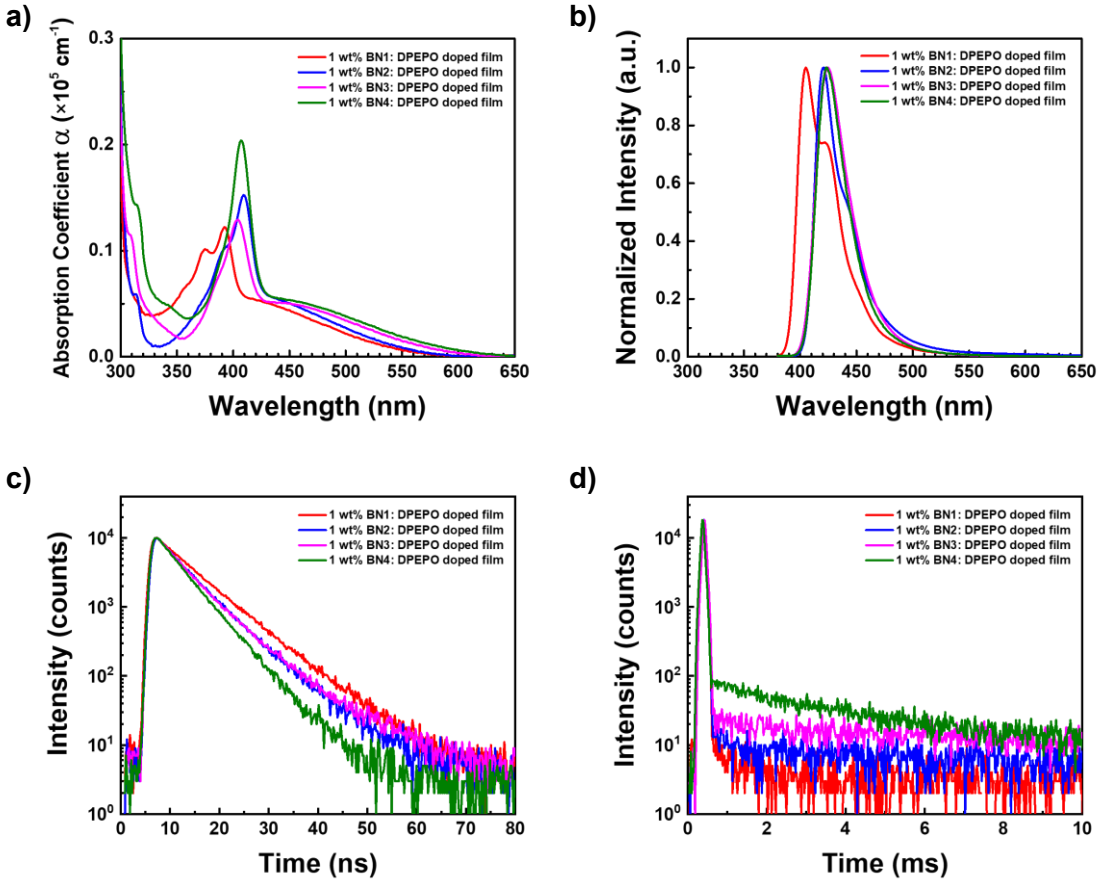

Figure 2-11. a) Absorption and **b)** fluorescence spectra of 1 wt% BNs in DPEPO film. Transient PL decay curves of **c)** prompt and **d)** delayed emissions for 1 wt% BNs in DPEPO film were also measured with a streak camera under the vacuum at 300 K.

Table 2-3. Estimated photophysical and rate constant values of 1 wt% BNs in DPEPO doped film.

Doped film	S_1[a] (eV)	T_1[a] (eV)	ΔE_{ST}[a] (eV)	τ_p[b] (ns)	τ_d[b] (ms)	Φ_{PF}[c]	Φ_{DF}[c]	Φ_{PLQY}[d]	k_r^S[c] (10^8 s^{-1})	max. k_{nr}^S[c,e] (10^7 s^{-1})	avg. k_{ISC}[c,e] (10^7 s^{-1})	avg. k_{RISC}[c,e] (s^{-1})	max. k_{nr}^T[c,e] (s^{-1})
BN1	3.18	2.82	0.36	7.03	-	0.82	-	0.821	1.17	2.55	1.27 ±1.27	-	-
BN2	3.06	2.78	0.28	5.70	16.24	0.70	0.06	0.762	1.24	3.86	3.25 ±1.93	41.80 ± 25	49.60
BN3	3.07	2.76	0.29	5.54	13.34	0.67	0.09	0.766	1.21	3.89	4.04 ±1.95	57.27 ±28	55.14
BN4	3.07	2.83	0.24	4.96	4.19	0.70	0.10	0.801	1.40	3.49	4.38 ±1.74	196.50 ±78	156.51

[a] Estimated from onset values of fluorescence and phosphorescence spectra. $\Delta E_{ST} = S_1 - T_1$. [b] Prompt and delayed emission lifetimes were estimated from the ns and ms range transient emission decay curves, respectively. [c] Values were estimated by the reported method in the literature. [d] Under inert gas condition. [e] Maxima values of k_{nr}^S and k_{nr}^T are related to the limited condition of $k_{nr}^T = 0$, and $k_{nr}^S = 0$, respectively. Maximum k_{ISC} and minimum k_{RISC} obtained from average rate constants with the range are relayed to k_{nr}^S and opposite values are related to k_{nr}^T.[15]

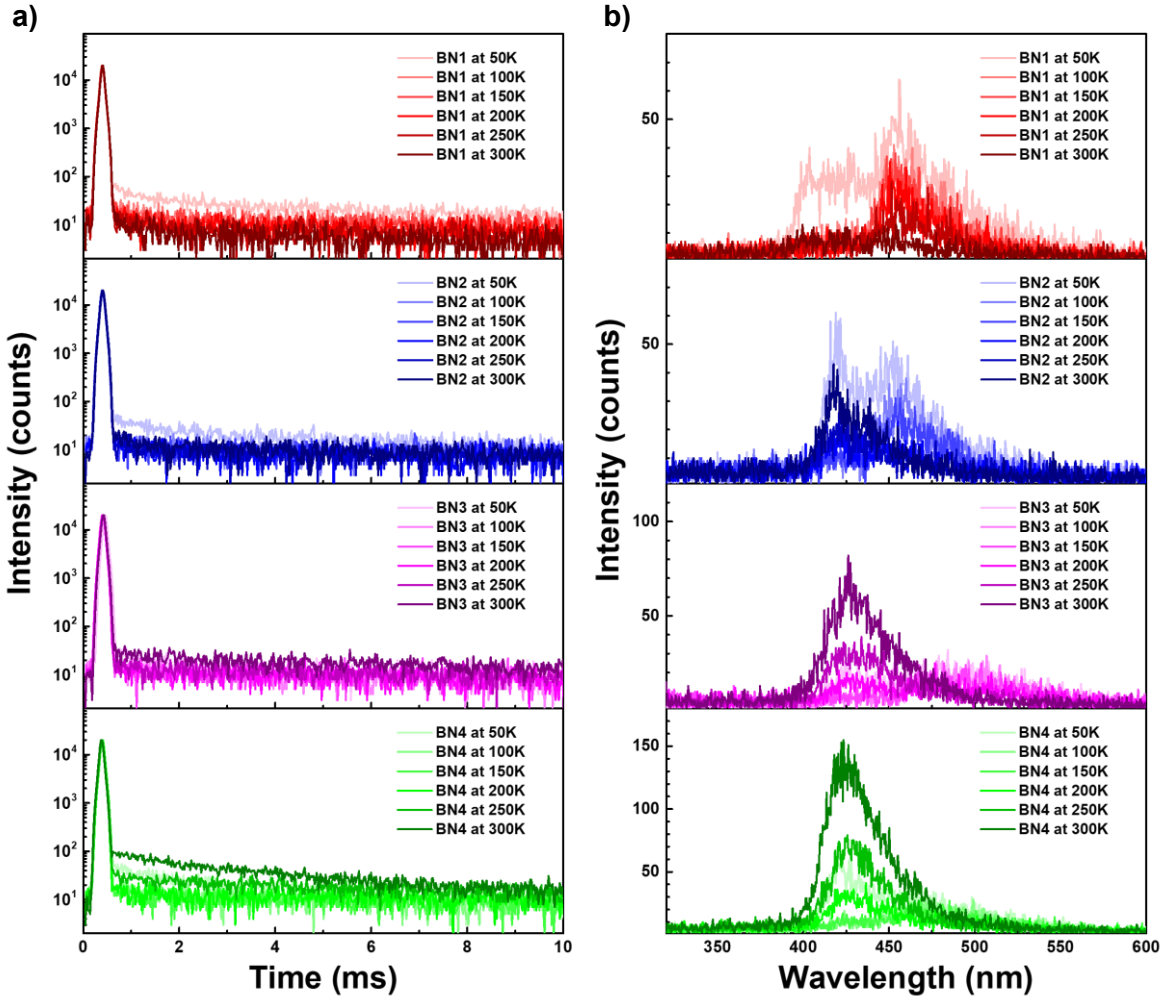

Figure 2-12. a) Temperature dependency of transient photoluminescence decay curves of 1 wt% BNs in DPEPO film. **b)** Transient emission spectra for delayed emission of 1-10 ms time range.

Interestingly, BN4 exhibited a much shorter delayed emission lifetime (τ_d = 4.2 ms) compared to BN2 and BN3 (16.2 and 13.3 ms, respectively), suggesting a more favorable alignment of the T_2 state in BN4 for efficient upconversion. Further analysis revealed quantitatively estimated intersystem crossing rates (k_{ISC}) for BN2, BN3, and BN4 to be 1.32 × 10^7, 2.09 × 10^7, and 2.64 × 10^7 s^{-1} respectively, with corresponding k_{RISC} values at 300 K being 66.8, 85.3, and 204.3 s^{-1}. These data suggest a direct RISC mechanism, given that phosphorescence is negligible in the delayed emission for these compounds, hence the application of the limiting condition k_{nr}^{T} = 0 (Among the ranges (±) of rate constants in **Table 2-3**, apply '-' for k_{ISC} and '+' for k_{RISC}).[15]

The theoretical k_{RISC} values were derived using the Marcus equation, which accounts for the relative population between the T_1 and T_2 levels (detailed estimation method of experimental reorganization energy estimation (λ) and SOCME are in **2. 4. Experimental section**).[16] The precise calculation results of RISC rates for each triplet pathway are outlined in **Table 2-4**. When considering the direct RISC from T_1 to S_1, the k_{RISC} value for BN3 was found to be slightly higher than that for BN4. However, when

the T_2 state was included in the analysis ($k_{RISC}^{S_1 \leftarrow T_2 \leftrightarrow T_1}$), the relative size of these values reversed. The incorporation of ΔE_{ST} values from spectral data into the Marcus equation alongside the measured k_{RISC} values facilitated the estimation of the SOCME. Experimental SOCME were calculated to be 0.068 and 0.049 cm^{-1} ($k_{nr}^{S} = 0$) or 0.115 and 0.075 cm^{-1} ($k_{nr}^{T} = 0$) for BN3 and BN4, respectively. This behavior is consistent with the observed direct RISC process without considering the T_2 contribution.

Table 2-4. Parameters for RISC process estimated by Marcus equation.

		BN1	BN2	BN3	BN4
Theoretical calculation values ($S_1 \leftarrow T_1$)	$\Delta E_{S_1-T_1}$ (eV) [a]	0.40	0.30	0.36	0.34
	$\mathrm{SOCME}_{S_1-T_1}$ (cm^{-1}) [a]	0.00	0.00	0.19	0.12
	$k_{RISC}^{S_1 \leftarrow T_1}$ (s^{-1}) [a,b]	–	–	1.39×10^{1}	1.23×10^{1}
Theoretical calculation values ($S_1 \leftarrow T_2$)	$\Delta E_{S_1-T_2}$ (eV) [a]	0.12	0.02	-0.10	0.23
	$\mathrm{SOCME}_{S_1-T_2}$ (cm^{-1}) [a]	0.01	0.04	0.10	0.08
	$k_{RISC}^{S_1 \leftarrow T_2}$ (s^{-1}) [a,b]	7.16×10^{2}	1.34×10^{6}	8.14×10^{6}	4.70×10^{2}
Theoretical calculation values ($S_1 \leftarrow T_2 \leftrightarrow T_1$)	$\Delta E_{T_1-T_2}$ (eV) [a]	0.28	0.28	0.46	0.11
	Boltzmann factor [a]	1.98×10^{-5}	1.98×10^{-5}	1.87×10^{-8}	1.42×10^{-2}
	$k_{RISC}^{S_1 \leftarrow T_2 \leftrightarrow T_1}$ (s^{-1}) [a,b]	1.42×10^{-2}	2.66×10^{1}	1.40×10^{1}	1.88×10^{1}
Limited condition	$k_{RISC}^{nrS=0}$ (s^{-1}) [c]	–	1.68×10^{1}	2.93×10^{1}	1.19×10^{2}
Experimental values (Emission spectrum)	ΔE_{ST} (eV) [d]	0.36	0.28	0.29	0.24
	$\mathrm{SOCME}_{S_1-T_1}$ (cm^{-1}) [b,c,d]	–	0.042	0.068	0.049
Experimental values (Marcus plot)	ΔE_{ST} (eV) [e]	–	–	0.065	0.121
	λ (eV) [e]	–	–	0.065	0.121
	$\mathrm{SOCME}_{S_1-T_1}^{\mathrm{effective}}$ (cm^{-1}) [e]	–	–	0.00059	0.00398
Limited condition	$k_{RISC}^{nrT=0}$ (s^{-1}) [c]	–	6.68×10^{1}	8.53×10^{1}	2.75×10^{2}
Experimental values (Emission spectrum)	ΔE_{ST} (eV) [d]	0.36	0.28	0.29	0.24
	$\mathrm{SOCME}_{S_1-T_1}$ (cm^{-1}) [b,c,d]	–	0.083	0.115	0.075
Experimental values (Marcus plot)	ΔE_{ST} (eV) [e]	–	–	0.099	0.083
	λ (eV) [e]	–	–	0.120	0.184
	$\mathrm{SOCME}_{S_1-T_1}^{\mathrm{effective}}$ (cm^{-1}) [e]	–	–	0.00065	0.00435

[a] Theoretical calculation values (Samanta et al. 2017). [b] $\Delta E_{S_1-T_x}$ employing as an activation energy. [c] Experimentally obtained emission decay at 300 K. [d] Fluorescence and phosphorescence spectra. [e] Marcus plot assuming in the normal region.

Moreover, using the Marcus plot, a graphical representation that helps estimate reaction rates from the activation energy of the reaction (**Figure 2-13**), the effective SOCMEs for the RISC processes of BN3 and BN4 were calculated to be approximately 0.0006 and 0.004 cm^{-1}, respectively. Remarkably, this shows that BN4 exhibits a SOCME that is an order of magnitude larger than that of BN3, as detailed in Table 2-4. Such findings conclusively indicate that the Tn state in BN4 substantially enhances the RISC process, significantly enhancing its TADF efficiency. This comprehensive investigation provides important insights into the RISC activity of BN molecules, particularly highlighting how the planar structural properties of BN4 molecules promote a more efficient RISC mechanism. This not only validates the theoretical model used but also emphasizes the importance of specific molecular configurations in enhancing the practical application of TADF materials.

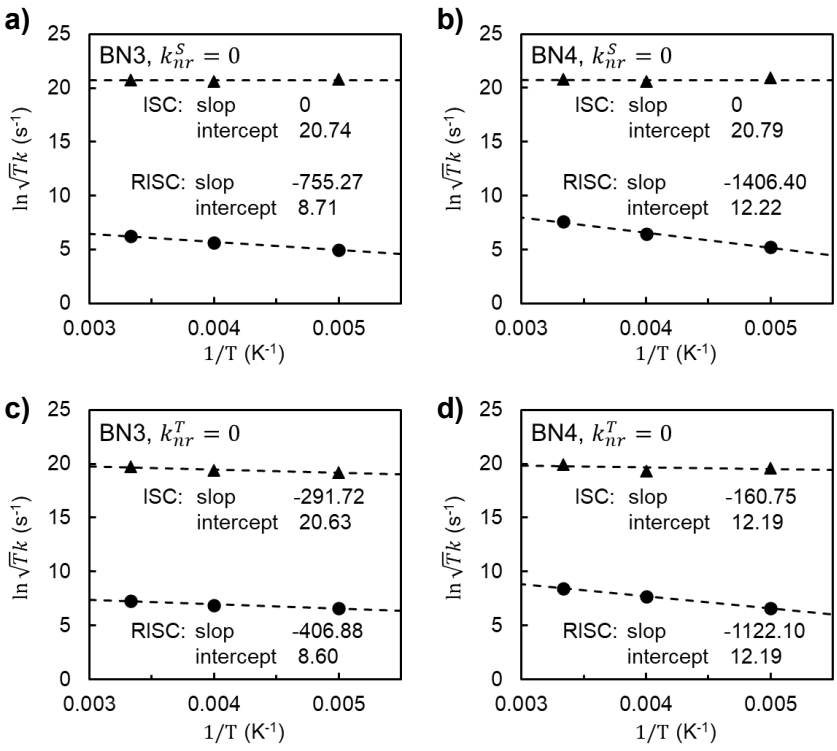

Figure 2-13. Marcus plots (ISC and RISC rate constants vs. inverse of temperature) for BN3 (**a**, **c**) and BN4 (**b**, **d**) in case of limit condition of k_{nr}^{S}=0 (**a**, **b**) and k_{nr}^{T}=0 (**c**, **d**).

2. 2. 4. Device performance employing BN4 as an emitter

Finally, I fabricated a device using BN4 as an emitter (see **Figure 2-14**), and the device structure is as follows.: indium tin oxide (ITO) /followed by layers of 1,1-bis[(di-4-tolylamino)phenyl]cyclohexane (TAPC, 35 nm) / 4,4′,4″-tris(carbazol-9-yl)triphenylamine (TCTA, 10 nm) / 1,3-bis(9-carbazol-9-yl)

benzene (mCP, 10 nm) / DPEPO doped 1 wt% BN4 (30 nm) / DPEPO layer (10 nm) / 2,2′,2"-(1,3,5-benzinetriyl)-tris(1-phenyl-1-H-benzimidazole) (TPBi, 45 nm) / LiF (0.8 nm) / aluminum (Al, 100 nm). The EL spectrum of this device was similar to the PL spectrum of BN4 in the DPEPO host with a maximum emission wavelength (λ_{ELmax}) of 423 nm and an FWHM of 31 nm. The device achieved Commission Internationale de l'Eclairage (CIE) coordinates of (0.17, 0.04) and an EQE_{max} of 9.1%.

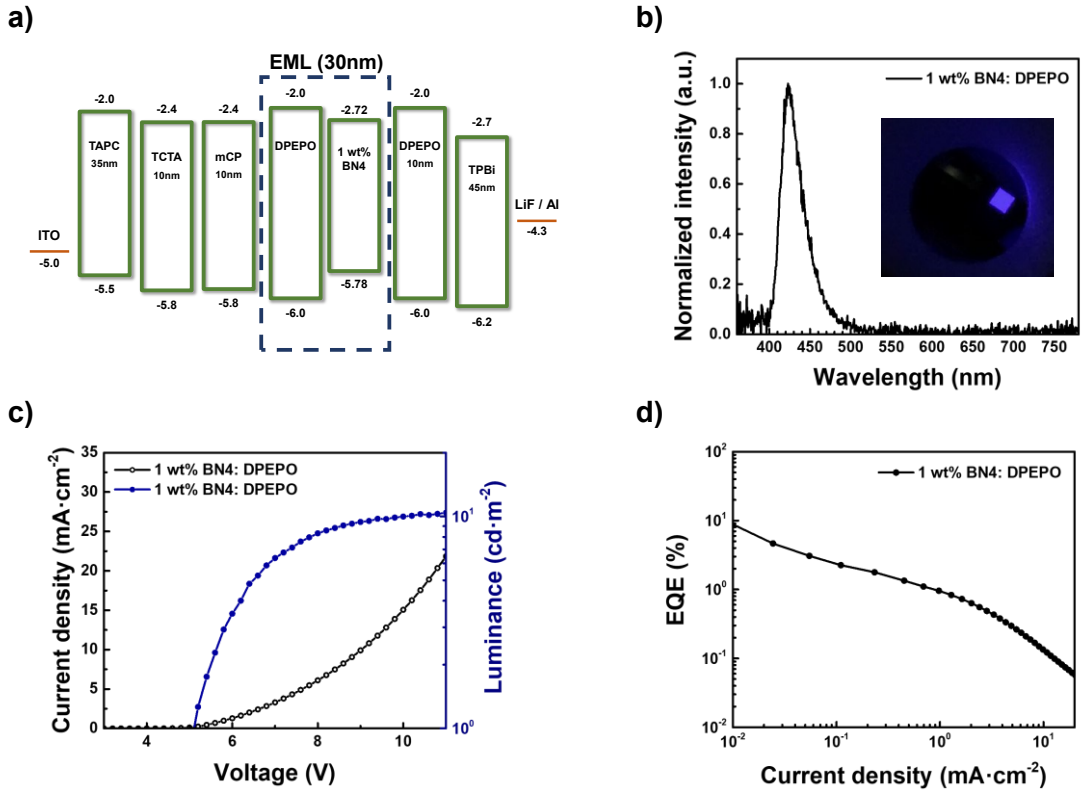

Figure 2-14. Device characteristics of BN4; **a)** Schematic device structure and energy level alignment, **b)** normalized EL spectra, **c)** J-V-L profile, and **d)** EQE-J curves.

To understand this device's efficiency, I explored the factors contributing to EQE_{max}, considering internal quantum efficiency (η_{int}), outcoupling efficiency (η_{out}), and charge balance factor (η_{CB}). The maximum external efficiency (EQE_{max}) of an OLED is defined by the product of the η_{int}, η_e, and η_{CB} as follows.

$$EQE_{max} = \eta_{int}\eta_{out}\eta_{CB} \tag{2.1}$$

η_{int} is determined by the exciton generation efficiency (η_{exc}) of the luminescent material multiplied by the PLQY (Φ_{PLQY}).

$$\eta_{int} = \eta_{exc}\Phi_{PLQY} \tag{2.2}$$

Based on the spin-statistics rule, it's explained that η_{exc} equals 0.25 for fluorescent materials and 1.00 for phosphorescent and TADF materials. However, examining the non-radiative deactivation efficiency of excitons in TADF materials for PL and EL (represented by Eqs. 2.3 and 2.4, both with $\Phi_r^T \approx 0$), it's incorrect to simplistically consider $\eta_{exc} = 1.00$ and thus $\eta_{int} = \Phi_{PLQY}$.[17-20]

$$\Phi_{nr}^{PL} = \Phi_{nr}^{S} + \Phi_{ISC}\Phi_{nr}^{T} + \sum_{n=1}^{\infty}(\Phi_{ISC}\Phi_{RISC})^n\left(\Phi_{nr}^{S} + \Phi_{nr}^{T}\right) \tag{2.3}$$

$$\Phi_{nr}^{EL} = (0.25 + 0.75\Phi_{RISC})\Phi_{nr}^{S} + (0.25\Phi_{ISC} + 0.75)\Phi_{nr}^{T} + \sum_{n=1}^{\infty}(\Phi_{ISC}\Phi_{RISC})^n\left(\Phi_{nr}^{S} + \Phi_{nr}^{T}\right) \tag{2.4}$$

The formulas for Φ_{nr}^{PL} and Φ_{nr}^{EL} clearly indicate that they yield the same values only if $\Phi_{nr}^{T} = 0$, i.e., $\Phi_{RISC} = 1$, is substituted. If the EQE is significantly lower than the maximum theoretical efficiency despite high PLQY, it suggests a substantial non-radiative deactivation from T_1. Designing TADF molecules to make $k_{nr}^{T} = 0$ is crucial for high EL efficiency. Considering the distribution of excitons, η_{int} for TADF materials is provided by the following equation.

$$\eta_{int} = \frac{1}{4}\left(\Phi_{PLQY} + 3\frac{\Phi_{DF}}{\Phi_{ISC}}\right) \tag{2.5}$$

This adjustment was important due to the non-negligible nonradiative decay from the T_1 state, which significantly impacts the overall device performance. By incorporating an outcoupling efficiency (often assumed to be 0.2 for devices with randomly oriented emitter molecules) and considering the presence of nonradiative decay pathways, I calculated theoretical EQE_{max} values as 16.0% and 9.2% for the limit condition of $k_{nr}^{T} = 0$ and $k_{nr}^{S} = 0$, respectively. the analysis revealed that the majority of nonradiative decay in the BN4-based OLED occurs from the T_1 state within the DPEPO host matrix. This finding emphasizes the importance of managing the nonradiative decay process in the design and optimization of TADF OLEDs, suggesting that careful material design and device engineering are required to maximize efficiency.

2. 3. Conclusion

In my research, I explored the fundamental azaborine components that facilitate MR-TADF properties. A crucial finding was that planarization through ring fusion, particularly of the *B*- or *N*-phenyl groups, significantly enhances the structural rigidity and is instrumental in exhibiting pronounced

MR characteristics. This structural modification results in a notably narrower emission spectrum. Specifically, the planarization of the *N*-phenyl moiety, as opposed to the *B*-phenyl group, not only reduced the FWHM and the ΔE_{ST} by extending π-conjugation but also improved the molecular SOCME and effectively suppressed vibronic structures in emission spectra. In particular, the ring fusion of *B*- and *N*-phenyl groups induces a synergistic effect, combining the two advantages to effectively enhance the MR-TADF properties. These findings further demonstrate that the TADF characteristics of BN molecules, which exhibit relatively high ΔE_{ST} values (0.24~0.36 eV), are largely influenced by SOCME. The incorporation of a carbazole unit and further planarization significantly lowered the T_2 state energy, which is critical in facilitating the RISC process. This structural optimization is crucial for enhancing the efficiency of the TADF mechanism. These molecular insights led to the development of OLEDs with BN4 that exhibit blue-violet emission with a peak wavelength (λ_{max}) of 423 nm. This device achieved an EQE of 9.1%, which is close to the theoretical maximum EQE of 9.2% when considering a limited condition with minimal contribution from non-radiative decay in the singlet state. Given that the PLQY of BN4 exceeds 80%, this result emphasizes the importance of minimizing non-radiative processes in the triplet state for the molecular design of efficient deep-blue MR-TADF OLEDs. Lastly, I compared the characteristics, utility, and costs of the computational methods used in this study. The summary of these comparisons can be found in **Table 2-5**. This comprehensive analysis not only highlights the potential of BN molecules in OLED applications but also illustrates the importance of molecular design, particularly strategic planarization, and functionalization, in dictating the efficiency and color properties of TADF OLEDs.

Table 2-5. Comparison of three different computational analysis method used in this study.

Calculation	B3LYP	SCS-CC2	STEOM-DLPNO-CCSD
Type	Hybrid functional method	Post–Hartree–Fock method	Post–Hartree–Fock method
Advantages	Relatively fast and computationally inexpensive; widely used; good for ground state properties	Better accuracy for excited states compared to DFT; good agreement for ΔE_{ST} values	Best accuracy among the three methods; good agreement with experimental S_1, T_1 levels, and ΔE_{ST} values
Disadvantages	Often inaccurate for excited state energies and transition properties	Still lower accuracy for singlet and triplet energies; more computationally demanding than DFT	Very computationally expensive
Computational Cost	Low	High	Very high
Usefulness for D-A Type TADF	Good for geometry optimizations, but may require correction methods for accurate excited states.	Limited; often not ideal for excited state properties	Best for accurate predictions of excited state properties
Usefulness for MR Type TADF	Provides large discrepancy with experimental results	Better agreement for ΔE_{ST} but not for each excited energy levels	Provides the best results for MR-TADF

2. 4. Experimental section

Fitting method for transient PL decay curves measured by streak camera

The transient PL decay curve measured by a streak camera system includes the considerable instrument-related function (IRF) related to the pumping laser, slit width in front of the photo-cathode, and emission distribution on the phosphor plate after the microchannel plate, etc. However, the data would be analyzed with the direct multi-exponential curve fitting in general. Because the transient PL data provided the very weak delayed emission component in this study, it required a more precise analysis. Therefore, all data was analyzed with the unusual fitting method considering the IRF.

When IRF data is provided, I would be able to employ the convolution fitting provided with some software. However, there are many cases in which the IRF data cannot be used. However, the IRF can be explained by the sum of several Gauss curves in many cases. Therefore, I employed an ex-gauss function for fitting the PL decay curve. The ex-gauss function is a convoluted function as explained by Eq. 2.6-2.8.

$$f(x;\,\mu,\sigma,\lambda) = f(x)\otimes g(x) = \frac{\lambda}{2}\exp\left[\frac{\lambda}{2}(2\mu+\lambda\sigma^2-2x)\right]\mathrm{erfc}\left(\frac{\mu+\lambda\sigma^2-x}{\sqrt{2}\sigma}\right) \tag{2.6}$$

$$f(x) = \begin{cases}\lambda\exp(-\lambda x), & (x\geq 0)\\ 0, & (x<0)\end{cases} \tag{2.7}$$

$$g(x) = \frac{1}{\sqrt{2\pi}\sigma}\exp\left[-\frac{(x-\mu)^2}{2\sigma^2}\right] \tag{2.8}$$

where $\mathrm{erfc}(x)$ is a complementary error function for the Gauss function defined as Eq. 2.9.

$$\mathrm{erfc}(x) \equiv \frac{2}{\sqrt{\pi}}\int_x^\infty \exp(-x^2)dx \tag{2.9}$$

For the single exponential decay containing simple IRF explained with a single Gauss curve, e.g., fluorescence emission decay, Eq. 2.6 can be rewritten as Eqs. 2.10-2.12.

$$I_{FL}(t) = f(t)\otimes g(t) = \frac{A}{2}\exp\left[\frac{k_{FL}}{2}(2\mu+k_{FL}\sigma^2)\right]\mathrm{erfc}\left(\frac{\mu+k_{FL}\sigma^2-t}{\sqrt{2}\sigma}\right)\exp(-k_{FL}t) \tag{2.10}$$

$$f(t) = \begin{cases}A\exp(-k_{FL}t), & (t\geq 0)\\ 0, & (t<0)\end{cases} \tag{2.11}$$

$$g(t) = \frac{1}{\sqrt{2\pi}\sigma}\exp\left[-\frac{(t-\mu)^2}{2\sigma^2}\right] \tag{2.12}$$

The expanded equation for multi-exponential decay with IRF with multi-gauss function can be written by Eqs. 2.13-2.14. The formula can be written as multiple ex-gauss functions for the multiple exponential decays.

$$I(t) = \sum_{n=1}^{n}\left\{R_n\left[\sum_{m=1}^{m} I_m(t_n, A_{\mathrm{m}}, k_m, \mu_n, \sigma_n)\right]\right\} \tag{2.13}$$

$$I_m(t_n, A_m, k_m, \mu_n, \sigma_n) = \frac{A_m}{2}\exp\left[\frac{k_m}{2}(2\mu_n + k_m{\sigma_n}^2)\right]\mathrm{erfc}\left(\frac{\mu_n + k_m{\sigma_n}^2 - t_n}{\sqrt{2}\sigma_n}\right)\exp(-k_m t_n) \tag{2.14}$$

R_n explained the relative intensity for each ex-gauss function and t_n is $t - \mu_n + \mu_1$. The deconvoluted exponential curve can be written by Eq. 2.15.

$$I_{dec}(t) = \sum_{n=1}^{n} R_n \times \sum_{n=1}^{n}[A_n \exp(-k_n t)] \tag{2.15}$$

The actual formula of Eq. 2.13 can be written as multiple ex-gauss functions for multiple exponential decays. To analyze the TADF on the three-state system, for example, the fitting curve for bi-exponential decay with three Gauss curves as IRF can be written by Eqs. 2.16-2.18.

$$\begin{aligned} I(t) = {} & R_1\left[I_p(t_1, A_p, k_p, \mu_1, \sigma_1) + I_d(t_1, A_d, k_d, \mu_1, \sigma_1)\right] \\ & + R_2\left[I_p(t_2, A_p, k_p, \mu_2, \sigma_2) + I_d(t_2, A_d, k_d, \mu_2, \sigma_2)\right] \\ & + R_3\left[I_p(t_3, A_p, k_p, \mu_3, \sigma_3) + I_d(t_3, A_d, k_d, \mu_3, \sigma_3)\right] \end{aligned} \tag{2.16}$$

$$I_p(t_n, A_p, k_p, \mu_n, \sigma_n) = \frac{A_p}{2}\exp\left[\frac{k_p}{2}(2\mu_n + k_p{\sigma_n}^2)\right]\mathrm{erfc}\left(\frac{\mu_n + k_p{\sigma_n}^2 - t_n}{\sqrt{2}\sigma_n}\right)\exp(-k_p t_n) \tag{2.17}$$

$$I_d(t_n, A_{\mathrm{d}}, k_d, \mu_n, \sigma_n) = \frac{A_d}{2}\exp\left[\frac{k_d}{2}(2\mu_n + k_d{\sigma_n}^2)\right]\mathrm{erfc}\left(\frac{\mu_n + k_d{\sigma_n}^2 - t_n}{\sqrt{2}\sigma_n}\right)\exp(-k_d t_n) \tag{2.18}$$

where t_1, t_2, and t_3 are t, $t - \mu_2 + \mu_1$, and $t - \mu_3 + \mu_1$, respectively. The corresponding deconvoluted exponential curve can be written by Eq. 2.19.

$$I_{dec}(t) = (R_1 + R_2 + R_3)\left[A_p \exp(-k_p t) + A_d \exp(-k_d t)\right], \qquad (t \geq 0) \tag{2.19}$$

In this study, the PL decay curves were analyzed by using three ex-Gauss curves for bi-exponential decay with a baseline ($I(t) + baseline$).

Estimation of experimental reorganization energy (λ) and SOCME

Basically, the ISC and RISC process can be explained as an electron transfer reaction between S_1 and T_1 orbitals therefore, those are often explained by using the basic equation of Marcus theory with the equation of Eqs. 2.20-2.21.[21]

$$k_{ET} = \frac{2\pi}{\hbar}|H_{\mathrm{if}}|^2 \frac{1}{\sqrt{4\pi\lambda k_B T}} \exp\left[-\frac{\Delta G^{\ddagger}}{k_B T}\right] \tag{2.20}$$

$$\Delta G^{\ddagger} = \frac{(\lambda + \Delta G^{\mathrm{o}})^2}{4\lambda} \tag{2.21}$$

where k_{ET} is an electron transfer rate, $\hbar$ is the Dirac's constant, H_{if} is an electronic coupling between the initial and final states, $\Delta G^{\ddagger}$ is the transition state energy, λ is the reorganization energy, k_B is the Boltzmann constant, T is the temperature, and ΔG^{o} is the total Gibbs free energy change between the initial and final states for the electron transfer reaction. To apply RISC process, the equation can be written as Eq. 2.22; the equation was shown only for RISC process in here.[16]

$$k_{\mathrm{RISC}} = \frac{2\pi}{\hbar\sqrt{4\pi\lambda k_B T}} \left|\langle \psi_{\mathrm{S}} | \hat{H}_{\mathrm{SOC}} | \psi_{\mathrm{T}} \rangle\right|^2 \exp\left(-\frac{E_a^{RISC}}{k_B T}\right) \tag{2.22}$$

Until now, the SOCME strength has only been given by quantum chemical calculations, but I present a method for experimentally estimating the effective SOC strength under the application of the Marcus equation. The activation energy of the ISC and RISC processes can be calculated using the temperature dependence of the rate constants in an Arrhenius plot ($\ln k = -E_a/k_BT + \ln A$) from the slope but notice in Eq. 2.22 that the intercept term ($\ln A$) in the Arrhenius formula includes a temperature term ($\sqrt{T}$). This means that each plot in the Arrhenius plot is drifting. It can be written for the Arrhenius plot ($\ln k$ vs. $1/T$) as Eq. 2.23.[22]

$$\ln k_{\mathrm{RISC}} = -\frac{E_a^{RISC}}{k_B}\frac{1}{T} + \ln\left(\frac{2\pi}{\hbar\sqrt{4\pi\lambda k_B T}} \left|\langle \psi_{\mathrm{S}} | \hat{H}_{\mathrm{SOC}} | \psi_{\mathrm{T}} \rangle\right|^2\right) \tag{2.23}$$

In this case, there is a time dependence term in the intercept coefficient. While the phenomena related to TADF are provided in very small energy regions, this would have a large impact. Therefore, the Marcus plot with Eq. 2.23 should be used to discuss its temperature dependency.

$$\ln\left(\sqrt{T} k_{\mathrm{RISC}}\right) = \alpha \cdot \frac{1}{T} + \ln\beta = -\frac{E_a^{RISC}}{k_B} \cdot \frac{1}{T} + \ln\left(\frac{2\pi}{\hbar\sqrt{4\pi\lambda k_B}} \left|\langle \psi_{\mathrm{S}} | \hat{H}_{\mathrm{SOC}} | \psi_{\mathrm{T}} \rangle\right|^2\right) \tag{2.24}$$

From the slope coefficient α of the straight-line approximation in the Marcus plot, E_a^{RISC} can be explained as $-\alpha k_B$. From the intercept coefficient ln β of the collinear approximation line in the Marcus plot, The absolute value of SOCME can be obtained as Eq. 2.25.

$$\left|\langle\psi_{\mathrm{S}}|\hat{H}_{\mathrm{SOC}}|\psi_{\mathrm{T}}\rangle\right| = \sqrt{\frac{\hbar}{2\pi}\sqrt{4\pi\lambda k_B}\exp(\ln\beta)} \tag{2.25}$$

Because $\Delta G^{\ddagger}$ and ΔG^{o} are corresponding to be activation energy (E_a^{RISC}) and energy difference between S_1 and T_1 (ΔE_{ST}), λ can be written as Eq. 2.26. Note that ΔE_{ST} is a value defined by $E_a^{RISC} - E_a^{ISC}$ and λ should be smaller or larger than ΔE_{ST} in Marcus' normal or reverse region.

$$\lambda = E_a^{ISC} + E_a^{RISC} \pm 2\sqrt{E_a^{ISC} \cdot E_a^{RISC}} \tag{2.26}$$

Note that the value of ΔE_{ST} should be negative by using E_a^{ISC} instead of E_a^{RISC}. The value of λ should be the same between ISC and RISC processes. Considering a Marcus Parabola, $\lambda > \Delta E_{\mathrm{ST}}$ when the system is in the Marcus normal region and $\lambda < \Delta E_{\mathrm{ST}}$ when the system is in the Marcus inverted region. Therefore, TADF materials with small ΔE_{ST} are considered to be in the Marcus normal region. Note that although the ΔE_{ST} calculated by the Arrhenius and Marcus plots are the same, E_a^{ISC} and E_a^{RISC} can difference by several 10 meV, so for TADF materials where small E_{a} is often discussed Marcus plots are preferred.

Derivation of internal quantum efficiency (η_{int})

Because the excitons are statistically generated as singlet and triplet with the ratio of 1:3, the prompt emission fraction in current excitation is $0.25\Phi_{PF}$. When the number of cycles for ISC/RISC (n) equals 1, the additional emissive fraction is $0.25\Phi_{PF}\Phi_{ISC}\Phi_{RISC} + 0.75\Phi_{PF}\Phi_{RISC}$. When n = 2 and 3, the additional emissive fraction is $0.25\Phi_{PF}(\Phi_{ISC}\Phi_{RISC})^2 + 0.75\Phi_{PF}\Phi_{ISC}\Phi_{RISC}{}^2$ and $0.25\Phi_{PF}(\Phi_{ISC}\Phi_{RISC})^3 + 0.75\Phi_{PF}\Phi_{ISC}{}^2\Phi_{RISC}{}^3$, respectively. Therefore, the total emission efficiency considering PF and DF at the current excitation (internal quantum efficiency, η_{int}) can be formulated as Eq. 2.27 under the assumption of no phosphorescence in emission.

$$\begin{aligned}\eta_{int} &= \frac{1}{4}\Phi_{PF}\sum_{n=0}^{\infty}(\Phi_{ISC}\Phi_{RISC})^n + \frac{3}{4}\Phi_{PF}\sum_{n=1}^{\infty}\Phi_{ISC}{}^{n-1}\Phi_{RISC}{}^n \\ &= \frac{1}{4}\Phi_{PF} + \frac{(\Phi_{ISC}+3)}{4\Phi_{ISC}}\Phi_{PF}\sum_{n=1}^{\infty}(\Phi_{ISC}\Phi_{RISC})^n\end{aligned} \tag{2.27}$$

On the other hand, the PLQY (Φ_{PLQY}) can be written by,

$$\Phi_{PLQY} = \Phi_{PF}\sum_{n=0}^{\infty}(\Phi_{ISC}\Phi_{RISC})^n = \Phi_{PF} + \Phi_{PF}\sum_{n=1}^{\infty}(\Phi_{ISC}\Phi_{RISC})^n \quad (2.28)$$

From Eq. 2.28, the fragment of delayed fluorescence can be written by,

$$\Phi_{DF} = \Phi_{PLQY} - \Phi_{PF} = \Phi_{PF}\sum_{n=1}^{\infty}(\Phi_{ISC}\Phi_{RISC})^n \quad (2.29)$$

From Eqs. 2.27 and 2.29, η_{int} can be written as

$$\eta_{int} = \frac{1}{4}\Phi_{PF} + \frac{(\Phi_{ISC}+3)}{4\Phi_{ISC}}\Phi_{DF} = \frac{1}{4}\left(\Phi_{PLQY} + 3\frac{\Phi_{DF}}{\Phi_{ISC}}\right) \quad (2.30)$$

Also, $\eta_{int} = \Phi_{PLQY}(1 + 3\Phi_{RISC})/4$ can be obtained by a similar method. When the limit condition of $k_{nr}^{T} = 0$ was employed, Φ_{DF}/Φ_{ISC} should be Φ_{PLQY} because Φ_{DF} is the emitting fraction via S_1 of generated T_1 exciton by ISC process. Therefore, η_{int} is provided as the same value with Φ_{PLQY}. However, η_{int} is provided much smaller than Φ_{PLQY} in the limit condition of $k_{nr}^{S} = 0$. In the case of 1 wt% BN4 in DPEPO, η_{int} was estimated to be 0.801 (= Φ_{PLQY}) and 0.459 for $k_{nr}^{T} = 0$ and $k_{nr}^{S} = 0$, respectively.

2. 5. References

[1] Hatakeyama, T.; Shiren, K.; Nakajima, K.; Nomura, S.; Nakatsuka, S.; Kinoshita, K.; Ni, J.; Ono, Y.; Ikuta, T. Ultrapure Blue Thermally Activated Delayed Fluorescence Molecules: Efficient HOMO-LUMO Separation by the Multiple Resonance Effect. *Adv. Mater.* **2016**, *28*, 2777–2781.

[2] Chan, C.-Y.; Suresh, S. M.; Lee, Y.-T.; Tsuchiya, Y.; Matulatis, T.; Hall, D.; Slawin, A. M. Z.; Warriner, S.; Beljonne, D.; Olivier, Y.; Adachi, C.; Zysman-Colman E. Two boron atoms versus one: high-performance deep-blue multi-resonance thermally activated delayed fluorescence emitters. *Chem. Commun.* **2022**, *58*, 9377.

[3] Park, J.; Lim, J.; Jang, B.; Han, J. H.; Yoon, S. S.; Lee, J. Y. Asymmetric Blue Multiresonance TADF Emitters with a Narrow Emission Band. *ACS Appl. Mater. Interfaces* **2021**, *13*, 45798−45805.

[4] Ando, M.; Sakai, M.; Ando, N.; Hirai, M.; Yamaguchi, S. Planarized *B*, *N*-phenylated dibenzoazaborine with a carbazole substructure: Electronic impact of the structural constraint. *Org. Biomol. Chem.* **2019**, *17*, 5500–5504.

[5] Kim, H. J.; Yasuda, T. Narrowband Emissive Thermally Activated Delayed Fluorescence Materials. *Adv. Opt. Mater.* **2022**, *10*, 2201714.

[6] Mamada, M.; Hayakawa, M.; Ochi, J.; Hatakeyama, T. Organoboron-Based Multiple-Resonance Emitters: Synthesis, Structure-Property Correlations, and Prospects. *Chem. Soc. Rev.* **2024**, *53*, 1624.

[7] Pershin, A.; Hall, D.; Lemaur, V.; Sancho-Garcia, J. C.; Muccioli, L.; Zysman-Colman, E.; Beljonne, D.; Olivier, Y. Highly Emissive Excitons with Reduced Exchange Energy in Thermally Activated Delayed Fluorescent Molecules. *Nat. Commun.* **2019**, *10*, 597.

[8] Stephen, P. J.; Devlin, F. J.; Chabalowski, C. F.; Frisch, M. J. Ab Initio Calculation of Vibrational Absorption. *J. Phys. Chem.* **1994**, *98*, 11623–11627.

[9] Neese, F., Wennmohs, F., Becker, U. and Riplinger, C. The ORCA Quantum Chemistry Program Package. *J. Chem. Phys.* **2020,** *152*, 224108.

[10] Bhattacharyya, K. Can TDDFT Render the Electronic Excited States Ordering of Azine Derivative? A Closer Investigation with DLPNO-STEOM-CCSD. *Chem. Phys. Lett.* **2021**, *779*, 138827.

[11] Hirata, S.; Sakai, Y.; Masui, K.; Tanaka, H.; Lee, S. Y.; Nomura, H.; Nakamura, N.; Yasumatsu, M.; Nakanotani, H.; Zhang, Q.; Shizu, K.; Miyazaki, H.; Adachi, C. Highly efficient blue electroluminescence based on thermally activated delayed fluorescence. *Nat. Mater.* **2015**, *14*, 330–336.

[12] Tsuchiya, Y.; Tsuji, K.; Inada, K.; Bencheikh, F.; Geng, Y.; Kwak, H. S.; Mustard, T. J. L.; Halls, M. D.; Nakanotani, H.; Adachi, C. Molecular Design Based on Donor-Weak Donor Scaffold for Blue Thermally Activated Delayed Fluorescence Designed by Combinatorial DFT Calculations. *Front. Chem.* **2020**, *8*, 2–11.

[13] Tsuchiya, Y.; Ishikawa, Y.; Lee, S. H.; Chen, X. K.; Brédas, J. L.; Nakanotani, H.; Adachi, C. Thermally Activated Delayed Fluorescence Properties of Trioxoazatriangulene Derivatives Modified with Electron Donating Groups. *Adv. Opt. Mater.* **2021**, *9*, 1–8.

[14] Reichardt, C. Solvatochromic dyes as solvent polarity indicators. *Chem. Rev.* **1994**, *94*, 2319–2358.

[15] Tsuchiya, Y.; Diesing, S.; Bencheikh, F.; Wada, Y.; dos Santos, P. L.; Kaji, H.; Zysman-Colman, E.; Samuel, I. D. W.; Adachi, C. Exact Solution of Kinetic Analysis for Thermally Activated Delayed Fluorescence Materials. *J. Phys. Chem. A* **2021**, *125*, 8074–8089.

[16] Samanta, P. K.; Kim, D.; Coropceanu, V.; Brédas, J. L. Up-Conversion Intersystem Crossing Rates in Organic Emitters for Thermally Activated Delayed Fluorescence: Impact of the Nature of Singlet vs Triplet Excited States. *J. Am. Chem. Soc.* **2017**, 139, 4042–4051.

[17] Masui, K.; Nakanotani, H.; Adachi, C. Analysis of exciton annihilation in high-efficiency sky-blue organic light-emitting diodes with thermally activated delayed fluorescence. *Org. Electron.* **2013**, *14*, 2721−2726.

[18] Dias, F. B.; Penfold, T. J.; Monkman, A. P. Photophysics of thermally activated delayed fluorescence molecules. *Methods Appl. Fluoresc.* **2017**, 5, 012001.

[19] Endo, A.; Sato, K.; Yoshimura, K.; Kai, T.; Kawada, A.; Miyazaki, H.; Adachi, C. Efficient up-conversion of triplet excitons into a singlet state and its application for organic light emitting diodes. *Appl. Phys. Lett.* **2011**, *98*, 083302.

[20] Hirata, S.; Sakai, Y.; Masui, K.; Tanaka, H.; Lee, S. Y.; Nomura, H.; Nakamura, N.; Yasumatsu, M.; Nakanotani, H.; Zhang, Q.; Shizu, K.; Miyazaki, H.; Adachi, C. Highly efficient blue electroluminescence based on thermally activated delayed fluorescence. *Nat. Mater.* **2015**, *14*, 330–336.

[21] Marcus, R. A. Electron Transfer Reactions in Chemistry: Theory and Experiment. *Rev. Mod. Phys.* **1993**, 65, 599−610.

[22] Fukuzumi, S.; Itoh, A.; Ohkubo, K.; Suenobu, T. Size-selective incorporation of donor–acceptor linked dyad cations into zeolite Y and long-lived charge separation. *RSC Adv.* **2015**, *5*, 45582−45585.

Chapter III

Experimental Investigation and Visualization of the Electronic Structure of a Single MR-TADF Molecule Using Scanning Tunneling Microscopy

3. 1. Introduction

As discussed in ***Chapter I***, STM stands as the most powerful method for probing the electronic structures of single TADF molecules at the atomic level.[1-5] STM utilizes a topographical scanning technique across a two-dimensional plane, where a bias voltage (V_s) is applied between the STM tip and the sample. The technology exploits quantum tunneling, a phenomenon in which electrons go through a vacuum gap between a tip and a surface, enabling atomic-scale analysis of materials.

During STM operation, a conductive tip scans the surface, and the resulting tunneling current, which varies with the spatial distribution of the LDOS of the sample, is measured.[3,5] This current is sensitive to the electronic properties at specific locations on the sample, allowing for detailed imaging and spectroscopic analysis. STM's ability to adjust the bias voltage facilitates the investigation of conductance, thereby enabling the spectroscopic imaging of MOs at defined energy levels. This capability is crucial for the precise visualization of the electronic structure at the atomic level, providing deep insights into the behavior and properties of single TADF molecules.

Although STM has successfully visualized the HOMO and LUMO in conventional donor-acceptor (D-A) type TADF molecules,[6-8] the visualization of FMOs in MR-TADF molecules presents significant challenges due to the delicate separation between HOMO and LUMO that occurs at the atomic scale, necessitating an even higher spatial resolution than typically required for D-A type TADF molecules. To enhance the spatial resolution of STM for analyzing the intricate electron structures in MR-TADF molecules, I have remarkable tip functionalization techniques by customizing STM tips equipped with a chlorine (Cl) atom at the apex.[9-10] This tailor-made setup achieves higher spatial resolution compared to conventional bare metal tips, which is crucial for accurately visualizing FMOs and their separations within MR-TADF molecules.

Synthesis of DABNA-1, 5,9-diphenyl-5,9-diaza-13b-bora-5*H*,9*H*-naphtho[3,2,1-*de*]anthracene, was aimed at investigating the electronic structure of MR-TADF molecules using advanced STM techniques. Although the molecule series of BNs used in ***Chapter I*** were also good candidates for STM measurements, the asymmetric single phenyl groups present in BN2 and BN3 had the potential to rearrange parallel to the chromophore core upon adsorption onto the surface, significantly altering the electronic structure of the molecule. The methyl groups present in BN2 and BN4 also had the potential to form protruding images in STM scans, hindering visualization of the electronic structure. Therefore, I decided to use the more representative DABNA-1 for STM analysis. By depositing a single DABNA-1 molecule onto an ultrathin NaCl insulating film, I isolated its electronic structure from the metallic influences of the Au(111) substrate. The Cl-terminated STM tip provided enhanced spatial resolution, allowing us to scan STM images with sufficient clarity to distinguish the FMOs at each carbon atom corresponding to the resonance effects induced by the heteroatoms within the DABNA-1 molecule.[9-10]

These images revealed resonance effects induced by heteroatoms within the DABNA-1 molecule, challenging previous theoretical assumptions that such substituted heteroatoms would result in equivalent orbital lobes at the *ortho*- and *para*-positions.[11-13] Furthermore, local DOS analysis through scanning tunneling spectroscopy (STS) revealed the presence of empty states, which can be regarded as LUMO, in regions around nitrogen atoms. These experimental findings highlight the need for additional considerations in molecular design to precisely control the separation between HOMO and LUMO in MR-TADF molecules

3. 2. Result and discussion

3. 2. 1 DABNA-1 deposition onto 1-ML NaCl/Au(111)

The formation of FMOs by resonance effects in the DABNA-1 molecule is prominently influenced by the positions of the nitrogen and boron atoms, which act as electron donors and acceptors, respectively. These elements are strategically embedded within the polycyclic aromatic hydrocarbon (PAH) core, contributing significantly to the formation of the HOMO and LUMO at ortho and para positions relative to adjacent benzene rings. **Figure 3-1** depict these configurations. The ortho positioning of these atoms limits the overlap of resonance effects, enhancing the TADF properties of the molecule. In general, the presence of two peripheral phenyl groups (PPGs) attached to the nitrogen atom does not contribute to the electronic properties of the PAH core. Instead, these PPGs introduce steric hindrance between molecules, which prevents the molecules from concentration quenching.[14-16]

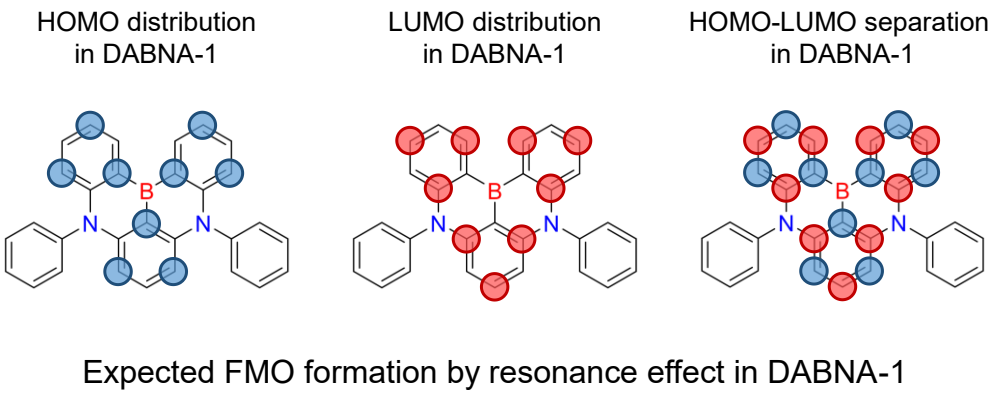

Figure 3-1. Illustration of FMOs formation by resonance effect corresponding to heteroatoms in the molecular structure of DABNA-1.

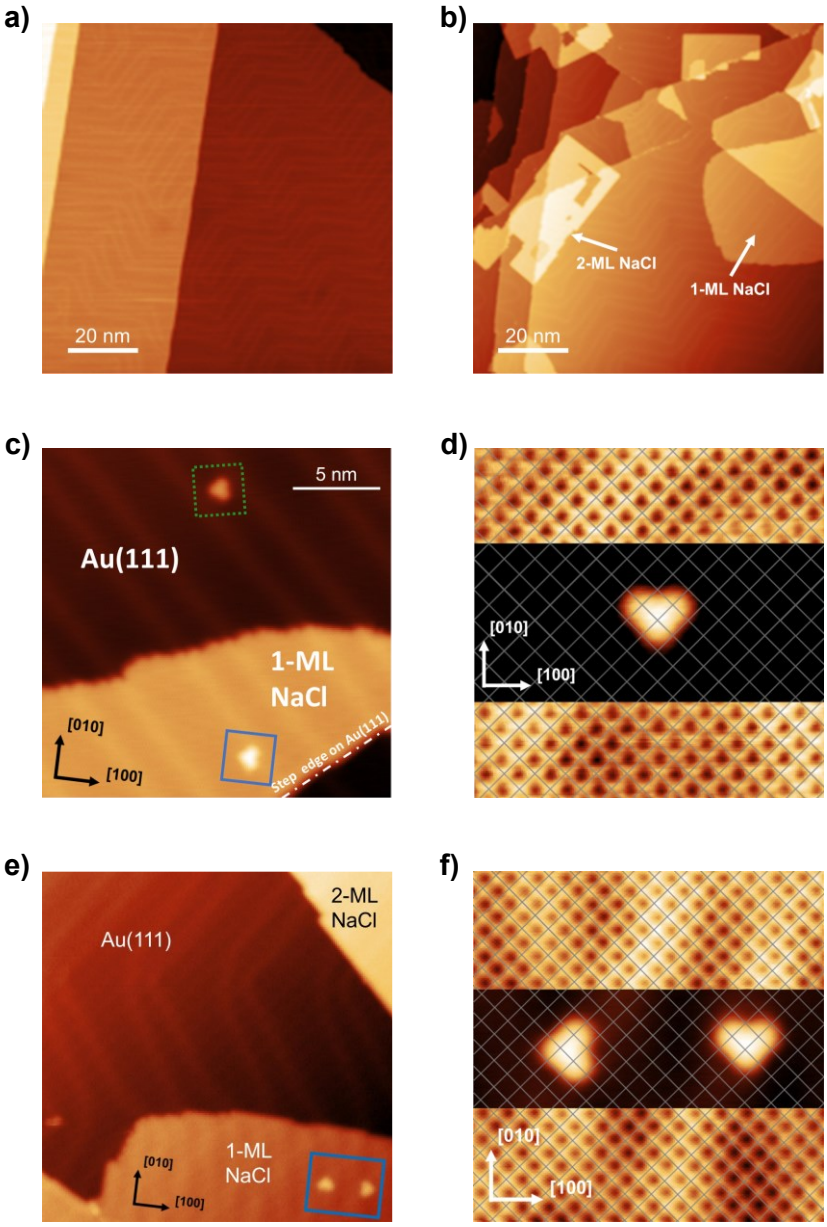

Figure 3-2. a) STM images of cleaned Au(111) surface and **b)** after NaCl films growing (I_t = +3 pA, V_s: +1.0 V, scan size: 100 nm × 100 nm). 1-ML and 2-ML NaCl films were predominantly observed on the step-edge side of the Au(111) surface. **c)** STM overview images of DABNA-1 molecule on Au(111) and 1-ML NaCl/Au(111) surface (Scan size = 20 nm × 20 nm, I_t = +10 pA, V_s = +1.0 V). **d)** Adsorption structure STM image of in-gap state DABNA-1 molecule on 1-ML NaCl/Au(111) (Cl-terminated tip is used, scan size: 6 nm × 6 nm, surface: I_t = +2.2 nA, V_s = +20 mV; molecule: I_t = +10 pA, V_s = +1.0 V). **e)** Adjacent two equivalent DABNA-1 molecules adsorbed with two different orientations on 1-ML NaCl/Au(111) surface (I_t = +10 pA, V_s = +1.0 V, scan size = 30 nm × 30 nm). **f)** STM image of DABNA-1 molecule with atomically resolved 1-ML NaCl/Au(111) surface (Cl-terminated tip, scan size : 7 nm × 7 nm, surface : I_t = +2.2 nA, V_s : +20 mV ; molecule : I_t = +10 pA, V_s : +1.0 V).

To investigate these unique MR-TADF characteristics, I prepared a clean Au(111) substrate followed by the growth of 1- or 2-monolayer (ML) NaCl islands as illustrated in **Figures 3-2a** and **3-2b**.

Subsequently, DABNA-1 molecules were deposited onto these substrates maintained at temperatures below 14 K. STM scanning of DABNA-1 molecules on both the bare Au(111) and 1-ML NaCl/Au(111) surfaces was conducted in a cryogenic, ultra-high vacuum environment at approximately 4.6 K and a pressure of about 5.8×10^{-11} torr.

Figure 3-2c shows an STM image of two heart-shaped single DABNA-1 molecules, reflecting the PAH core of the molecules on both substrate types, the Au(111) surface highlighted with a green dashed line and the 1-ML NaCl/Au(111) surface with a blue line. The atomically-resolved STM image in **Figure 3-2d** reveals the adsorption site of the DABNA-1 molecule on the NaCl film surface. The adsorption structures of DABNA-1 observed at the [010] or [100] orientation on the NaCl surface in **Figures 3-2e** and **3-2f** further demonstrate the orientation of the molecule relative to the substrate.

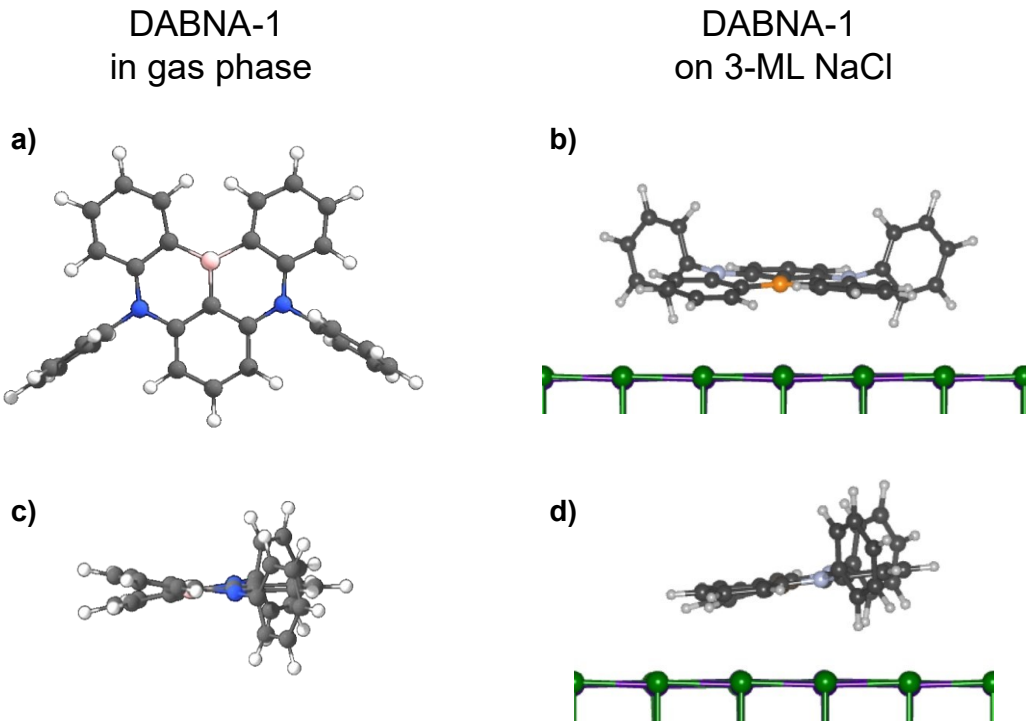

Figure 3-3. The optimized ground geometry for DABNA-1 views from **a)** the front and **b)** the side using DFT at B3LYP/def2-SVP (C, H, N, and B were colored dark gray, white, blue, and light orange, respectively). Optimized geometry of DABNA-1 molecule on 3-ML NaCl layers views from **c)** the top and **d)** the side (Na, Cl, C, H, N, and B were colored purple, green, dark gray, light gray, light blue, and orange, respectively).

For a comprehensive understanding of the geometric and electronic structure of the molecule, I performed computational simulations using the B3LYP method for gas phase optimization and the DFT-D3 method with van der Waals (vdW)-dispersion corrections to model the adsorption configuration and electronic structure (**Figure 3-3**).[17-18] Intriguingly, the DFT results confirmed that the PAH core of the DABNA-1 molecule adopts a nearly planar structure with a torsional angle of about 5° when adsorbed

on the 3-ML NaCl surface, a notable reduction from the 20° observed in gas-phase calculations, depicted in **Figures 3-3b** and **3-3d**. This planarity is slightly adjusted due to the tilt of the PAH framework relative to the NaCl surface, with the PPGs oriented perpendicularly. This geometrical configuration might explain why the PPGs were not identified in the in-gap state image of the STM results, possibly due to their perpendicular orientation to the STM tip and an insufficient DOS at the relevant energy levels to be detected.

3. 2. 2. STS measurement and local density of state analysis

To enhance my understanding of the MOs distribution within the DABNA-1 molecule, I employed spatial distribution spectroscopy facilitated by STM. This approach involved measuring differential conductance (d*I*/d*V*) spectra using scanning tunneling spectroscopy (STS) to resolve the electronic structure of the DABNA-1 molecule deposited on a 1-monolayer (ML) NaCl/Au(111) substrate. This technique allowed for the precise identification of the LDOS, which varies depending on the position of the STM tip relative to the DABNA-1 molecule.[5,7] To avoid interference from the electronic states of a terminated Cl atom on the tip's conductivity, measurements were conducted using a bare Au tip.

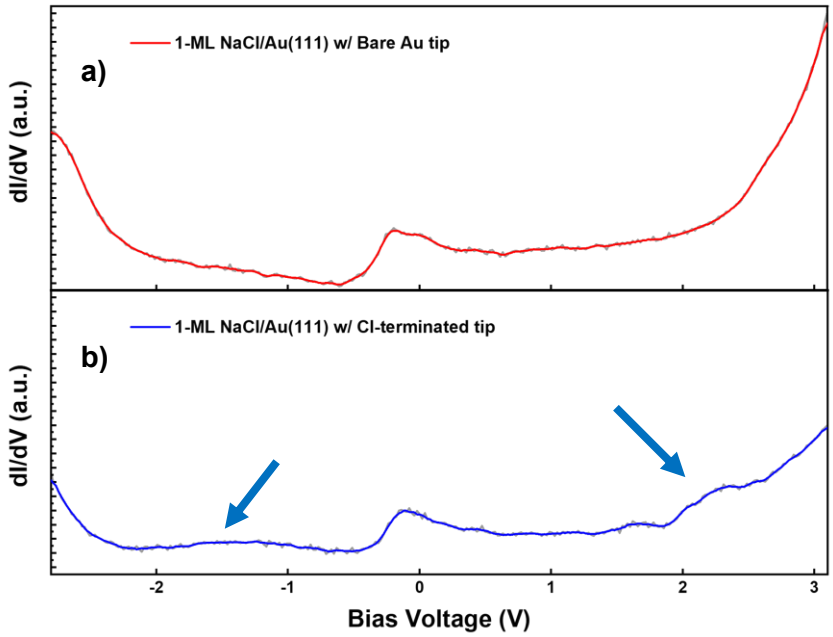

Figure 3-4. d*I*/d*V* spectra of surface state on 1-ML NaCl/Au(111) surface with **a)** Au tip and **b)** Cl-terminated tip. In the case of d*I*/d*V* spectra measured with a Cl-terminated tip, the electronic structure is observed to be impacted by the Cl atom at the tip apex.

As shown in **Figure 3-4**, when measuring the surface state of the 1-ML NaCl/Au(111) surface in the case of the Cl-terminated tip, I observed additional peaks near -1.5 V and +2.2 V compared to the bare Au tip. The appearance of this additional state is considered to be an effect of the DOS of Cl attached to the tip, and while it is not critical to the MOs observations and STS measurements performed in this experiment, it can be difficult to use the results reported in the paper to obtain the ionization energy and electron affinity of a single molecule, so a bare metal tip was used in this experiment.

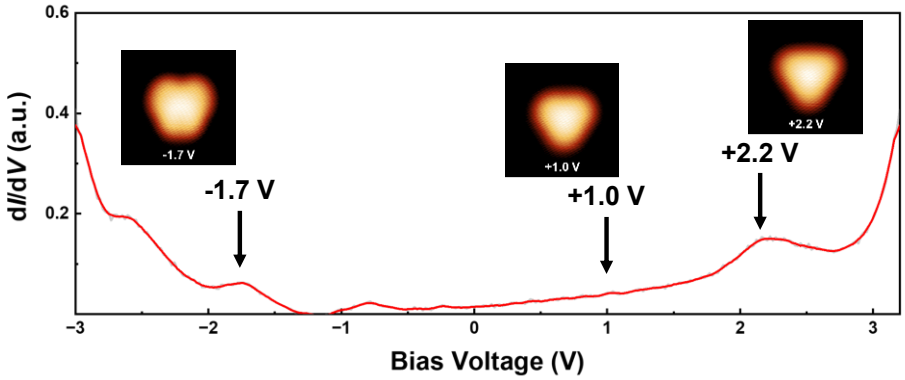

Figure 3-5. STM images in C.C. mode and dI/dV spectrum of DABNA-1 molecule on Au(111) surface (Bare Au tip, I_t = +10.0 pA, scan size = 2.5 nm × 2.5 nm). Compared to the results in the DABNA-1 molecule on 1-ML NaCl/Au(111), the position of the peaks in the dI/dV spectrum is largely shifted (from -2.4 V to -1.7 V and +2.7 V to +2.2 V, respectively).

Before I studied DABNA-1 molecules using STS, I confirmed that profound differences in electronic structure between the molecule on a metallic surface, Au(111), and an ultrathin insulating film, 1-ML NaCl/Au(111) substrate (**Figures 3-5** and **3-6a**). When DABNA-1 is adsorbed directly onto the Au(111) surface, the molecule's orbitals strongly interact with the electronic states of the metal surface. This interaction leads to the hybridization of the metallic state with MO, resulting in a mixed characterization of the metallic surface in the spectra observed in STS measurements. In contrast, on the 1-ML NaCl/Au(111) substrate, the insulating 1-ML NaCl layer acts as a decoupling factor, reducing the influence of the surface state of Au(111) on the electronic structure of DABNA-1. This decoupling preserves the intrinsic electronic structure of the organic molecule, allowing the contours of the MO distribution in organic molecules to be more accurately observed by STM scans. The peaks within the STS spectrum of the DABNA-1 molecule on 1-ML NaCl/Au(111) also offer a more accurate depiction of the molecule's inherent electronic states. It is noteworthy that when comparing the two STS spectra, there was a shift in the spectral peaks indicating the energy level of specific electronic states. For DABNA-1 on Au(111), the peaks in the STS spectrum had appeared closer to the Fermi level due to the aforementioned orbital hybridization. In contrast, for DABNA-1 on 1-ML NaCl/Au(111) substrate, the same peaks are observed at higher energy for the LUMO and lower energy for the HOMO. Additionally,

for DABNA-1 on 1-ML NaCl/Au(111), the STS spectrum showed almost no d*I*/d*V* intensity between the peaks of the two resonant channels presumed to be the HOMO and LUMO. These properties are similar to those of electronic band structures of semiconductor materials and confirm that the inherent electronic structures of DABNA-1 are better preserved on 1-ML NaCl/Au(111).

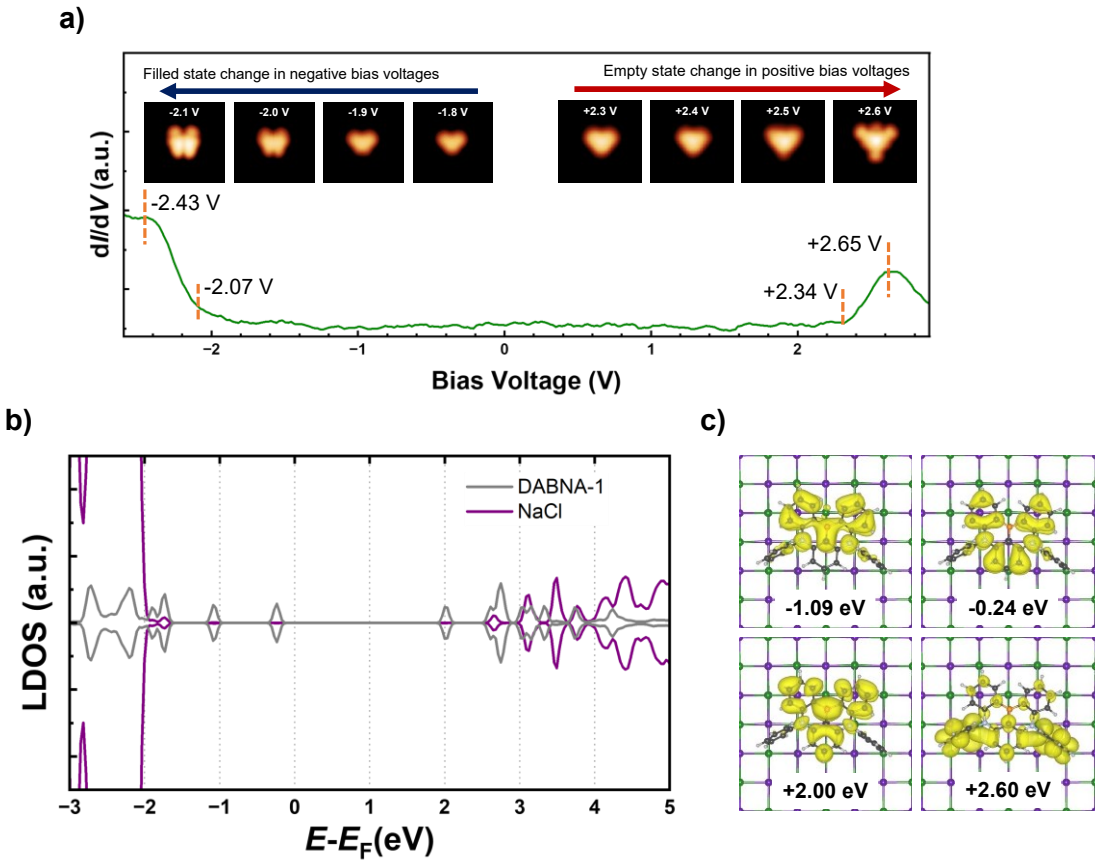

Figure 3-6. a) The d*I*/d*V* spectrum of the DABNA-1 molecule on 1-ML NaCl/Au(111) with peak top values and onset values (inset: I_t = 3 pA, Scan size = 3 nm × 3 nm). **b)** Local DOS (LDOS) for a DABNA-1 molecule on 3-ML NaCl and **c)** band-decomposed charge density map at different energy (Na, Cl, C, B, N, and H were colored as purple, green, dark gray, orange, silver and light gray, respectively).

To confirm whether the electronic states observed in the STM image correspond to the HOMO and LUMO of the DABNA-1 molecule, I performed additional calculations on the LDOS using the DABNA-1 molecule situated on a 3-ML NaCl slab model. The results, presented in **Figures 3-6b** and **3-6c**, include the calculated LDOS and band-decomposed charge density maps at various energy levels. The LDOS calculations revealed that the energy states of the first and second electronic states in both the occupied and unoccupied regions are notably distinct, with no energetic degeneracy observed between them. This was evidenced by the clear separation and unique spatial distributions in their electronic structures. If these states have been energetically degenerate, their features would have merged in the STM images, appearing as an integrated image. Consequently, the electronic states

observed in the STM images in the d*I*/d*V* spectrum can be considered to be the peaks at -0.24 eV and +2.00 eV in calculated LDOS.

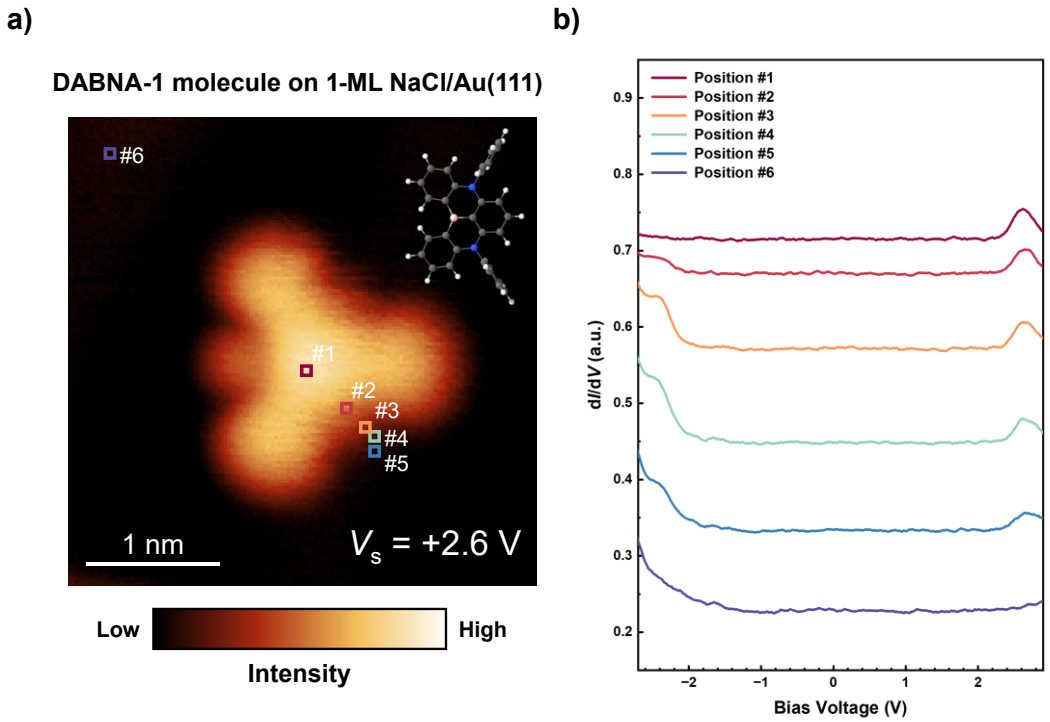

Figure 3-7. Electronic structures of DABNA-1 molecule on 1-ML NaCl/Au(111) and spatial distributions of electronic state. **a)** Constant current mode STM scan image of the DABNA-1 molecule at +2.6 V (Au tip, scan size = 3.5 nm × 3.5 nm, I_t = +3.0 pA). **b)** Moving averaged d*I*/d*V* spectra measured at six different tip positions.

After confirming that the 1-ML NaCl interface could clearly resolve the MOs of the DABNA-1 molecule, I analyzed the STS spectrum of the DABNA-1 molecule on 1-ML NaCl/Au(111). Considering that in the in-gap state, it is difficult to determine the exact location of boron and nitrogen atoms within the DABNA-1 molecule, which are important for electron donation and acceptance ability, I positioned the tip based on STM images taken at a bias voltage (V_s) of +2.6V. This setpoint enhances the visibility of the electronic state distribution corresponding to heteroatoms, as shown in **Figure 3-7a**. The resulting d*I*/d*V* spectra, based on the tip's positions across the molecule, are detailed in **Figure 3-7b**. For clarity, each corresponding tip positions were annotated in the STM image sequentially from #1 to #6, with position #6 serving to measure the surface state of the 1-ML NaCl/Au(111) away from the molecule.

The initial focus was on the central region of the STM image obtained at V_s of +2.6 V, where the LUMO primarily formed by the boron atom was expected to be prominent. By locating the tip at position #1, I captured a resonant tunneling peak at around +2.6 V, indicative of an empty state associated with

a single DABNA-1 molecule. This peak was distinctly separated from both the surface state and the conductivity contributions of the 1-ML NaCl/Au(111) substrate (noted at position #6). Notably, the absence of signals for the filled state at negative V_s suggests that the LUMO is predominantly localized in the central region of the DABNA-1 molecule. Further STS analysis involved relocating the tip to positions #2 and #3, aimed at the presumed locations of the nitrogen atoms. The dI/dV spectra from these positions revealed a peak at approximately -2.3 V, corresponding to the filled state of the molecule, indicative of the presence of a HOMO localized around the nitrogen atoms. This finding is corroborated by the electronic state distribution observed in the STM images and the distinct peaks in the dI/dV spectra at position #3, suggesting a significant presence of the LUMO distribution. As the tip moved to positions #4 and #5, the dI/dV spectrum continued to show two distinct resonance channels at both bias voltages of +2.6 V and -2.3 V. While quantitative analysis of MO distribution from dI/dV conductivity spectra remains challenging, these results strongly imply substantial involvement of nitrogen atoms and adjacent peripheral phenyl groups (PPGs) in the overlap between HOMO and LUMO within the DABNA-1 molecules.

3. 2. 3. Energy level alignment of the DABNA-1 molecule

Upon meticulous examination of the DABNA-1 molecule situated on a 1-monolayer (ML) NaCl/Au(111) substrate, I conducted a detailed assessment of the ionization potential and electron affinity by means of the well-established techniques outlined in **Figure 3-8**. The STS measurements, indicative of the resonant tunneling peaks, reveal insights into the energy levels of the molecule's HOMO and LUMO. However, to achieve an accurate representation of these energy levels, I must consider the voltage drop across the insulating NaCl film, a factor that demands careful calibration.[19] The compensation method for this voltage drop is described in detail in **3. 4. Experimental section** and estimated using the onset values of the two negative and positive peaks on the STS spectrum in **Figure 3-6**.[19-20]

The process involves factoring in the work function (Φ_s) of the 1-ML NaCl/Au(111), along with the estimated ionization (E_i^F) and electron affinity (E_a^F) energies referenced to the Fermi level (E^F). With these considerations of Φ_s, the ionization (E_i^v) and electron affinity (E_a^v) energies were adjusted to align with the vacuum level (E_v), resulting in a more accurate representation of the electronic structure of the molecule. Using this compensation, I deduced an energy gap of approximately 3.82 eV for a single DABNA-1 molecule on the 1-ML NaCl/Au(111) surface. This calculation stands in contrast to the apparent HOMO-LUMO gap, which was initially measured to be 4.41 eV from the raw dI/dV data. The importance of this compensated approach was demonstrated by the large discrepancy between the compensated and apparent energy gaps, especially for materials with a wide range of band gaps. This

emphasizes the importance of considering Fermi level alignment and voltage drop from the insulating film for a quantitative understanding of the electronic structure.

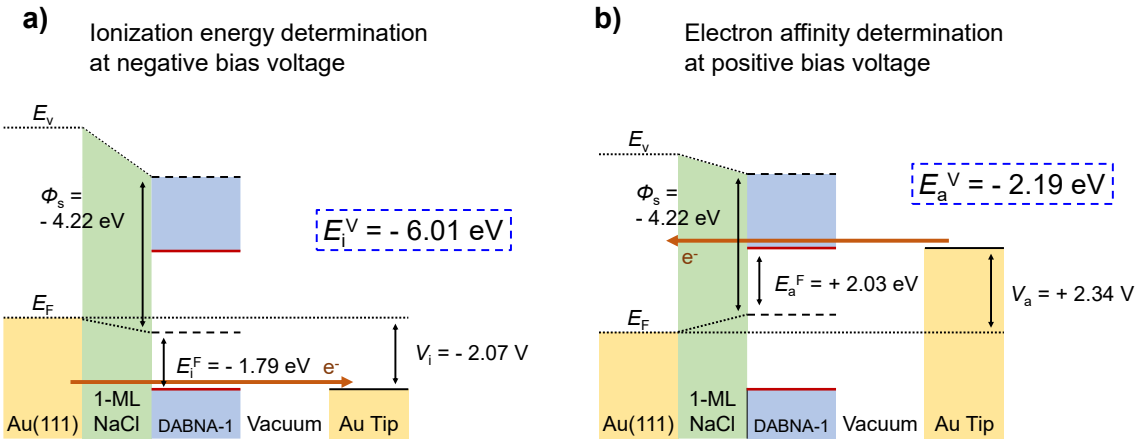

Figure 3-8. Schematic illustration of the energy diagrams compensated voltage drop in the NaCl film. **a)** Ionization energy and **b)** electron affinity of DABNA-1 molecule on 1-ML NaCl/Au(111) estimated from the onset value of each peak with the reported method.

I compared the estimated ionization and electron affinity values obtained from the STS spectrum with the data measured from the CV results of DABNA-1.[1] The ionization energy obtained using the CV measurement method was -5.24 eV, and the electron affinity was -2.29 eV, which showed some differences from the values obtained using STS spectrum. The potential reasons for these discrepancies can be attributed to the following factors. 1) Environmental differences: CV is measured in solution, while STS is measured on a solid surface in a vacuum. Solvent effects, ionic interactions in solution, and interactions with the substrate affect the energy level. The substrate used in STS (1-ML NaCl/Au(111)) can affect the electronic structure of the molecule, which causes changes in ionization energy and electron affinity. 2) Measurement method differences: CV obtains energy indirectly through electrochemical reactions with ensemble average method, while STS measures individual electron levels directly.

3. 2. 4. STM scan images of the DABNA-1 molecule

I investigated the resonant tunneling channels in the dI/dV spectrum using STM to analyze the electronic structure of the DABNA-1 molecule. STM imaging, performed at V_s of -2.3 V and +2.6 V, corresponded to the electronic states HOMO and LUMO, respectively. The customized Cl-terminated tip allowed for precise analysis of the molecule's orbitals while maintaining stability within this voltage range. The STM scanning utilized two modes to optimize the resolution of MO imaging. The C.C. mode,

while tending to overestimate the size of the MOs, offers a comprehensive view of the MO configurations. In contrast, the C.H. mode provides an image closer to the actual size of the MOs, allowing for their precise spatial localization (**Figures 3-9a** and **3-9b**). This dual-mode approach, especially when coupled with the Cl-terminated tip, yielded high-resolution images that more accurately reflected the MO distribution when compared to those obtained with a bare Au tip.

The observed STM images were compared with the theoretical MO distribution of DABNA-1 calculated via density functional theory (DFT) using the B3LYP method for the gas phase molecule (**Figure 3-9c**).[21] I also accounted for the influence of the NaCl surface by calculating the slab model of the DABNA-1 molecule on a 3-ML the NaCl using DFT-D3 method (**Figure 3-9d**).[17-18] Notably, despite geometric changes of the PPGs upon adsorption to the NaCl surface, the charge density maps predicted by DFT-D3 remained similar to the gas-phase model. The conservation of MO distribution at NaCl surfaces allows for comparison of gas-phase DFT calculations as a benchmark for analyzing STM scans of DABNA-1 on NaCl/Au(111) substrates.

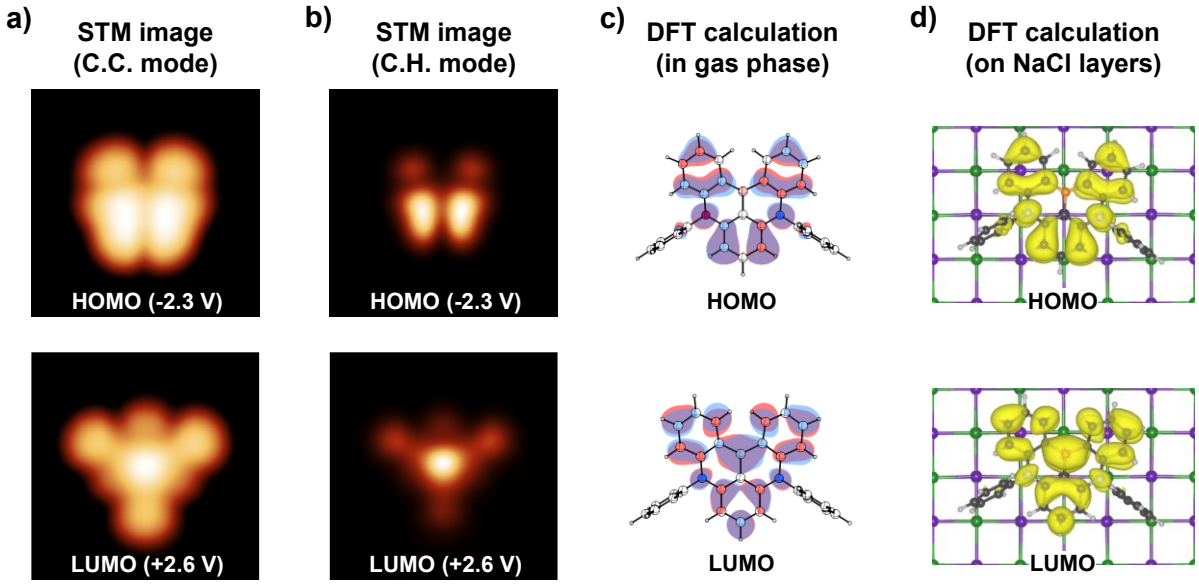

Figure 3-9. Comparison of STM images with Cl-terminated tip and DFT calculation results. STM images with **a)** constant current mode at V_s = -2.3 V / +2.6 V (Cl-terminated tip, scan size = 2.5 nm × 2.5 nm, I_t = +10 pA) and **b)** constant height mode at V_s = -2.3 V / +2.6 V (Cl-terminated tip, scan size = 2.5 nm × 2.5 nm) of DABNA-1 molecule on 1-ML NaCl/Au(111). **c)** DFT calculation result of the DABNA-1 molecule in the gas phase. **d)** Band-decomposed charge density maps of DABNA-1 molecule on 3-ML NaCl near Fermi level (Na, Cl, C, H, N, and B were colored purple, green, dark gray, light gray, light blue, and orange, respectively). The STM images were all denoised using a fast Fourier filter.

Upon examining the STM images scanned at bias voltages -2.3 V and +2.6 V, I can observe features that indicate FMOs in the DABNA-1 molecular structure. At -2.3 V, the electronic state distribution corresponds to the filled states, revealing a quartet of orbital lobes with a notable node centrally located

along the vertical axis. The STM image aligns with the DFT predictions despite exhibiting a different lobe count, displaying a symmetrical structure with the clear node crossing vertically through the center of the molecule's core. With this comparison, which confirmed the match with the MOs calculated by DFT, I verified the state measured at -2.3V as the HOMO. At a positive bias voltage of 2.6 V, the STM image reveals the empty state of DABNA-1, showing a distinct triangle formation with an intense central concentration. This configuration is attributed to the LUMO, primarily formed through the boron atom. The observed STM image is very similar to the LUMO distribution predicted by DFT, with the central high conductivity region representing the LUMO. Nevertheless, the STM results show that there is an additional electron distribution around the upper region of the boron atom position, a feature that was not expected from the DFT calculations. This unexpected electronic state distribution is a MO not predicted in the DFT calculation in the gas-phase, suggesting the presence of interactions and requires more detailed discussion.

3. 2. 5. Discussion of the potential influence of surfaces on STM images

In the detailed investigation of the DABNA-1 molecule on a 1-ML NaCl/Au(111) substrate, the STM imaging and STS analysis revealed an unexpected MO distribution at the location designated as position #4 in **Figure 3-10**. This MO distribution, observed in the LUMO visualization, presented challenges in interpretation due to its deviation from expected results based on computational predictions. Notably, this elusive MO feature extended beyond the π-conjugated PAH framework of the DABNA-1 molecule, leading to challenges in understanding its electronic characteristics. Despite the unexpected position of this MO, the dI/dV spectra at position #4 were consistent with the LUMO characteristics observed at other positions, indicating that this unusual distribution might not represent a different electronic state but rather an unconventional aspect of the LUMO itself. The similarity of features across the dI/dV maps at various positions (#1~#3) corresponding to LUMO energy levels further supports this assumption. To investigate deeper into the structural impact on the molecule's FMOs, I adapted the geometry of the DABNA-1 molecule in its ground state (S_0) to possess C_{2V} symmetry (**Figure 3-11**). These geometric adjustments allowed me to analyze the electronic properties of DABNA-1, which has a molecular structure with relaxed torsion at the surface. However, even with this refined approach, the results did not clarify the ambiguous MO distribution observed in the STM images.

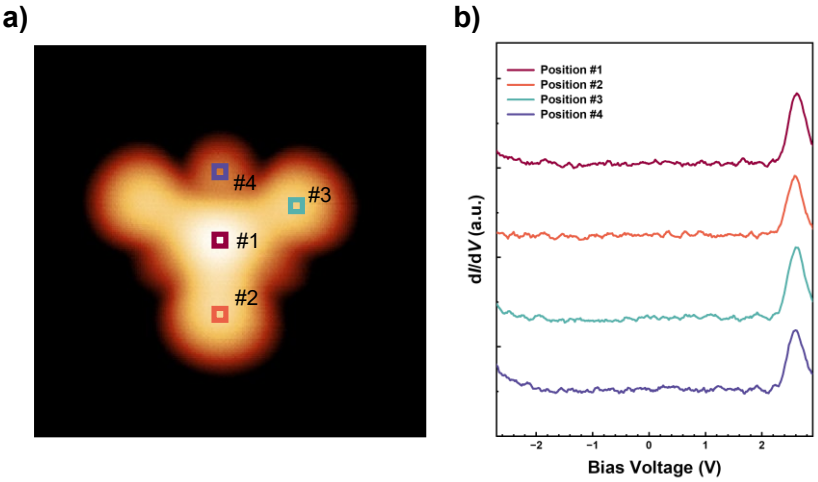

Figure 3-10. a) STM image of DABNA-1 molecule on 1-ML NaCl/Au(111) (I_t = +10.0 pA, V_s = +2.7 V, scan size = 3.0 nm × 3.0 nm). **b)** Moving averaged dI/dV spectrum results depending on tip position #1 ~ #4. Equivalent spectra were measured at all tip positions.

For a comprehensive elucidation, I also considered the charged state of the DABNA-1 molecule. By examining ionization states and their spin density plot, I analyzed to discern any influence these states might have on the observed STM image (**Figure 3-12**). Unfortunately, these investigations did not yield a satisfactory account of the elusive MO distribution. Extending investigation to include the molecule's electronic structures in excited states, I employed a STEOM-DLPNO-CCSD method which was used in ***Chapter II*** (**Figure 3-13**). Nevertheless, the results of these advanced computational methods were also consistent with previous studies and could not explain the distinctive LUMO distribution.

The DFT calculations, considering the interaction between the DABNA-1 molecule and the NaCl surface, reaffirmed that the charge density near the Fermi level on the 3-ML NaCl substrate exhibited characteristics similar characteristics to those predicted for the molecule in the gas phase. Consequently, these findings suggest that the observed features may originate from interactions between the molecules and the metallic substrate underneath the 1-ML NaCl layer. Considering that the geometry of the core structure of the calculated DABNA-1 molecule tends to flatten on the NaCl surface compared to the gas phase, I expect some degree of interface interaction to be working. However, it is complicated to theoretically address the effects of a 1ML NaCl/Au(111) surface due to the incommensurate growth of the NaCl layer on Au(111) in computer analysis. One example of such a solution is to adjust the distance between the molecule and the metallic substrate by varying the thickness of the insulator film. However, in the case of DABNA-1 used in this experiment, high value of bias voltages (-2.3 V for HOMO and +2.6 V for LUMO) are applied for FMO observation, which causes the molecules to be mobile during the scan. **Figure 3-14** shows the molecular stability of DABNA-1 in 2-ML NaCl, which represents the difficulty of this experiment. In this context, due to the difficulty in fully understanding the range of interactions between the molecule and its surroundings and their impact on STM scan images, additional

research and the development of more refined theoretical models or experimental setups are needed to address the discrepancy between computational predictions and empirical observations.

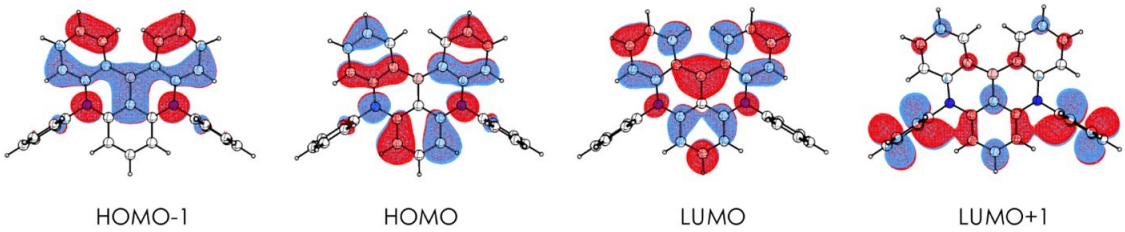

Figure 3-11. The MO distributions for the DABNA-1 molecule are referenced from the geometry with the C_{2V} point group. This geometry was manipulated from the optimized S_0 state using the B3LYP/def2-SVP method. For the visualization of MOs, an iso-value of 0.02 was employed.

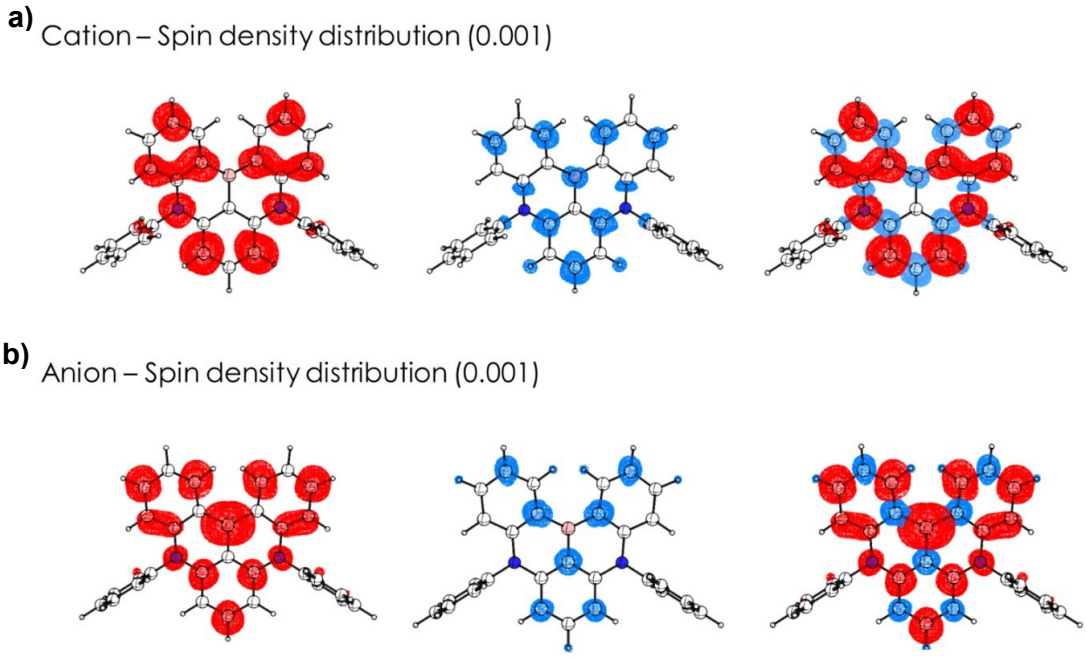

Figure 3-12. Spin density plot for the DABNA-1 molecule referenced from the optimized ground geometry using B3LYP/def2-SVP method; **a)** Cation state and **b)** anion state. Herein, the red (blue) colored mesh corresponds to spin up (spin down) with an iso-surface of 0.001.

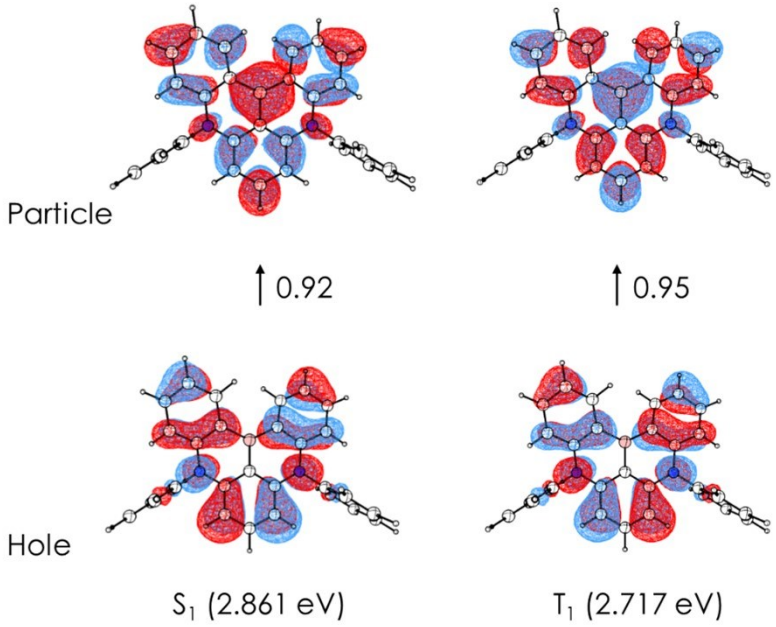

Figure 3-13. NTO behaviors at S_1 and T_1 using a post-HF method (STEOM-DLPNO-CCSD/def2-SVP). Hole and particle wave functions (i.e., virtual MOs) with the weight are placed above the arrows, respectively.

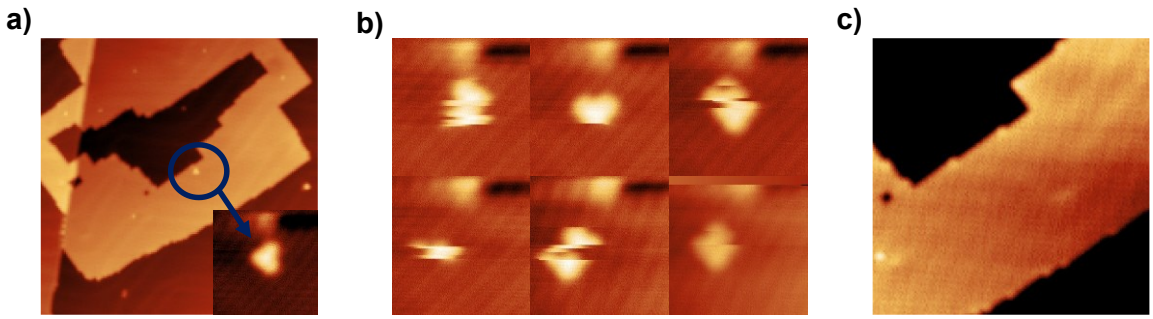

Figure 3-14. a) STM images of DABNA-1 molecule on 2-ML NaCl/Au(111) in constant current mode (I_t = +3 pA, V_s: +1.0 V, scan size: 50 nm × 50 nm; inset: 5 nm × 5 nm). **b)** The observed instability of DABNA-1 molecule on 2-ML NaCl/Au(111) by STM scans. **c)** After several STM scans, the DABNA-1 molecule had disappeared.

3. 2. 6. Visualization of FMOs in DABNA-1 molecule

FMO visualization of the DABNA-1 molecule, supported by dI/dV mapping with voltage modulation, led to a precise analysis of the electronic states corresponding to HOMO and LUMO. This mapping was meticulously conducted in C.H. mode to ensure a more precise observation of the MOs at their actual

size, facilitating a clearer identification of the nodal structure in the center of the HOMO and the boundary delineating the central region at the boron atom for the LUMO, as illustrated in **Figure 3-15**.

This approach allowed us to observe the electronic state distribution in detail, which I further compared with DFT calculations. A notable feature observed through d*I*/d*V* mapping is that the regions where high tunneling current is detected correspond to the positions of the heteroatoms in both the HOMO and LUMO. For the LUMO, a strong current is detected in the region corresponding to the central boron atom. For the HOMO, although it could be the problem of insufficient tip spatial resolution, it is observed that the nitrogen atom and the surrounding MOs form a single large MO lobe. Next, distinct MOs are also observed at the para positions of each heteroatom. In the case of the LUMO, the elusive MO distribution is still observed.

Interestingly, it appears that the MO distribution of the DABNA-1 molecule on the 1-ML NaCl/Au(111) surface, particularly due to the resonance effects, might be overestimated at the para positions and underestimated at the ortho positions relative to the equivalent distribution of typical MOs of the benzene ring. Despite the potential influence of interactions between the molecule and the surface, a standardized analysis and application of these observations can significantly contribute to examining the STM scan results of the DABNA-1 molecule on 1 ML NaCl/Au(111). Therefore, I have established a hypothesis to address these discrepancies.

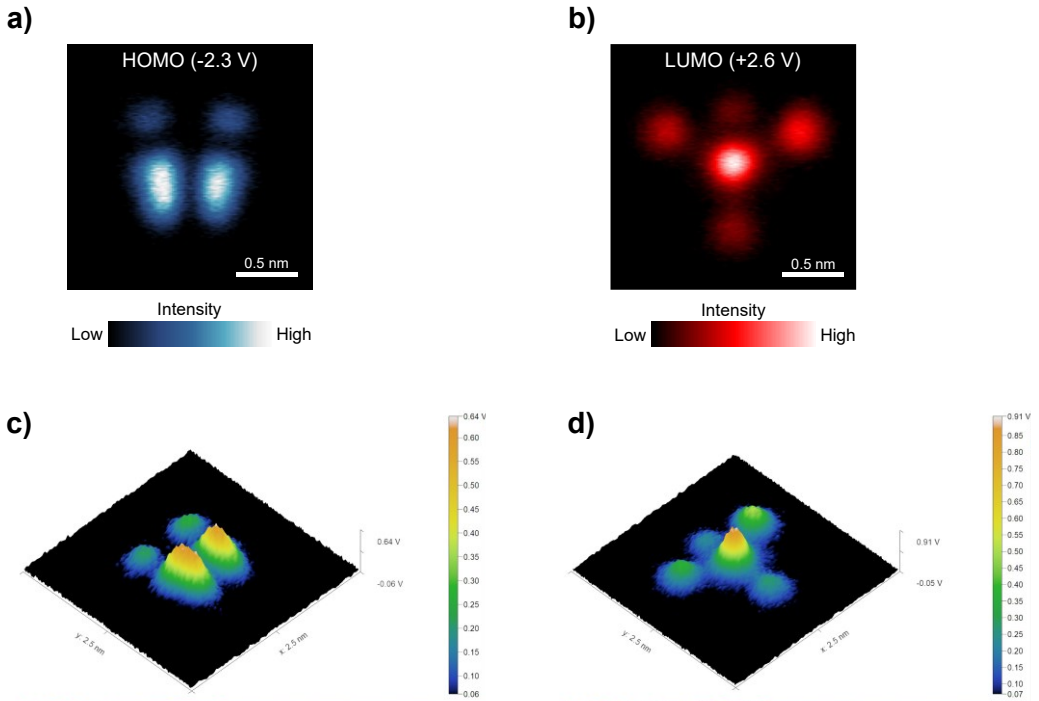

Figure 3-15. Spatial distribution of d*I*/d*V* maps to clearly recognize the MOs separation of DABNA-1 molecule on 1-ML NaCl/Au(111). d*I*/d*V* mapping results at **a)** -2.3 V (HOMO) and **b)** +2.6 V (LUMO) bias voltage with constant height mode and their 3D view data of each **c)** HOMO and **d)** LUMO result.

This observation led to an extension of the conventional resonance effect model to incorporate this unique distinguishing, schematically illustrated in **Figure 3-16**. In the detailed analysis of the HOMO distribution, a significant similarity was observed when considering that the nitrogen atoms and their adjacent MO lobes coalesce into one extensive orbital lobe. This phenomenon is presumed to be due to the electron-donating ability of the nitrogen atom, which contributes to the formation of bonding orbitals within the molecular structure. The LUMO distribution still presented elusive features, but it also closely matched the expected trigonal shape of the LUMO as visualized in the STM images. These findings challenge previous theories that typically predict equivalent orbital sizes for *ortho* and *para* positions in benzene rings influenced by heteroatoms. These insights not only enhance understanding of the electronic properties of DABNA-1 but also highlight the intricacies of predicting MO distributions in resonance effect systems. Although this extension model has only been validated in the limited condition of the DABNA-1 molecule on 1ML NaCl/Au(111), the integration of STM visualization techniques with theoretical models offers a more advanced perspective, potentially leading to more accurate predictions and optimized design of MR-TADF materials for optoelectronic applications. Therefore, these results demonstrate the potential of STM analysis to provide novel insights into the distribution of MOs influenced by resonance effects. This can significantly impact the design of MR-TADF molecules, depending on further experimental verification. For this, further experimental verification is essential, requiring validation across various molecular structures and environments.

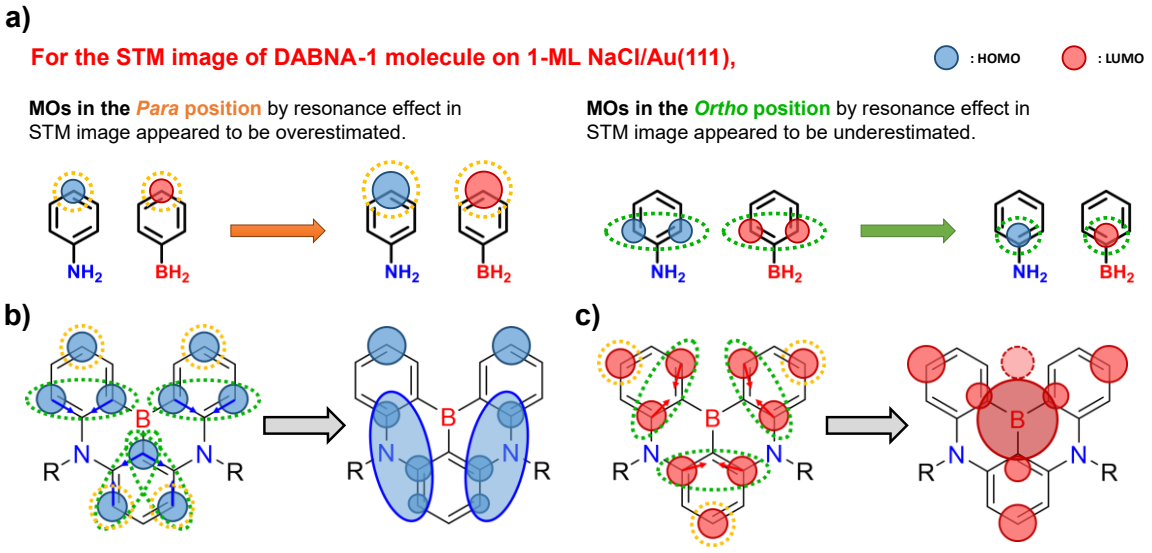

Figure 3-16. a) Schematic illustration of the features seen in the MO distribution observed by STM of the DABNA-1 molecule and its application to the conventional resonance effect model for the **b)** HOMO and **c)** LUMO distributions. The red dashed line circles in **Figure 3-16c** indicate the distribution estimated to be formed by interaction with the surface.

Finally, the visualization results from STM provided crucial observations in confirming the spatial separation between the HOMO and LUMO through detailed analysis using superimposed images. As shown in **Figure 3-17**, the superimposed d*I*/d*V* map integrated with the ball-and-stick model of the DABNA-1 molecule demonstrates a distinct separation of HOMO and LUMO, primarily around each heteroatom in the molecule and their para positions. The distribution of such MOs provides insight into the behavior of electron density within a molecule upon excitation, considering that CT characteristics are crucial in defining the photophysical properties of a molecule. Furthermore, the spatial separation of FMOs analyzed by d*I*/d*V* mapping results supports the insistence that the strong *f* of the DABNA-1 molecule is primarily due to multi-site short-range CT.[22]

These results confirm previous theoretical predictions regarding the electronic structure of the DABNA-1 molecule by providing a tangible visualization of how resonance effects contribute to FMO formation. The findings affirm the role of precise spatial control of MOs in facilitating efficient CT mechanisms, which are essential for the enhanced performance of materials used in optoelectronic applications. This in-depth understanding of HOMO and LUMO distributions, and their separation at specific molecular positions, can guide designs and optimizations of TADF molecules, potentially leading to the development of next-generation OLEDs.

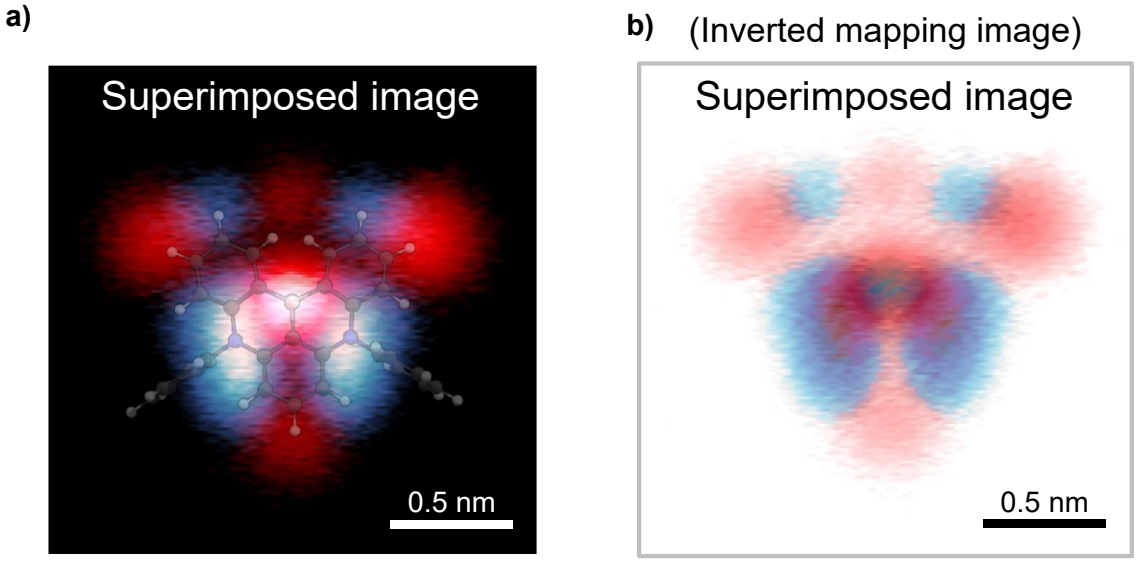

Figure 3-17. a) Superimposed image overlaid the ball-and-stick model of the DABNA-1 molecule structure and **b)** its inverted mapping image. Blue color regions represent the HOMO distribution and red color regions represent LUMO distribution, respectively. Scan size of all images = 2.0 nm × 2.0 nm.

3. 3. Conclusion

The MO theory, which describes MOs as the result of the linear combination of atomic orbitals, is a cornerstone of computational chemistry, foundational for techniques like DFT and post-HF methods. These MO theories are crucial for exploring the electronic properties of molecules, providing a framework for translating theoretical configurations into concrete, observable phenomena. The significance of MOs extends beyond their theoretical implications; they serve as essential elements that enhance understanding of molecular structures and their electronic behaviors. In research on the DABNA-1 molecule, a representative MR-TADF molecule, I adopted this theoretical framework to investigate its spatial distribution and electronic properties at the molecular level as a comparison to experimental results. These experimental insights reveal how heteroatom within the PAH core influences the electronic structure, particularly the HOMO and LUMO. By mapping these orbitals, I have unveiled intricate and delicate resonance effects that go beyond the atomic interactions conventionally modeled in computational chemistry.

This investigation has highlighted the need to improve our understanding of the organic molecular resonance effect, suggesting that the position of heteroatoms within the PAH core is a crucial factor influencing the electronic properties of MR-TADF molecules. By providing direct insights into the HOMO and LUMO distributions affected by resonance effects, it is expected to contribute to the optimized design of MR-TADF molecules. Consequently, it is anticipated to inspire further research on molecular design aimed at optimizing electronic properties for enhanced performance in applications such as OLEDs. In conclusion, the analysis of single molecules using STM not only improved existing knowledge by linking theoretical models and empirical data but also laid the foundation for future research on the complex interactions between molecular structure and electronic properties. Therefore, with this experiment, I have confirmed the strong potential of STM and emphasized the need for further experiments for more precise and accurate analysis.

3. 4. Experimental section

Sample preparation

Molecule Evaporating condition of 5,9-diphenyl-5,9-diaza-13b-bora-5*H*,9*H*-naphtho[3,2,1-*de*]anthracene (DABNA-1) molecule[1] was checked in a home-built mini vacuum chamber. The evaporator containing DABNA-1 molecules was heated in vacuum condition (~ 2.0×10^{-9}) and

measured the change in pressure with respect to the temperature in the chamber. The deposition temperature of the DABNA-1 molecule was determined based on these results (**Figure 3-18a**).

Substrate A single crystal Au(111) surface is prepared as a substrate (**Figure 3-18b**). The Au(111) surface was cleaned by repeated cycles of sputtering process by Ar^+ ion bombardment and heat treatment process by annealing. The NaCl is deposited to grow an insulator film on Au(111) surface at room temperature, using a home-made evaporator heated at 800 K. After deposition, 1 and 2-ML NaCl islands formed on Au(111) were observed in STM scan images (**Figure 3-2b**). DABNA-1 molecule was then deposited onto the Au(111) surface on which NaCl films were grown, using another homemade effusion cell evaporator attached to the STM chamber. The evaporator was heated to 170 °C and DABNA-1 molecules were deposited on prepared substrate kept at 4.6 K ~ 14 K (for low-temperature deposition) in the STM chamber. The deposition proceeded until the appropriate number of DABNA-1 molecules were observed on the 1-ML NaCl film.

STM tip The bare metal (Au) tip was prepared from Au wire etched by an electrochemical method (**Figure 3-19**). The fabricated STM tip was loaded into the STM head after confirming the condition of the tip apex using a scanning electron microscope (SEM). Before STM scanning of the target molecule, the STM tip was adequately conditioned by controlled indentation and voltage pulses on the Au(111) surface. Chlorine (Cl) atoms for tip functionalization were obtained from NaCl films deposited on the Au(111) surface. The Cl-terminated tip was fabricated by STM operation using a bare Au tip (**Figure 3-20**).

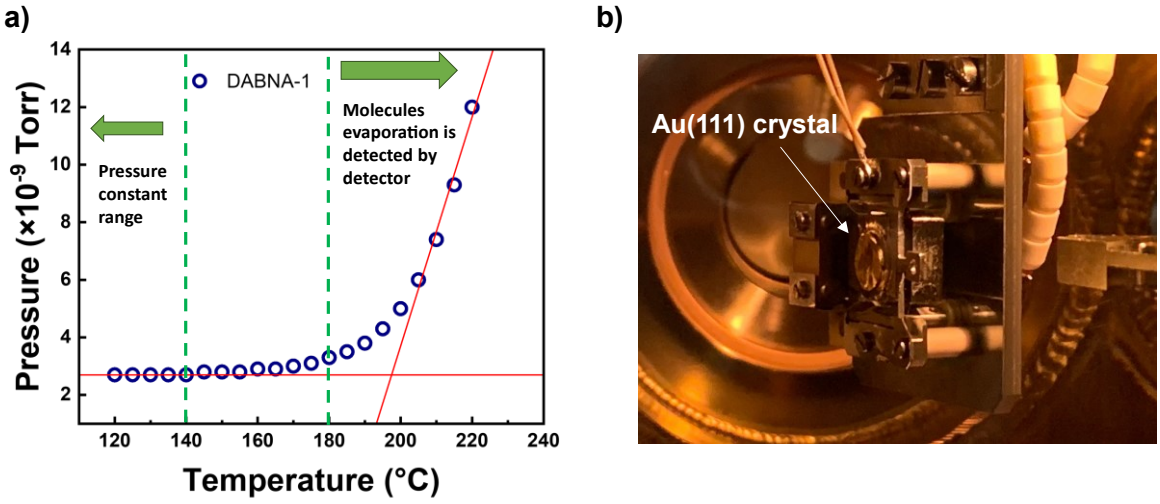

Figure 3-18. **a)** Evaporation test for measuring pressure-temperature graph of the DABNA-1 molecule **b)** substrate with Au(111) crystal.

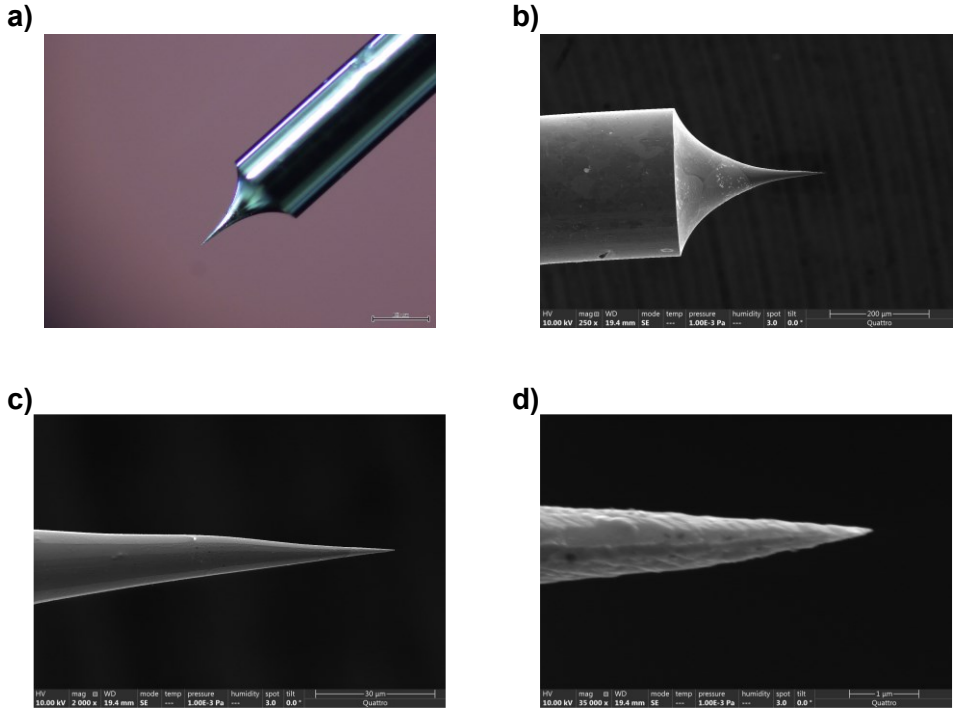

Figure 3-19. Fabricated STM tip by electrochemistry method. **a)** Optical microscope images and SEM images at **b)** 250x, **c)** 2,000x, and **d)** 35,000x magnification.

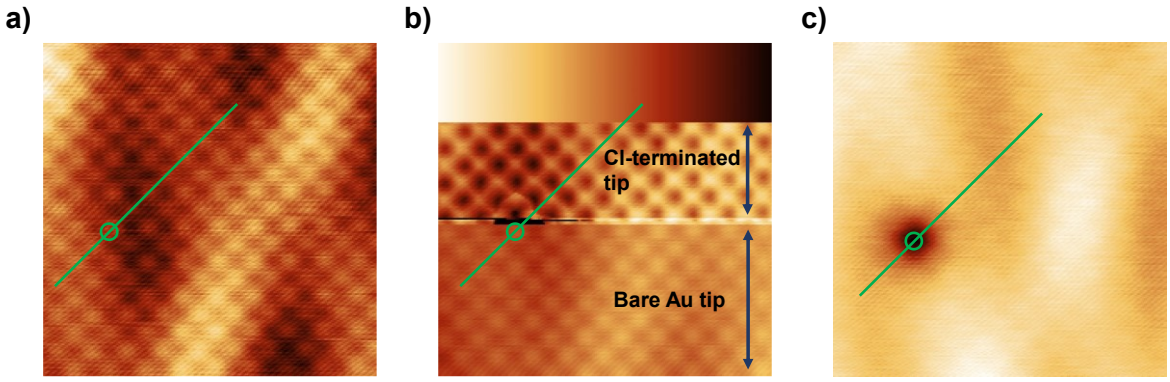

Figure 3-20. Cl-terminated tip fabrication in 1-ML NaCl/Au(111). **a)** Atomically resolved 1-ML NaCl/Au(111) surface using bare metal (Au) tip (I_t = +2.0 nA, V_s = +50 mV, scan size = 5.0 nm × 5.0 nm). **b)** The apex of the tip was positioned over the Cl atom in the green circle, and V_s was changed from +20 mV to +10 mV at I_t +2.0 nA (scan size = 5.0 nm × 5.0 nm). **c)** Vacancy formed where the Cl atom was after the Cl-terminated tip was fabricated (I_t = +10 pA, V_s = +1.0 V, scan size = 5.0 nm × 5.0 nm).

STM results

All STM/STS experiments were conducted using low-temperature STM (Omicron, **Figure 3-21**) operating at a cryogenic condition (4.6 K) under an ultra-high vacuum environment (~ 5.8 × 10^{-11} torr).

In this experiment, two STM modes were used to scan the distribution of electronic states in the molecule: C.C. mode and C.H. mode. In C.C. mode, the STM detects fluctuations in tunneling current through a feedback loop and compensates for them so that the tip is located in the spatial position where the set tunneling current is detected. Alternatively, in C.H. mode, the STM detects changes in tunneling current (I_t) at a predetermined STM tip height. This C.H. mode is limited by the measurement conditions in which the surface must be flat, but it allows for STM images that are closer to the actual size of the molecule, and scanning at higher speeds because the tip does not need to move in height. The height of the tip for the constant height mode STM image of HOMO and LUMO was determined based on the highest position of the STM tip according to the respective electronic state distribution in the constant current mode. The height of the STM tip was then carefully lowered and remeasured until an apparent STM image was obtained. dI/dV spectra and mappings were measured with the bias modulation of 50 mV at 617 Hz with a feedback loop open. All the dI/dV spectra were measured by the bare Au tip. The Cl-terminated tip was confirmed to have maintained its tip functionalization by scanning the atomically resolved 1-ML NaCl/Au(111) surface after STM measurements.

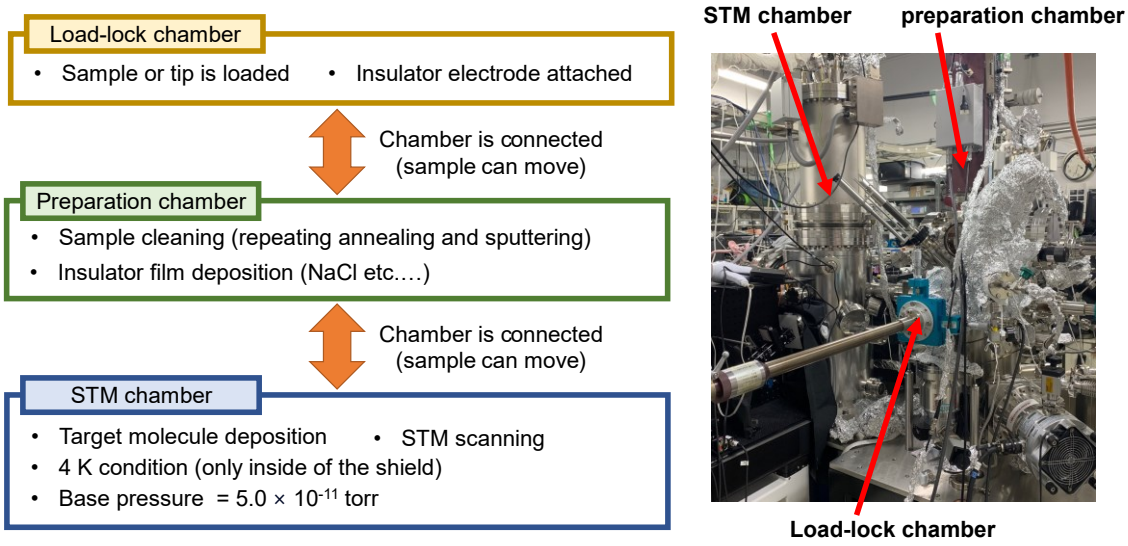

Figure 3-21. Chamber configuration and explanations of STM.

Computational details

Electronic structures of DABNA-1 molecule in gas phases

To examine the electronic properties of the DABNA-1 molecule, we initially optimized its ground (S_0) state using the Becke, 3-parameter, Lee-Yang-Parr (B3LYP) hybrid functional, employing a basis set (def2-SVP) that ensures valence double-ζ polarized quality for all atoms.[21,23] Subsequently, we

computed the vibration frequencies for the optimized geometry to confirm the absence of any negative frequencies. Following this, we investigated the electronic vertical absorption using the same hybrid functionals and basis sets within the linear response of the time-dependent DFT (TD-DFT) framework. We carried out natural transition orbital (NTO) analyses to further understand the nature of excited states in the target molecule.[24] Additionally, we conducted spin density distribution for the DABNA-1 molecule in the doublet state (either cation or anion), referencing the S_0 geometry obtained from the B3LYP/def2-SVP method. Considering the expectation value for the $\hat{S}^2$ operator ($<S^2>$) was 0.7506 for the cation and 0.7502 for the anion, respectively, we conclude that the magnitude of spin contamination in this molecule is significantly less, particularly for the doublet radicals.

According to the previous studies, there has been a consistent observation that the computed ΔE_{ST} between the S_1 and T_1 states of MR-TADF molecule, such as DABNA-1 molecule, was overestimated.[25,26] This finding persisted regardless of the choice of the DFT functionals and the utilization of TD-DFT. Specifically, even when using tuned range-separated functionals designed to correct the Hartree-Fock (HF) ratio for the exchange-correlation energy, which adjusts for the excited energies of conventional D-A type CT clusters, there was no significant compensation for the overestimated value of ΔE_{ST}. In this regard, to accurately model the electrical properties of the DABNA-1 molecule, we employed the STEOM-CCSD calculations.[27,28] Specifically, we utilized the DLPNO theory-based STEOM-CCSD method, which is known for providing accurate excited energy levels for large-size molecules. We applied the same basis set, def2-SVP, as the one used for optimizing the S_0 state at the level of DFT. As a result, we obtained converged vertical energies for the S_1 state at 2.861 eV and the T_1 state at 2.717 eV, referenced from the S_0 geometry obtained at B3LYP/def2-SVP. The percentage of active character in each excited state (i.e., S_1 and T_1 states) was approximately ~ 97 %, indicating that these states converged. We further conducted NTO analyses to gain insights into the nature of excited states. All calculations above in this work were conducted using Gaussian 16W,[29] Jaguar (version 11.7),[30] and ORCA (version 5.0.3).[31]

Simulated slab model of DABNA-1 molecule on 3-ML NaCl

Spin-polarized periodic DFT calculations were performed using the Perdew-Burke-Ernzerhof (PBE) functional[32] as implemented in the Vienna Ab-initio Simulation Package (VASP) code.[17,34] Grimme's D3 method was used to take account of dispersion interactions at the interface between the molecule and NaCl surface.[35] The core electrons were replaced by projector-augmented wave (PAW) pseudopotentials, which were expanded in a basis set of plane waves with a cutoff energy of 400 eV.[35] The slab models consist of DABNA-1 molecule on (6 × 6) supercells of three NaCl layers for ionic relaxations to prevent the rumpling of insulating film in 1-ML which can overestimate the interfacial interaction between the molecule and surface. The periodically replicated slabs were separated by over

15 Å of vacuum, and the dipole correction was applied to avoid interactions between periodic slab images. The convergence criteria for the electronic self-consistent iterations and ionic relaxations were 10^{-7} eV and 0.01 eV/Å, respectively.

The thermodynamically stable adsorption site was calculated considering possible configurations and the optimized structure shows the same result with experimental results. Differing from the gas phase calculation result, the torsion of the DABNA-1 core reduced and became a planar structure with a torsional angle of ~ 5° on the NaCl surface. This is expected due to interfacial interaction between molecule and surface. For further investigation, the electronic structures of the molecule, DOS, and band-decomposed charge density with an iso-surface level of 0.0007 e/Å^3 were analyzed which was discussed below.

Energy level alignment at DABNA-1 molecule on 1-ML NaCl/Au(111)

To investigate the energy positions of the ionization and electron affinity energy levels, the bias voltage (V_s) should be compensated for the voltage drop effect within the NaCl film.[19] The voltage drop induced by V_s and the concomitant change in Fermi energy level (E_F) is depicted in **Figure 3-8**. To estimate the intrinsic energy levels of ionization and electron affinity (E_i and E_a, respectively) at $V_s = 0$ from the peak position (V_η) of the dI/dV spectrum, the following equation can be utilized.[19,20]

$$V_\eta = \frac{d_{\mathrm{NaCl}} E_\eta}{\varepsilon_r} \frac{1}{d_{\mathrm{vac}}} + E_\eta \quad (\eta = a \text{ or } i) \tag{3.1}$$

In this equation, ε_r, d_{NaCl}, and d_{vac} are relative dielectric constant, thickness of NaCl film, and tip-NaCl surface distance, respectively. For each parameter, I used the reported value ($\varepsilon_r = 2.1$, $d_{\mathrm{NaCl}} = 288$ pm for 1-ML NaCl/Au(111)) or the estimated value ($d_{\mathrm{vac}} = 895$ pm) from this experimental system.[36] For the estimation of energy positions, the onset values of the first peak of the negative and positive bias voltage regions were used to the observed peak position of the ionization and affinity level (V_i and V_a), respectively. Each onset point was evaluated based on the direction of the state change relative to the E_F of the substrate (at $V_s = 0$). The estimated E_η^F ($\eta =$ a or i) are denoted as E_η^v with respect to E_v based on the work function (Φ_S) of the substrate ($E_\eta^v \equiv \Phi_S - E_\eta^F$). The Φ_S value of 1-ML NaCl/Au(111) was also used as the reported value, -4.22 eV.

3. 5. References

[1] Stipe, B. C.; Rezaei, M. A.; Ho, W. Single-Molecule Vibrational Spectroscopy and Microscopy. *Science* **1998**, *280*, 5370

[2] Pascual, J. I.; Gomez-Herrero, J.; Rogero, C.; Baro, A. M.; Sanchez-Portal, D.; Artacho, E.; Ordejon, P.; Soler, J. M. Seeing molecular orbitals. *Chem. Phys. Lett.* **2000**, *321*, 78–82.

[3] Repp, J.; Meyer, G.; Stojković, S. M.; Gourdon, A.; Joachim, C. Molecules on Insulating Films: Scanning-Tunneling Microscopy Imaging of Individual Molecular Orbitals. *Phys. Rev. Lett.* **2005**, *94*, 026803.

[4] Swart, I.; Gross, L.; Liljeroth, P. Single-Molecule Chemistry and Physics Explored by Low-Temperature Scanning Probe Microscopy. *Chem. Commun*. **2011**, 47, 9011–9023.

[5] Hoffman J. E. Spectroscopic scanning tunneling microscopy insights into Fe-based superconductors *Rep. Prog. Phys.* **2011**, *74*, 124513.

[6] Hasegawa, Y.; Yamada, Y.; Sasaki, M.; Hosokai, T.; Nakanotani, H.; Adachi, C. Well-Ordered 4CzIPN ((4s,6s)-2,4,5,6-Tetra(9-H-Carbazol-9-Yl)Isophthalonitrile) Layers: Molecular Orientation, Electronic Structure, and Angular Distribution of Photoluminescence. *J. Phys. Chem. Lett.* **2018**, *9*, 863–867.

[7] Zoh, I.; Imai-Imada, M.; Bae, J.; Imada, H.; Tsuchiya, Y.; Adachi, C.; Kim, Y. Visualization of Frontier Molecular Orbital Separation of a Single Thermally Activated Delayed Fluorescence Emitter by STM. *J. Phys. Chem. Lett.* **2021**, *12*, 7512–7518.

[8] Mayder, D. M.; Tonge, C. M.; Nguyen, G. D.; Hojo, R.; Paisley, N. R.; Yu, J.; Tom, G.; Burke, S. A.; Hudson, Z. M. Design of High-Performance Thermally Activated Delayed Fluorescence Emitters Containing s-Triazine and s-Heptazine with Molecular Orbital Visualization by STM. *Chem. Mater.* **2022**, *34*, 2624–2635.

[9] Lauwaet, K.; Schouteden, K.; Janssens, E.; Van Haesendonck, C.; Lievens, P.; Trioni, M. I.; Giordano, L.; Pacchioni, G. Resolving All Atoms of an Alkali Halide via Nanomodulation of the Thin NaCl Film Surface Using the Au(111) Reconstruction. *Phys. Rev. B* **2012**, *85*, 245440.

[10] Li, Z.; Schouteden, K.; Iancu, V.; Janssens, E.; Lievens, P.; Van Haesendonck, C.; Cerdá, J. I. Chemically Modified STM Tips for Atomic-Resolution Imaging of Ultrathin NaCl Films. *Nano. Res.* **2015**, *8*, 2223–2230.

[11] Hatakeyama, T.; Shiren, K.; Nakajima, K.; Nomura, S.; Nakatsuka, S.; Kinoshita, K.; Ni, J.; Ono, Y.; Ikuta, T. Ultrapure Blue Thermally Activated Delayed Fluorescence Molecules: Efficient HOMO-LUMO Separation by the Multiple Resonance Effect. *Adv. Mater.* **2016**, *28*, 2777–2781.

[12] Mamada, M.; Hayakawa, M.; Ochi, J.; Hatakeyama, T. Organoboron-Based Multiple-Resonance Emitters: Synthesis, Structure-Property Correlations, and Prospects. *Chem. Soc. Rev.* **2024**, 53, 1624.

[13] Hall, D.; Suresh, S. M.; dos Santos, P. L.; Duda, E.; Bagnich, S.; Pershin, A.; Rajamalli, P.; Cordes, D. B.; Slawin, A. M. Z.; Beljonne, D.; Köhler, A.; Samuel, I. D. W.; Olivier, Y.; Zysman-Colman, E. Improving Processability and Efficiency of Resonant TADF Emitters: A Design Strategy. *Adv. Opt. Mater.* **2020**, *8*, 1901627.

[14] Han, S. H.; Jeong, J. H.; Yoo, J. W.; Lee, J. Y. Ideal Blue Thermally Activated Delayed Fluorescence Emission Assisted by a Thermally Activated Delayed Fluorescence Assistant Dopant through a Fast Reverse Intersystem Crossing Mediated Cascade Energy Transfer Process. *J. Mater. Chem. C* **2019**, *7*, 3082–3089.

[15] Cheon, H. J.; Woo, S. J.; Baek, S. H.; Lee, J. H.; Kim, Y. H. Dense Local Triplet States and Steric Shielding of a Multi-Resonance TADF Emitter Enable High-Performance Deep-Blue OLEDs. *Adv. Mater.* **2022**, *34*, 2207416.

[16] Kim, H. S.; Jin Cheon, H.; Lee, D.; Lee, W.; Kim, J.; Kim, Y.-H.; Yoo, S. Toward Highly Efficient Deep-Blue OLEDs: Tailoring the Multiresonance-Induced TADF Molecules for Suppressed Excimer Formation and near-Unity Horizontal Dipole Ratio. *Sci. Adv*. **2023**, 9, eadf1388.

[17] Grimme, S.; Antony, J.; Ehrlich, S.; Krieg, H. A Consistent and Accurate Ab Initio Parametrization of Density Functional Dispersion Correction (DFT-D) for the 94 Elements H-Pu. *J. Chem. Phys.* **2010**, *132*, 154104.

[18] Grimme, S. Accurate Description of van Der Waals Complexes by Density Functional Theory Including Empirical Corrections. *J. Comput. Chem.* **2004**, *25*, 1463–1473.

[19] Imai-Imada, M.; Imada, H.; Miwa, K.; Jung, J.; Shimizu, T. K.; Kawai, M.; Kim, Y. Energy-Level Alignment of a Single Molecule on Ultrathin Insulating Film. *Phys. Rev. B.* **2018**, *98*, 201403(R).

[20] Wu, S. W.; Nazin, G. V.; Chen, X.; Qiu, X. H.; Ho, W. Control of Relative Tunneling Rates in Single Molecule Bipolar Electron Transport. *Phys. Rev. Lett.* **2004**, *93*, 236802.

[21] Becke, A. D. A New Mixing of Hartree-Fock and Local Density-Functional Theories. *J. Chem. Phys.* **1993**, *98*, 1372–1377.

[22] Pershin, A.; Hall, D.; Lemaur, V.; Sancho-Garcia, J. C.; Muccioli, L.; Zysman-Colman, E.; Beljonne, D.; Olivier, Y. Highly Emissive Excitons with Reduced Exchange Energy in Thermally Activated Delayed Fluorescent Molecules. *Nat. Commun.* **2019**, *10*, 597.

[23] Lee, C.; Yang, eitao; Parr, R. G. Development of the Colic-Salvetti Correlation-Energy Formula into a Functional of the Electron Density. *Phys. Rev. B* **1988**, *37*, 785

[24] Martin, R. L. Natural Transition Orbitals. *J. Chem. Phys*. **2003**, *118*, 4775–4777

[25] Pershin, A.; Hall, D.; Lemaur, V.; Sancho-Garcia, J. C.; Muccioli, L.; Zysman-Colman, E.; Beljonne, D.; Olivier, Y. Highly Emissive Excitons with Reduced Exchange Energy in Thermally Activated Delayed Fluorescent Molecules. *Nat. Commun.* **2019**, *10*, 597.

[26] Kim, H. S.; Jin Cheon, H.; Lee, D.; Lee, W.; Kim, J.; Kim, Y.-H.; Yoo, S. Toward Highly Efficient Deep-Blue OLEDs: Tailoring the Multireso-nance-Induced TADF Molecules for Suppressed Excimer Formation and near-Unity Horizontal Dipole Ratio. *Sci. Adv.* **2023**, *9*, eadf1388.

[27] Dutta, A. K.; Nooijen, M.; Neese, F.; Izsák, R. Exploring the Accuracy of a Low Scaling Similarity Transformed Equation of Motion Method for Vertical Excitation Energies. *J. Chem. Theory Comput.* **2018**, *14*, 72–91.

[28] Bhattacharyya, K. Can TDDFT Render the Electronic Excited States Ordering of Azine Derivative? A Closer Investigation with DLPNO-STEOM-CCSD. *Chem. Phys. Lett.* **2021**, *779*, 138827.

[29] M. J. Frisch, G. W. Trucks, H. B. Schlegel, G. E. Scuseria, M. A. Robb, J. R. Cheeseman, G. Scalmani, V. Barone, G. A. Petersson, H. Nakatsuji, X. Li, M. Caricato, A. V. Marenich, J. Bloino, B. G. Janesko, R. Gomperts, B. Mennucci, H. P. Hratchian, J. V. Ortiz, A. F. Izmaylov, J. L. Sonnenberg, D. WilliamsYoung, F. Ding, F. Lipparini, F. Egidi, J. Goings, B. Peng, A. Petrone, T. Henderson, D. Ranasinghe, V. G. Zakrzewski, J. Gao, N. Rega, G. Zheng, W. Liang, M. Hada, M. Ehara, K. Toyota, R. Fukuda, J. Hasegawa, M. Ishida, T. Nakajima, Y. Honda, O. Kitao, H. Nakai, T. Vreven, K. Throssell, J. A. Montgomery Jr., J. E. Peralta, F. Ogliaro, M. J. Bearpark, J. J. Heyd, E. N. Brothers, K. N. Kudin, V. N. Staroverov, T. A. Keith, R. Kobayashi, J. Normand, K. Raghavachari, A. P. Rendell, J. C. Burant, S. S. Iyengar, J. Tomasi, M. Cossi, J. M. Millam, M. Klene, C. Adamo, R. Cammi, J. W. Ochterski, R. L. Martin, K. Morokuma, O. Farkas, J. B. Foresman, D. J. Fox, Gaussian 16 Revision C.01. *Gaussian Inc.*, **2016**, *16*.

[30] Schrödinger Release 2022-3: Jaguar, *Schrödinger LLC*, **2022**.

[31] Neese, F. The ORCA program system. *Wiley Interdiscip. Rev. Comput. Mol. Sci*. **2012**, *2*, 73–78.

[32] Perdew, J. P.; Burke, K.; Ernzerhof. M. Generalized Gradient Approximation Made Simple. *Phys. Rev. Lett.*, **1996**, *77*, 3865.

[33] Kresse, G.; Furthmü, J. Efficient Iterative Schemes for Ab Initio Total-Energy Calculations Using a Plane-Wave Basis Set. *Phys. Rev. B* **1996**, *54*, 11169.

[34] Kresse, G.; Hafner, J. Ab. Initio Molecular Dynamics for Liquid Metals. *Phys. Rev. B*, **1993**, *47*, 558(R).

[35] Kresse, G.; Joubert, D. From Ultrasoft Pseudopotentials to the Projector Augmented-Wave Method. *Phys. Rev. B* **1999**, *59*, 1758.

[36] Imai-Imada, M.; Imada, H.; Miwa, K.; Tanaka, Y.; Kimura, K.; Zoh, I.; Jaculbia, R. B.; Yoshino, H.; Muranaka, A.; Uchiyama, M.; Kim, Y. Orbital-Resolved Visualization of Single-Molecule Photocurrent Channels. *Nature* **2022**, *603*, 829–834.

Chapter IV

Summary and Perspective

4. 1. Summary and conclusion

In this thesis, I presented comprehensive research aimed at understanding the electronic structures of MR-TADF materials as a function of their organic molecular structure. Through an encompassing investigation that includes computational analysis, photophysical properties, and applications in OLEDs, as well as experimental visualization at the single molecule level, I have enhanced my understanding of the TADF mechanism.

In Chapter 2, I analyzed the impact of partial planarization at boron and nitrogen sites within MR-TADF molecules using dibenzo[14]azaborine derivatives. These findings revealed that such structural modifications significantly affect the electronic and photophysical properties of these materials, enhancing their TADF activity. The experimental and computational analyses provided insight into the role of molecular structure design in optimizing TADF properties, highlighting the importance of SOC and triplet energy level alignment.

In Chapter 3, I performed the experimental visualization of the electronic structure of a single MR-TADF molecule using STM. This pioneering research allowed for direct observation of the FMOs, providing novel insight into the electronic structures of MR-TADF molecules. The visualization of these molecular structures has not only confirmed previous theoretical predictions but also shed light on the intricate details of HOMO-LUMO separation that are crucial for the TADF mechanism.

In summary, I achieved TADF activity from the simplest BN derivatives, which exhibit an excellent color range for blue and ultraviolet TADF emitters. I explained the spin-up conversion mechanism in the simplest BN derivatives through difference spin density plots and theoretically calculated SOCME values. Using the DABNA-1 molecule, a representative material of MR-TADF, I successfully visualized the distribution of FMO formed by the MR effect in actual space. In the STM images, I discussed the configuration of MO distribution and contemplated future research plans to clarify the extended model of the MR effect.

4. 2. Perspective for future research

Over the past 12 years, there has been significant progress in the field of TADF-based organic optoelectronics. However, a detailed understanding of the spin-flip mechanism, crucial for TADF operation, remains elusive. This challenge is particularly pronounced in MR-TADF molecules, where the mechanisms of short-range CT by resonance effects introduce complexities to the spin dynamics. One of the essential processes in TADF, spin upconversion, which enables delayed fluorescence, takes

microseconds to occur and becomes less efficient at high exciton concentrations. This has been an obstacle to the fabrication of practical device fabrication utilizing TADF molecules. Therefore, unraveling the intricate TADF mechanisms is essential to harness the full potential of TADF systems in fabricating highly efficient devices for organic optoelectronics. *To advance this understanding, the following research should explore the in-depth analysis of luminescence characteristics of TADF molecules at the single-molecule level, employing the STM technique (**Figure 4-1a**).*

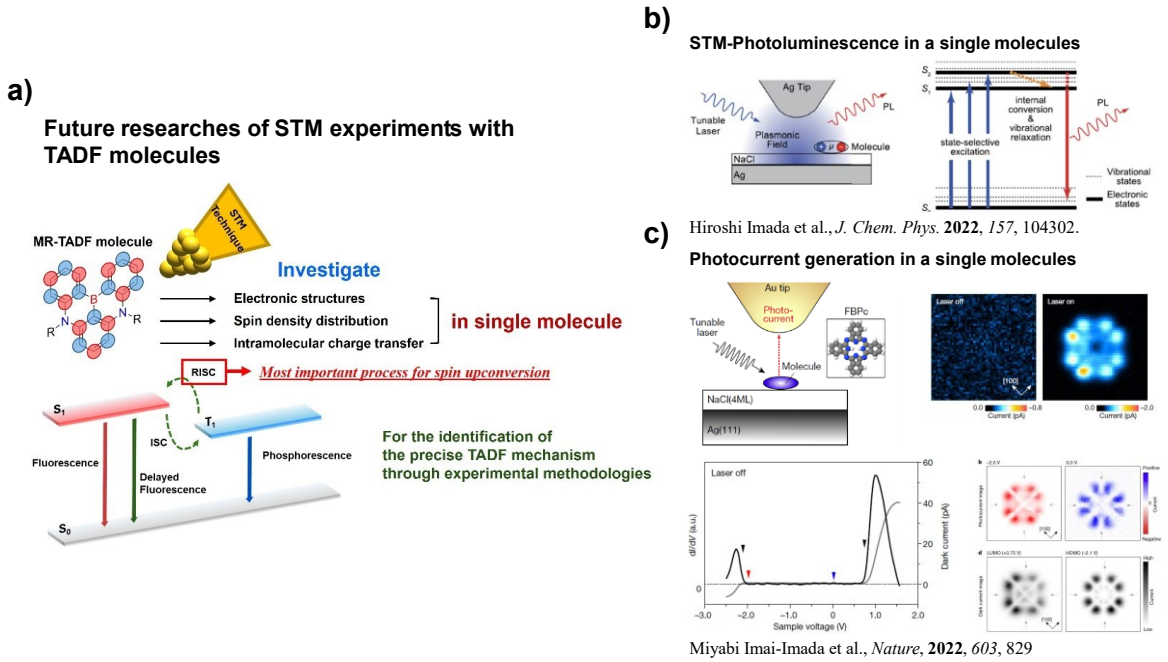

Figure 4-1. Future research for single MR-TADF molecule analysis using STM to elucidate the luminescence mechanism. **Figure 4-1b** edited with permission from Hiroshi Imada and Miyabi Imai-Imada et al., *J. Chem. Phys.* **157**, 104302 (2022*)*, *Rights managed by AIP Publishing*.[4] **Figure 4-1c** edited with permission from Miyabi Imai-Imada et al., *Nature* **603**, 829–834 (2022), *Copyright © 2022 Springer Nature*.[6]

First, photon-STM measurements will introduce a tunneling current as the excitation source, which allows for the selective excitation of individual MR-TADF molecules adsorbed on a solid surface (**Figure 4-1b**). This method not only circumvents the limitations of ensemble averaging but is also expected to accurately determine the energies of S_1 and T_1 excited states on a sub-meV order.[1-5] Analysis of photocurrent channels in MR-TADF molecules also provides important insights into the RISC mechanism, especially aspects of SOC (**Figure 4-1c**).[6] To achieve efficient RISC in TADF molecules, it is necessary to enhance SOC by having different excited states according to El-Sayed's rule. According to El-sayed's rule, the transition between the singlet and triplet excitonic states should involve a radiationless transition that changes the MO type for a large intersystem crossing. Therefore, the understanding of the electron transition of excited states is key to an efficient RISC process.

Nevertheless, due to technical limitations in observing the spin distribution of excited states, previous studies have relied entirely on computational chemistry. Previous, transitions of singlet and triplet states are generally identified through visualization of natural transition orbital (NTO) or difference density plots of excited states from theoretical calculations. Analyzing photocurrent from the excited states of single molecules can complement computational chemistry methods in analyzing electron transitions. Photocurrent analysis offers empirical evidence of how these transitions manifest in real space conditions. This complementary analysis between theoretical predictions and experimental observations can offer a more comprehensive understanding of photophysical processes, validate theoretical models, and provide new insights into the design of more efficient organic optoelectronic materials.

4. 3. References

[1] Imada, H.; Miwa, K.; Imai-Imada, M.; Kawahara, S.; Kimura, K.; Kim, Y. Real-space investigation of energy transfer in heterogeneous molecular dimers. *Nature* **2016**, *538*, 364.

[2] Imada, H; Miwa, K; Imai-Imada, M.; Kawahara, S.; Kimura, K.; Kim, Y. Single-Molecule Investigation of Energy Dynamics in a Coupled Plasmon-Exciton System. *Phys. Rev. Lett.* **2017**, *119*, 013901.

[3] Imada, H.; Imai-Imada, M.; Miwa, K.; Yamane, H.; Iwasa, T.; Tanaka, Y.; Toriumi, N.; Kimura, K.; Yokoshi, N.; Muranaka, A.; Uchiyama, M.; Taketsugu, T.; Kato, Y.; Ishihara, H.; Kim, Y. Single-molecule laser nanospectroscopy with micro–electron volt energy resolution. *Science* **2021**, *373*, 95-98.

[4] Imada, H.; Imai-Imada, M.; Ouyang, X.; Muranaka, A.; Kim Y. Anti-Kasha emissions of single molecules in a plasmonic nanocavity. *J. Chem. Phys.* **2022**, *157*, 104302.

[5] Kimura, K.; Miwa, K.; Imada, H.; Imai-Imada, M.; Kawahara, S.; Takeya, J.; Kawai, M.; Galperin, M.; Nature, Kim, Y. Selective triplet exciton formation in a single molecule. *Nature* **2019**, *570*, 210.

[6] Imai-Imada, M.; Imada, H.; Miwa, K.; Tanaka, Y.; Kimura, K.; Zoh, I.; Jaculbia, R.; Yoshino, H.; Muranaka, A.; Uchiyama, M.; Kim, Y. Orbital-resolved visualization of single-molecule photocurrent channels. *Nature* **2022**, *603*, 829.

The list of Publications

Original papers

1. **Jaehyun Bae**, Miyabi Imai-Imada, Hyung Suk Kim, Minhui Lee, Hiroshi Imada, Youichi Tsuchiya, Takuji Hatakeyama, Chihaya Adachi, Yousoo Kim, 'Visualization of Multiple-Resonance-Induced Frontier Molecular Orbitals in a Single Multiple-Resonance Thermally Activated Delayed Fluorescence Molecule', *ACS Nano* **2024**, *(accepted)*

2. **Jaehyun Bae**, Mika Sakai, Youichi Tsuchiya, Naoki Ando, Xian-Kai Chen, Thanh Ba Nguyen, Chin-Yiu Chan, Yi-Ting Lee, Morgan Auffray, Hajime Nakanotani, Shigehiro Yamaguchi and Chihaya Adachi, 'Multiple resonance type thermally activated delayed fluorescence by dibenzo [1,4] azaborine derivatives', *Front. Chem.* **2022**, *10*, 990918

Joint papers

1. Inhae Zoh, Miyabi Imai-Imada, **Jaehyun Bae**, Hiroshi Imada, Youichi Tsuchiya, Chihaya Adachi, Yousoo Kim, 'Visualization of Frontier Molecular Orbital Separation of a Single Thermally Activated Delayed Fluorescence Emitter by STM', *J. Phys. Chem. Lett.* **2021**, *12*, 7512–7518.

The list of Symposiums

Oral Presentations

1. Visualization of molecular orbital distribution of multiple resonance type thermally activated delayed fluorescence molecules, *Oral*, **Jaehyun Bae**, Miyabi Imai-Imada, Hiroshi Imada, Youichi Tsuchiya, Takuji Hatakeyama, Chihaya Adachi, Yousoo Kim, The Physical Society of Japan 2023 Annual (78th) Meeting, Sendai, Japan, Sep. (2023). (*Domestic*)

2. Multiple resonance type thermally activated delayed fluorescence nature on dibenzo[1,4]azaborine derivatives and their OLED performance, *Oral,* **Jaehyun Bae**, Mika Sakai, Xian-kai Chen, Youichi Tsuchiya, Shigehiro Yamaguchi, and Chihaya Adachi, KJF International Conference on Organic Materials for Electronics and Photonics 2022, Jeju Island, Korea, Sep. (2022). (*International*)

Poster Presentations

1. Atomic-scale investigation for electronic properties of multiple resonance thermally activated delayed fluorescence molecule, *Poster*, **Jaehyun Bae**, Miyabi Imai-Imada, Minhui Lee, Hyungsuk Kim, Hiroshi Imada, Youichi Tsuchiya, Takuji Hatakeyama, Chihaya Adachi, Yousoo Kim, NanospecFY2023, Okazaki, Japan, Mar. (2024). (*International*)

Acknowledgments

First, the author would like to express my deepest respect and gratitude to Prof. Chihaya Adachi of Kyushu University. Throughout my doctoral studies, his constant encouragement and profound discussions have greatly helped me to reflect on the proper attitude and mindset of a researcher.

The author would also like to extend my sincere gratitude to Prof. Yousoo Kim of RIKEN. From admission to graduation, he has always been considerate and attentive, showing great interest in experiments and consistently providing meaningful advice.

The author would also like to extend gratitude to the many students and researchers at OPERA who spent significant time together, sharing assistance, discussions, and enjoyment during my international doctoral program. Special thanks are given to Prof. Hajime Nakanotani, Prof. Youichi Tsuchiya, Dr. Thanh Ba Nguyen, Dr. Chin-Yiu Chan, Dr. Yi-Ting Lee, Dr. Morgan Auffray, and Dr. Hyung Suk Kim for their direct assistance with the paperwork.

The author would also like to thank Dr. Jong Uk Kim, Dr. Gabseok Seo, Dr. Buddhika S. B. Karunathilaka, and Mr. Koudai Ikesue for their considerable support in adjusting to living and researching at Kyushu University.

The author would like to express gratitude to Prof. Shigehiro Yamaguchi, Prof. Mika Sakai, and Dr. Naoki Ando for synthesizing and providing the significant molecules. Their contributions allowed for a deep study of the design and mechanisms of MR-TADF.

The author extends special thanks to all the members of RIKEN and the University of Tokyo who assisted with the STM experiments, which were central to the research. In particular, the author expresses deep gratitude to Dr. Miyabi Imai-Imada, Dr. Hiroshi Imada, and Professor Minhui Lee for their direct assistance, which enabled the acquisition of great data. The author also appreciates the significant assistance received during the research period at RIKEN, not only with the experiments but also in daily life.

The author would also like to express deep gratitude to Prof. Takuji Hatakeyama of Kyoto University for his assistance in designing and synthesizing the MR-TADF molecules for the STM experiments. His keen interest in the research, along with his constant advice and provision of research ideas, has been immensely helpful.

The author would also like to thank to Ms. Sachiko Higashikawa and Ms. Yasura Oiwa for their administrative support, which greatly facilitated a living in Japan.

The author would also like to express deep gratitude to Prof. Suk-Won Choi of Kyung Hee University in Korea for encouraging and providing the opportunity to start the international doctoral program at

Kyushu University. The author greatly appreciates the support provided in taking the first steps as a researcher.

Finally, the author would like to express deep gratitude to their family for their immense support during the study abroad period. Special thanks to the author's parents for their constant encouragement and unwavering support, ensuring a comfortable life while studying in a foreign country.

July 2024

Jaehyun Bae